

UC Irvine

UC Irvine Electronic Theses and Dissertations

Title

Thermodynamic Considerations for CO<sub>2</sub> Activation and Further Reactivity of CO<sub>2</sub> Reduction Products

Permalink

<https://escholarship.org/uc/item/4bq166c8>

Author

Kerr, Tyler Alan

Publication Date

2023

Peer reviewed|Thesis/dissertation

UNIVERSITY OF CALIFORNIA,  
IRVINE

Thermodynamic Considerations for CO<sub>2</sub> Activation and Further Reactivity of CO<sub>2</sub>  
Reduction Products

DISSERTATION

submitted in partial satisfaction of the requirements  
for the degree of

DOCTOR OF PHILOSOPHY

in Chemistry

by

Tyler Alan Kerr

Dissertation Committee:  
Professor Jenny Y. Yang, Chair  
Professor Michael T. Green  
Professor Shane Ardo

2023



## **DEDICATION**

To my family,

To my friends,

To my fur children,

To my love,

# Table of Contents

List of Schemes .....	vi
List of Figures .....	vii
List of Tables .....	x
Acknowledgements .....	xii
Vita .....	xiv
Abstract of the Dissertation .....	xvi
Chapter 0: Background and Motivations .....	1
General Overview .....	1
Research Goals .....	7
References .....	8
Chapter 1: Protonation-Induced Oxidation and Dimerization of a Tungsten Bisdithiolene Complex .....	12
Introduction .....	12
Experimental .....	14
General Methods .....	14
Synthesis of [Na(18-crown-6)] <sub>2</sub> [WS(S <sub>2</sub> C <sub>2</sub> (CH <sub>3</sub> ) <sub>2</sub> ) <sub>2</sub> ] (1b) .....	14
Synthesis of [K(2.2.2-cryptand)] <sub>2</sub> [WS(S <sub>2</sub> C <sub>2</sub> (CH <sub>3</sub> ) <sub>2</sub> ) <sub>2</sub> ] (1c) .....	15
Synthesis of [K(2.2.2-cryptand)] <sub>2</sub> [WS(S <sub>2</sub> C <sub>2</sub> (CH <sub>3</sub> ) <sub>2</sub> ) <sub>2</sub> ] (2) .....	15
X-ray Absorption Measurements .....	15
EXAFS Fitting .....	16
Electrochemical Experiments .....	16

Results and Discussion .....	16
Synthesis and Characterization .....	16
Electrochemical Studies .....	22
Protonation of $W^{IV}$ Salts .....	27
X-ray Absorption Spectroscopy .....	34
EXAFS .....	35
Electrochemical Characterization of Protonation Products .....	37
Hydride Transfer Studies of 1aH .....	39
Infrared Studies on Protonated 1a and Density Functional Analysis .....	41
Six-Coordinate FDH Analogues .....	49
Conclusions and Outlook .....	50
Crystallographic Information .....	52
References .....	56
Chapter 2: Studies of Cobalt Macrocyclic Compounds for $CO_2$ Reduction .....	66
Introduction .....	66
Experimental .....	68
General Methods .....	68
Physical Methods .....	69
Electrochemical Techniques .....	69
Synthesis of $Co(TIM)Br_2PF_6$ .....	70
Synthesis of $Co(SIM)Br_2PF_6$ .....	71
Synthesis of $Co(DIM)Br_2ClO_4$ .....	71
Results and Discussion .....	71
Synthesis and Characterization .....	71

Electrochemical Analysis.....	72
CO <sub>2</sub> Binding.....	73
Electrocatalytic Studies .....	75
Attempted Electrocatalytic CO <sub>2</sub> Reduction Using Co(SIM)Br <sub>2</sub> PF <sub>6</sub> .....	79
Spectroelectrochemical Characterization.....	81
Attempted Isolation of More Soluble Starting Materials .....	86
Conclusions and Outlook .....	89
Crystallographic Information for Co(GIM)(THF)PF <sub>6</sub> .....	90
References .....	92
Chapter 3: Development of an Electrochemical Catalytic System for the Reduction of CO <sub>2</sub> to	
Methanol.....	98
Introduction .....	98
Experimental Methods.....	100
General Considerations .....	100
NMR Experiments.....	100
Results and Discussion .....	101
Esterification and Amidation of HCO <sub>2</sub> <sup>-</sup> .....	101
Conclusions and Outlook .....	115
References .....	116
Appendix A: Tables of Cartesian Coordinates for DFT-Optimized Structures .....	122

## List of Schemes

Scheme 0.1: Thermochemical cycle for the reduction of CO <sub>2</sub> with a metal hydride .....	3
Scheme 0.2: Two systems showing decoupled proton-electron transfer .....	6
Scheme 1.1: Structure of the oxidized and the formate-reduced active site of a typical FDH where M= Mo, W .....	13
Scheme 1.2: Reactivity shown by Seo <i>et al.</i> and reactivity shown here .....	13
Scheme 1.3: Proposed reaction pathway for the conversion of 1c to 2 through protonation .....	33
Scheme 1.4: Attempted hydride transfer studies .....	40
Scheme 1.5: Published work by Fontecave and coworkers and alternate ligand sets for DFT studies .....	47
Scheme 1.6: Potential structure of hydride-reduced 6-coordinate tungsten compound .....	49
Scheme 1.7: Proposed reaction pathway for the decomposition of [Et <sub>4</sub> N]W(S)(SAd)[S <sub>2</sub> C <sub>2</sub> (CH <sub>3</sub> ) <sub>2</sub> ] <sub>2</sub> .....	50
Scheme 2.1: Structures of compounds targeted in this study .....	68
Scheme 2.2: Proposed mechanism for the reversible reduction of CO <sub>2</sub> using a Co(TIM) species as a template .....	68
Scheme 3.1: Proposed electrochemical cascade catalytic process .....	99
Scheme 3.2: Plausible mechanism for the substitution of 4-fluoroaniline into formic acid .....	114



## List of Figures

Figure 0.1: Comparison of energy densities of common energy carriers .....	1
Figure 0.2: Average reduction potentials have a linear relationship with hydricities in metal complexes (Adapted from J. Am. Chem Soc. 2020, 142, 19438) .....	3
Figure 0.3: Energetic contributions from the $pK_a$ and the $E_{1/2}$ on the hydricity of a metal complex .....	4
Figure 0.4: Alternate plot of the contributions of the $pK_a$ and the $E_{1/2}$ of the metal hydride to the hydricity .....	7
Figure 1.1: $^1\text{H}$ -NMRs of 1a (top), 1c (middle), and 1b (bottom) .....	18
Figure 1.2: Solid state crystal structures of (A) 1b and (B) 1c .....	19
Figure 1.3: Room temperature (Top) and $-40^\circ\text{C}$ (Bottom) $^1\text{H}$ -NMR spectra of 1a.....	20
Figure 1.4: Low-temperature ( $-40^\circ\text{C}$ ) $^{13}\text{C}\{^1\text{H}\}$ NMR of 1a in $\text{CD}_3\text{CN}$ .....	20
Figure 1.5: Solid state crystal structure of 2 .....	21
Figure 1.6: Cyclic voltammogram of 1 mM 1a (black) and 1c (red) in $\text{CH}_3\text{CN}$ .....	23
Figure 1.7: Scan-rate dependent cyclic voltammetry studies of 1a .....	23
Figure 1.8: Scan-rate dependent cyclic voltammetry studies of 1c.....	24
Figure 1.9: Scan-rate dependent studies on the reduction of 2 .....	25
Figure 1.10: Scan-rate dependent studies on the oxidation of 2 .....	26
Figure 1.11: Cycled differential pulse voltammetry on the oxidation of 2 .....	26
Figure 1.12: (A) UV-visible titrations of 1a with $\text{Pyrr}\cdot\text{HBF}_4$ in $\text{CH}_3\text{CN}$ and (B) attempted neutralization of acid with DBU .....	28
Figure 1.13: (A) UV-visible titrations of 1c with $\text{Pyrr}\cdot\text{HBF}_4$ in $\text{CH}_3\text{CN}$ . (B) attempted neutralization of acid with DBU .....	28
Figure 1.14: Comparison of UV-visible titrations of acids into solutions of 1a and 1c in $\text{CH}_3\text{CN}$ . 29	

Figure 1.15: Time-resolved spectra of the products of the treatment of 1c with 1 equivalent of Py•HBF <sub>4</sub> in CH <sub>3</sub> CN at room temperature.....	30
Figure 1.16: Time-resolved spectra of the products of the treatment of 1c with 1 equivalent of Py•HBF <sub>4</sub> in CH <sub>3</sub> CN at 50°C .....	31
Figure 1.17: Plot of ln(1cH) vs. time showing a linear relationship .....	32
Figure 1.18: <sup>1</sup> H NMR of the protonation of 1a showing evidence for H <sub>2</sub> and 2 after protonation by Py•HBF <sub>4</sub> .....	34
Figure 1.19: Comparison of W L <sub>3</sub> edge energies. The solid line represents 1a, while the dotted line represents protonated 1aH .....	35
Figure 1.20: EXAFS data and Fourier transforms for 1a (top) and 1aH (bottom) .....	36
Figure 1.21: Cyclic voltammetry studies of the protonation products of 5 mM 1a .....	38
Figure 1.22: Cyclic voltammograms of tungsten compounds.....	38
Figure 1.23: <sup>31</sup> P NMR study of hydride transfer from 1aH to [Ni(dppe) <sub>2</sub> ][BF <sub>4</sub> ] <sub>2</sub> .....	39
Figure 1.24: Infrared spectrum of 1a treated with 1 equivalent of Py•HBF <sub>4</sub> (black) and DFT-simulated spectrum (red) .....	43
Figure 1.25: Infrared Spectrum of 1a treated with 1 equivalent of Py•DOTf (black) and the DFT-simulated spectrum (blue).....	43
Figure 1.26: DFT optimized structure of protonation state C from two angles with selected bond lengths.....	44
Figure 1.27: Plot of relative energies of the various protonation states of WS(S <sub>2</sub> C <sub>2</sub> (CH <sub>3</sub> ) <sub>2</sub> ) <sub>2</sub> H using various basis sets and an alternate method.....	46
Figure 1.28: Relative DFT-calculated energies of various compounds similar to 1a.....	48
Figure 1.29: <sup>1</sup> H-NMR spectra of the reaction of [Et <sub>4</sub> N]W(S)(SAd)[S <sub>2</sub> C <sub>2</sub> (CH <sub>3</sub> ) <sub>2</sub> ] <sub>2</sub> with hydride donors in CD <sub>3</sub> CN.....	50
Figure 2.1: Cyclic voltammograms of saturated solutions of Co(TIM)Br <sub>2</sub> PF <sub>6</sub> (Blue), Co(SIM)Br <sub>2</sub> PF <sub>6</sub> (Black), and Co(DIM)Br <sub>2</sub> ClO <sub>4</sub> (Red) in 100 mM [ <sup>n</sup> Bu <sub>4</sub> N][PF <sub>6</sub> ] in THF.....	73

Figure 2.2: Cyclic voltammograms of Co(TIM)Br <sub>2</sub> PF <sub>6</sub> (A), Co(SIM)Br <sub>2</sub> PF <sub>6</sub> (B), and Co(DIM)Br <sub>2</sub> ClO <sub>4</sub> (C) in THF (black traces) and under CO <sub>2</sub> (blue traces) .....	74
Figure 2.3: Cyclic voltammograms of a saturated solution of Co(SIM)Br <sub>2</sub> PF <sub>6</sub> with acids.....	75
Figure 2.4: Cyclic voltammograms of Co(SIM)Br <sub>2</sub> PF <sub>6</sub> with CO <sub>2</sub> and weak acids.....	76
Figure 2.5: Cyclic voltammograms of Co(TIM)Br <sub>2</sub> PF <sub>6</sub> with CO <sub>2</sub> and acids.....	78
Figure 2.6: Cyclic voltammograms of Co(DIM)Br <sub>2</sub> ClO <sub>4</sub> with CO <sub>2</sub> and acids .....	78
Figure 2.7: Chronoamperograms of the bulk electrolytic reduction of Co(SIM)Br <sub>2</sub> PF <sub>6</sub> in THF ..	79
Figure 2.8: Chronoamperograms of the bulk electrolytic reduction of Co(SIM)Br <sub>2</sub> PF <sub>6</sub> in CH <sub>3</sub> CN .....	80
Figure 2.9: Pre- (black) and post-electrolysis (red) UV-Visible spectra of Electrolysis 2 .....	81
Figure 2.10: Spectroelectrochemistry of Co(SIM)Br <sub>2</sub> PF <sub>6</sub> in THF.....	83
Figure 2.11: Cyclic voltammograms of Co(SIM)Br <sub>2</sub> PF <sub>6</sub> THF with increasing concentration of CH <sub>3</sub> CN.....	83
Figure 2.12: Spectroelectrochemistry of Co(SIM)Br <sub>2</sub> PF <sub>6</sub> in CH <sub>3</sub> CN under an atmosphere of N <sub>2</sub>	85
Figure 2.13: Spectroelectrochemistry of Co(SIM)Br <sub>2</sub> PF <sub>6</sub> in CH <sub>3</sub> CN under an atmosphere of CO <sub>2</sub> .....	86
Figure 2.14: (Top) Solid state crystal structure of Co <sup>II</sup> (GIM)(THF)PF <sub>6</sub> and (bottom) drawn structures of Co(SIM)Br <sub>2</sub> PF <sub>6</sub> and Co(GIM)PF <sub>6</sub> .....	87
Figure 2.15: EPR spectra of Co(SIM)Br <sub>2</sub> PF <sub>6</sub> treated with 1 equiv. of KC <sub>8</sub> in 2-Me-THF (black) and held under vacuum for 3 hours (red).....	88
Figure 3.1: <sup>1</sup> H-NMR spectra of the formyl proton of tetra-n-butylammonium formate in CD <sub>3</sub> CN (Top), with 5 mol% Sc(OTf) <sub>3</sub> (middle), and 10 mol% Al(OTf) <sub>3</sub> (bottom).....	103
Figure 3.2: Two rotamers of a generic formamide .....	109
Figure 3.3: Conversions of 4-fluoroaniline to 4-fluoroanilide in the presence of a salt at 25°C (blue) and 60°C (red).....	113

## List of Tables

Table 0.1: Turnover frequencies for reported studies on catalysis with FDH.....	5
Table 1.1: $pK_a$ s of relevant bases used in this chapter .....	16
Table 1.2: Bond metrics of crystallized tungsten bisdithiolene species.....	22
Table 1.3: Reduction potentials of tungsten compounds .....	23
Table 1.4: EXAFS best fit bond metrics for W-S bonds in 1a and 1aH. ....	36
Table 1.5: EXAFS best fit bond metrics for protonated 1a modeled as 2 .....	37
Table 1.6: Results of hydride transfer studies.....	40
Table 1.7: Tabulated selected metrics for the DFT geometry-optimized structures of protonated $W(S)[S_2C_2(CH_3)_2]_2^{2-}$ .....	42
Table 1.8: Selected bond lengths found using single crystal XRD (for 1b and 1c), EXAFS (for 1a and 1aH), and computational methods for deprotonated and protonated $W(S)[S_2C_2(CH_3)_2]_2^{2-}$ .....	45
Table 1.9: NMR studies of 6-coordinate $W^{VI}$ compounds .....	50
Table 1.10: Crystallographic data for 1b, 1c, and 2.....	55
Table 2.1: Structures of conjugate bases used in this chapter .....	69
Table 2.2: Measured reduction potentials and $CO_2$ binding constants of Co complexes.....	73
Table 2.3: Performance of electrolysis attempts .....	81
Table 2.4: Tabulated reduction potentials of $Co(SIM)Br_2PF_6$ in mixed THF and $CH_3CN$ .....	84
Table 2.5: Crystal data for $Co(GIM)(THF)PF_6$ .....	91
Table 3.1: Relevant solvent-dependent empirically determined constants.....	99
Table 3.2: Relevant $pK_a$ values .....	101
Table 3.3: Diphosphine ligand abbreviations.....	101
Table 3.4: Esterification of $[^nBu_4N][HCO_2]$ with EtOH using Lewis and Brønsted acid catalysts .....	102
Table 3.5: Effect of heating reaction mixtures for 2 weeks.....	103

Table 3.6: Attempted amidations of [ <sup>n</sup> Bu <sub>4</sub> N][HCO <sub>2</sub> ] with dipropylamine and propylamine using Lewis acid catalysts.....	104
Table 3.7: Attempted amidations of [ <sup>n</sup> Bu <sub>4</sub> N][HCO <sub>2</sub> ] with ammonium salts.....	105
Table 3.8: Amidations of formic acid with dipropylamine using Sc(OTf) <sub>3</sub> .....	106
Table 3.9: Amidations and esterification of formic acid in the presence of drying agents .....	107
Table 3.10: Solvent screen and ratio dependence for the amidation of formic acid with 4-fluoroaniline.....	108
Table 3.11: Attempted amidations of [ <sup>n</sup> Bu <sub>4</sub> N][HCO <sub>2</sub> ] with 4-fluoroanilinium triflate by varying ratios and adding Brønsted acids .....	110
Table 3.12: Solvent screen for the attempted amidation of [ <sup>n</sup> Bu <sub>4</sub> N][HCO <sub>2</sub> ] with 4-fluoroanilinium triflate.....	110
Table 3.13: Effect of salts on the amidation of formic acid and 4-fluoroaniline .....	111
Table 3.14: Effect of heating amidation reactions with salts .....	112

## Acknowledgements

First, I'd like to thank the DOE DE-SC0020275 and the UCI Department of Chemistry for funding.

The text and figures of Chapter 0 are an adaptation of the materials in Yang, Jenny Y.; Kerr, Tyler A.; Wang, Xinran S.; Barlow, Jeffrey M. *J. Am. Chem. Soc.*, **2020**, *142*(46), 19438. Permission granted by the American Chemical Society.

To Jenny, thank you so much for all of your support over the last 5 and a half years. It hasn't been easy, but I'm so happy I ended up in your lab.

To past and current Yang Group members, I won't name all of you, but I'll give a special shoutout to Caitlin, Drew, Zach, Steven, Brian, Bianca, Alex, Annie, and Sarah, who all were there from the beginning. Thank you all so much for editing all my documents and pulling (sometimes dragging) me through. And to Allie, Nadia, and Kelsey, who have been key in getting me through writing.

To my candidacy committee, Profs. Evans, Heyduk, Green, Ardo, and Ross, thank you so much for challenging me to do better when I clearly hadn't done enough. I have learned a lot about myself since then, and I am a better scientist because of it.

To Dr. Joe Ziller, with all of 5 hours of experience with X-ray crystallography, you took me as the X-ray fellow. I learned so much under your guidance, and I'm so thankful for all of the on the job training in an extremely useful skill.

To all of the friends that I've met here in SoCal, especially Meghen, Justin, Carly, Taylor, Kirsten, Chuck, Leah, you all have supported me so much, and I'm so happy to have met and gotten to know all of you.

To my family, this hasn't been easy. Living so far away for so long has been hard. Thank you all so much for being there for me.

To Angelika, you are the best partner I could ask for. I'm not always easy to live with. You have been and continue to be my rock. Coming home to you every day for the last 4 years has made my life better. Thank you for being you, and thank you for holding my hand as I've gone through this. And to our animals, Ethylene, Norby, and Jimmy who (begrudgingly) give the best cuddles.

# Vita

## Tyler Alan Kerr

Education	University of California, Irvine Ph.D. in Chemistry, 2023	Irvine, CA
	University of Kansas Bachelor of Science, Chemistry; Minor, Religious Studies, May 2016. KU GPA: 3.0, Cumulative GPA: 3.2 (August 2012 – May 2016)	Lawrence, KS
	Wichita State University Student, Chemistry. GPA: 3.5 (August 2010 – May 2012)	Wichita, KS
Research Experience	University of California, Irvine Advisor: Jenny Yang	Irvine, CA
	University of Kansas Advisor: James Blakemore (May 2016 – July 2017)	Lawrence, KS
	Advisor: Minae Mure (August 2013 – May 2015)	
Publications	<u>Kerr, T.A.</u> ; Yang, J.Y. Proton-Induced Oxidation and Dimerization of a Tungsten Bisdithiolene Complex. <i>In preparation</i> .	
	Cordova, D.L.M.; Chua, K.; <u>Kerr, T.A.</u> ; Aoki, T.; Knez, D.; Skorupskii, G.; Lopez, D.; Ziller, J.W.; Fishman, D.A.; Arguilla, M.Q. 1D van der Waals Tetrahelices with an Irrational Boerdijk-Coxeter Twist. <i>Submitted</i> .	
	Cypcar, A.D.; <u>Kerr, T.A.</u> ; Yang, J.Y. Thermochemical Studies of Nickel Hydride Complexes with Cationic Ligands in Aqueous and Organic Solvents. <i>Organometallics</i> , <b>2022</b> , <i>41</i> (18), 2605.	
	Henke, W.C.; <u>Kerr, T.A.</u> ; Sheridan, T.R.; Henling, L.R.; Takase, M.K.; Day, V.W.; Gray, H.B.; Blakemore, J.D. Synthesis, structural studies, and redox chemistry of bimetallic [Mn(CO) <sub>3</sub> ] and [Re(CO) <sub>3</sub> ] Complexes. <i>Dalton Transactions</i> , <b>2021</b> , <i>50</i> , 2746.	
	Yang, J.Y.; <u>Kerr, T.A.</u> ; Wang, X.S.; Barlow, J.M. Reducing CO <sub>2</sub> to HCO <sub>2</sub> <sup>-</sup> at Mild Potentials: Lessons from Formate Dehydrogenase. <i>J. Am. Chem. Soc.</i> , <b>2020</b> , <i>142</i> (46), 19438.	
	Shaughnessy, C.I.; Sconyers, D.J.; <u>Kerr, T.A.</u> ; Lee H.J.; Subramaniam, B.; Leonard, K.C.; Blakemore, J.D. Intensified Electrocatalytic CO <sub>2</sub> Conversion in Pressure-Tunable CO <sub>2</sub> -Expanded Electrolytes. <i>ChemSusChem</i> , <b>2019</b> , <i>12</i> , 3761-3768.	
Oral Presentations	Tyler A. Kerr and Jenny Y. Yang. "Reactivity Studies of an Active-Site Model Complex of Tungsten-Containing Formate Dehydrogenases." University of California Chemical Symposium, Lake Arrowhead, CA, March 22-24, 2020. **cancelled due to COVID-19 pandemic	
	"Determining the Site of Protonation and the Hydricity of Active-Site Model Complexes of the Tungsten- and Molybdenum-Containing Formate Dehydrogenases." <u>Tyler A. Kerr</u> , and Jenny Y. Yang. ACS National Meeting & Exposition, San Diego, CA, August 25-29, 2019.	
	"Development of New Media for Electrochemical CO <sub>2</sub> Conversion." <u>Tyler A. Kerr</u> , Charles Shaughnessy, Hyun Jin Lee, David J. Sconyers, Bala Subramaniam, Kevin C. Leonard, and James D. Blakemore. 52 <sup>nd</sup> Midwest Regional Meeting of the American Chemical Society in Lawrence, KS. October 18-20, 2017.	



Teaching University of California, Irvine Irvine, CA  
 Inorganic Chemistry Lab (Chem 107L), Teaching Assistant (Winter 2018, Spring 2019)  
 Advanced Inorganic Chemistry (Chem 127) Teaching Assistant (Winter 2021)  
 Inorganic Chemistry Lab (Chem 107L), Head TA (Winter 2020)  
 Organic Chemistry Lab (Chem 51LB / Chem 51LC), Teaching Assistant  
 (Spring 2018, Winter 2018)  
 General Chemistry Lab (Chem 1LD), Teaching Assistant (Fall 2017, Summer 2018)

University of Kansas Lawrence, KS  
 General Chemistry Lab (Chem 135), Teaching Assistant (Springs 2015 and 2016)  
 College Chemistry Lab (Chem 125), Teaching Assistant (Spring 2014)

Poster Tyler A. Kerr and Jenny Y. Yang "Toward Electrocatalytic CO<sub>2</sub> reduction using Cascade Presentations Catalysis." ACS National Meeting & Exposition in San Diego, CA. March 2022.

Tyler A. Kerr and Jenny Y. Yang. "Reactivity Studies of an Active-Site Model Complex of Tungsten-Containing Formate Dehydrogenases." University of California Chemical Symposium, Lake Arrowhead, CA, March 22-24, 2020. \*\*cancelled due to COVID-19 pandemic

Tyler A. Kerr and Jenny Y. Yang. "Reactivity Studies of an Active-Site Model Complex of Tungsten-Containing Formate Dehydrogenases." SoCal Organometallics Conference, Santa Barbara, CA, March 15, 2020. \*\*cancelled due to COVID-19 pandemic

"Tuning the Hydricity of Metal Complexes for Selective CO<sub>2</sub> Reduction" T. Kerr, X. Wang, J. Yang. SoCal Bioinorganic Meeting. December 2, 2018.

"Electrochemical Carbon Dioxide Conversion in CO<sub>2</sub>-Expanded Liquids (CXLs)." T. Kerr, C. Shaughnessy, H. Lee, B. Subramaniam, K. Leonard, and J. Blakemore. Spring CEBC Industry Advisory Board Meeting in Lawrence, KS. April 24, 2017.

"Electrochemical Carbon Dioxide Conversion in CO<sub>2</sub>-Expanded Liquids (CXLs)." T. Kerr, C. Shaughnessy, H. Lee, B. Subramaniam, K. Leonard, and J. Blakemore. Fall CEBC Industry Advisory Board Meeting in Lawrence, KS. Oct. 17, 2016.

"We Are KU Chem Club: The ACS Student Affiliate Chapter at the University of Kansas." T. Kerr, C. Barrett, R. Latimer, E. Lorenzo, M. Holtz, R. Walsh, R. Black, and P. Hanson. ACS National Meeting & Exposition in San Diego, CA. March 2016.

Professional Co-chair for Programming, Registration, and Abstracts. University of California Chemical Activities Symposium. Virtual Meeting. March 2021.

Chairperson, University of California Chemical Symposium 2022, 2023.

Crystallography Fellow, University of California, Irvine. September 2021-September 2022.

# **Abstract of the Dissertation**

Thermodynamic Considerations for CO<sub>2</sub> Activation and Further Reactivity of CO<sub>2</sub>  
Reduction Products

by

Tyler Alan Kerr

Doctor of Philosophy in Chemistry

University of California, Irvine, 2023

Professor Jenny Y. Yang, Chair

Growing global energy demands and greenhouse gas emissions require the development of innovative technologies to both sustain the energy needs of the future and eliminate anthropogenic sources of climate change. By designing and deploying systems that capture, concentrate, and convert CO<sub>2</sub> to useful feedstocks on large scales using renewable, carbonless energy sources, we may be able to achieve a net neutral carbon economy.

One of the biggest challenges with reduction of carbon dioxide is that under standard state, where the concentration of every reagent is 1 M, the pressure of every gas is 1 atmosphere, and the temperature is 25°C, reduction of protons (H<sup>+</sup>) to hydrogen gas (H<sub>2</sub>) is more favorable regardless of the reduction potential. When we move to non-standard state conditions, we can shift the thermodynamics to favor formate (HCO<sub>2</sub><sup>-</sup>) production with metal hydrides. Using empirical solvent-dependent thermodynamic constants that describe the reactivity of these small molecules

in various solvents, we can identify conditions where many reactions with small molecules are favorable.

This dissertation focuses on using these empirically determined thermodynamic values to design systems that can convert CO<sub>2</sub> to reduced products, disfavoring other reactivity. I show, however, that deleterious side-reactivity and unexpected interactions in nonpolar solutions prevent the full understanding of the thermodynamics in the systems presented.

# Chapter 0: Background and Motivations

Portions of this introduction adapted from *J. Am. Chem Soc.* 2020, **142**, 19438.<sup>1</sup>

## General Overview

The United Nations has indicated that the world population has grown from 7 billion in 2011 to 8 billion this month (November 2022).<sup>2</sup> With the population growing, energy demands are growing as well. As we migrate away from fossil fuels as our primary energy source, the use of photovoltaics and wind energy has grown immensely. These intermittent energy sources pose a problem in today's on-demand energy infrastructure: the times of day that energy use is spiking, the sun sets and the wind slows down, decreasing clean energy generation, necessitating the use of smaller, dirtier, on-demand fossil fuel sources.<sup>3</sup> If the conversion to a more sustainable future continues, we need to find inexpensive, quickly deployable, and compact energy storage options. Current state of the art battery technology lags far behind the energy-carrying capacity of liquid and gaseous fuels (Figure 0.1).<sup>4</sup> One way of doing this is storing electrical energy in the form of chemical bonds. Specifically, conversion of carbon dioxide to liquid fuels may be an option for the storage of future intermittent electricity generation.

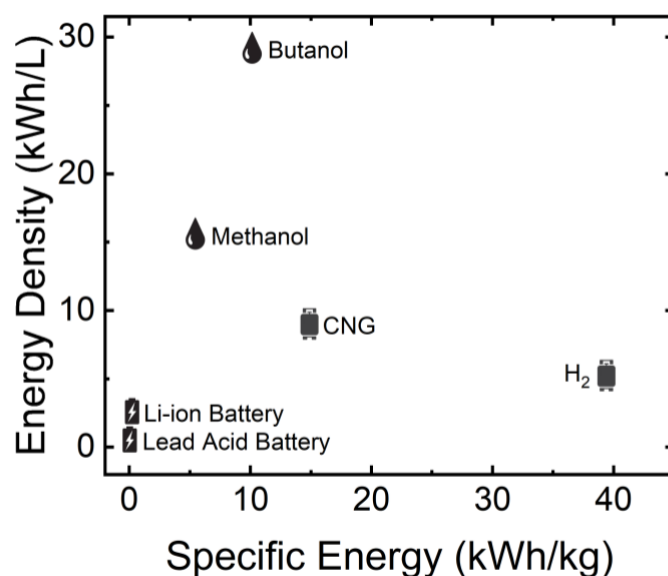


**Figure 0.1:** Comparison of energy densities of common energy carriers

Metal hydrides are of great interest for thermodynamic studies because the overall reactions involve simple elementary reactions that sum to give the overall reaction thermodynamics. While true for all reactions, summation of the thermodynamic contributions from each of the elementary steps of hydride transfers has proven to be useful in predicting reactivity in many systems containing metal hydrides.<sup>5</sup> Work in the Yang Group and much of the work herein has focused on the selective reduction of CO<sub>2</sub>, predicting reactivity using Hess's Law and Bordwell thermodynamic cycles.<sup>6</sup> Having well-defined empirical constants has been crucial in predicting reactivity in many of the systems published by our group.<sup>7-14</sup> Also, the development of well-defined thermochemical cycles with no readily accessible off-cycle intermediates is crucial for the accurate and complete descriptions of the reactivity. A Bordwell-like thermodynamic cycle is shown in Scheme **0.1**. In the first set of reactions, the free energy associated with the release of a solvated hydride by a metal complex, known as the solvent-dependent hydricity (5), is calculated by summing the energetic contributions from each one-electron reduction (2, 3), the equilibrium constant of the protonation of the reduced metal center (4), and a solvent-dependent constant where the two-electron reduction of a proton to a hydride (1) has been determined empirically.<sup>15</sup> Using the metal hydricity, the empirically determined hydricity for formate (6) (HCO<sub>2</sub><sup>-</sup>) is subtracted, yielding the overall change in free energy associated with hydride transfer to CO<sub>2</sub>, labeled as  $\Delta G_{\text{HCO}_2^-}$  (7). Some of the reported hydricities and associated reduction potentials are included in Figure **0.2**. Average  $E_{1/2}$  values were used to normalize the contribution to the reduction potential to the hydricity by metals that undergo two one-electron reductions and one two-electron reduction. The dashed line shows the point at which the transfer of a hydride to CO<sub>2</sub> in CH<sub>3</sub>CN is ergoneutral (44 kcal/mol).<sup>5</sup>

**Scheme 0.1:** Thermochemical cycle for the reduction of CO<sub>2</sub> with a metal hydride

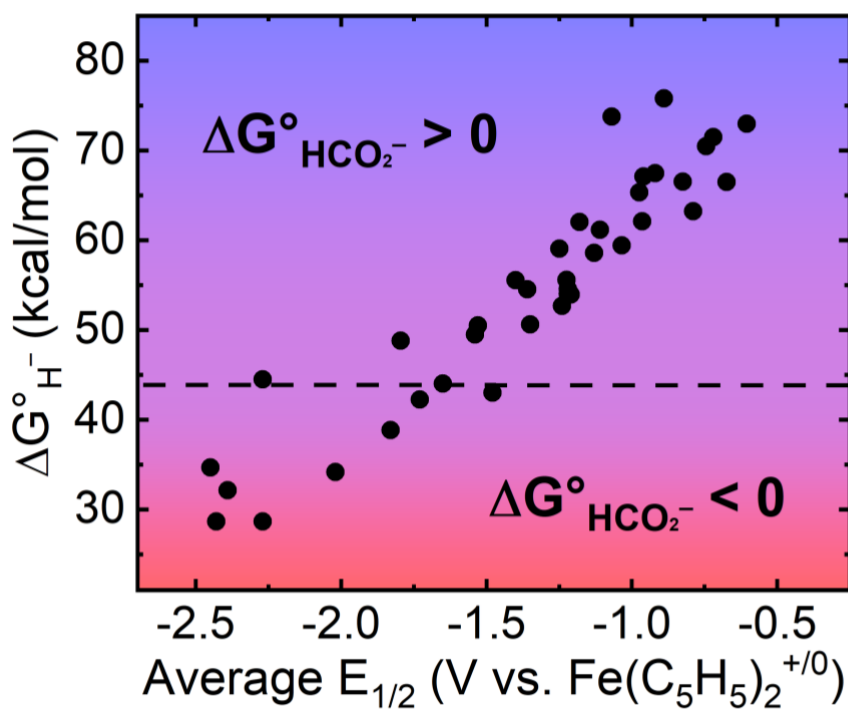
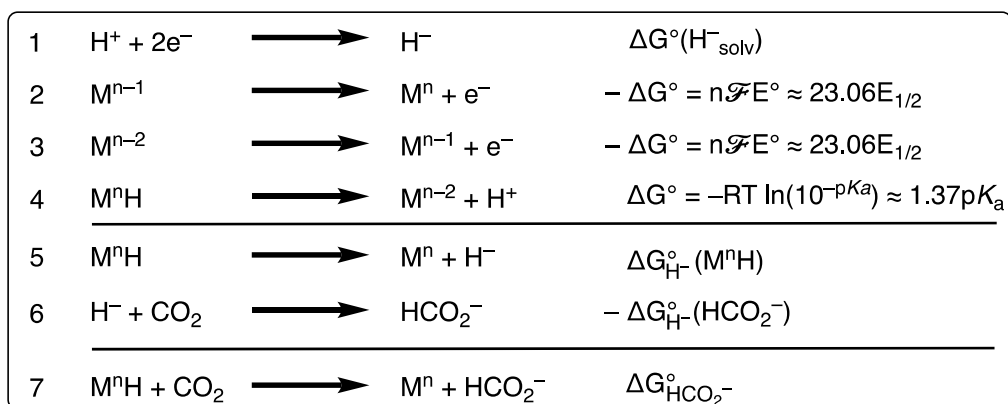


**Figure 0.2:** Average reduction potentials have a linear relationship with hydricities in metal complexes (Adapted from J. Am. Chem Soc. 2020, **142**, 19438)

Notably, the reduction potential of the metal center is strongly correlated with the complex's hydricity. To probe these observations further, the contributions of each of the elementary thermodynamic steps for some of the hydrides with reported  $\text{p}K_a$  and  $E_{1/2}$  values were separated and are shown in Figure 0.3. With a clearer picture of what is driving the reactivity here, we see that for all hydrides, the reduction potential contributes heavily to the overall calculated hydricity. In fact, the contribution by the  $\text{p}K_a$  has the opposite trend where if the

hydride is more basic, more energy is required to overcome the energy from the very downhill protonation reaction. In other words, all of the energy that was given off in the protonation step must be repaid by the contribution to the hydricity by the reduction potential.

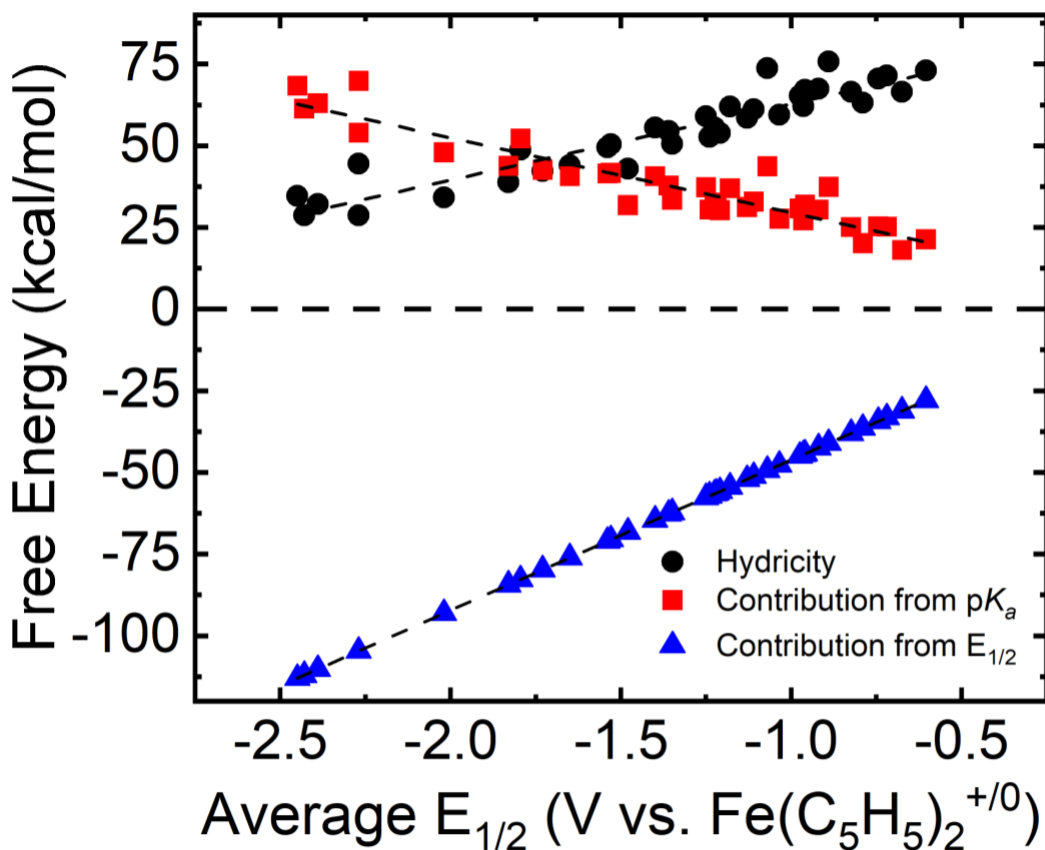


**Figure 0.3:** Energetic contributions from the  $pK_a$  and the  $E_{1/2}$  on the hydricity of a metal complex

With the energetic requirements in mind, how can we maximize overall energetic efficiency while maintaining catalytic turnover frequencies that are useful? Cunningham et al. used these principles in the development of the first synthetic example of reversible catalytic system for the interconversion of  $\text{CO}_2$  and  $\text{HCO}_2^-$  and achieving a 48 mV overpotential but with an observed turnover frequency of only  $1.0(1) \text{ hr}^{-1}$  for  $\text{CO}_2$  reduction under catalytic conditions.<sup>13,14</sup> This is greatly contrasted in work by Hirst and coworkers that showed reversible catalysis in an enzyme dissolved in solution and immobilized on an electrode.<sup>16</sup> With a tungsten-containing formate dehydrogenase (FDH1, isolated from *S. fumaroxidans*), the best rates of catalysis are

shown in **Table 0.1**. In the enzymatic system, reversible catalysis proceeds at least 5 orders of magnitude faster than the synthetic example.

**Table 0.1:** Turnover frequencies for reported studies on catalysis with FDH

	<i>Turnover Frequencies (s<sup>-1</sup>)</i>	
	<i>Soluble</i>	<i>Immobilized</i>
<i>CO<sub>2</sub> reduction</i>	282 <sup>a</sup>	112 <sup>b</sup>
<i>HCO<sub>2</sub><sup>-</sup> oxidation</i>	3380 <sup>a</sup>	700 <sup>c</sup>

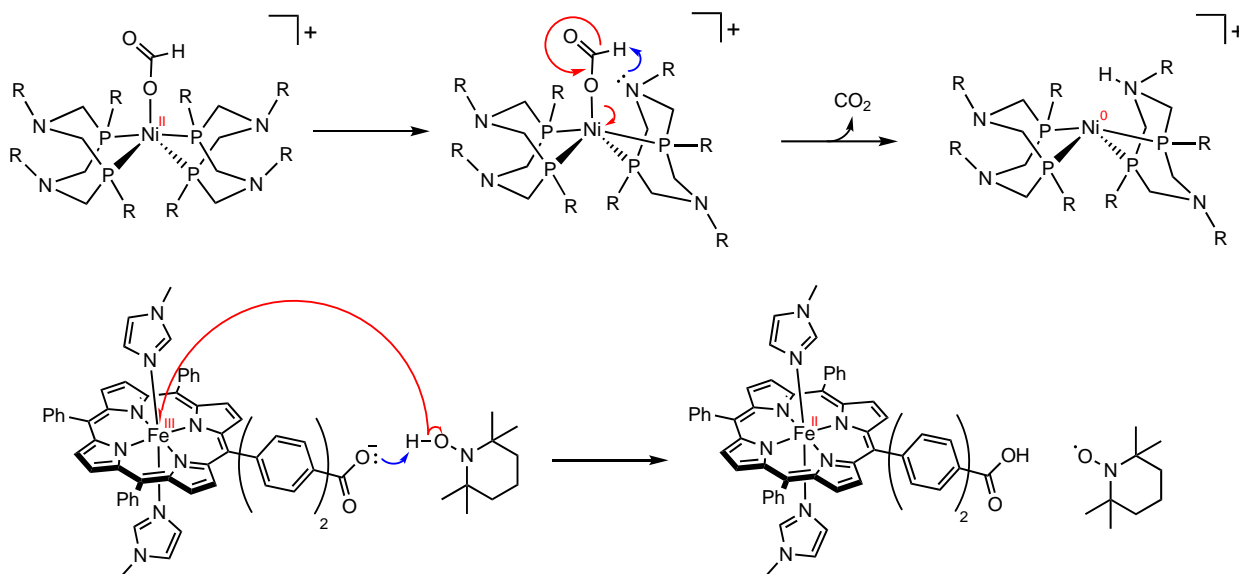
<sup>a</sup>pH 7.5 with methylviologen  
<sup>b</sup>pH 5.9  
<sup>c</sup>pH 8.0

Biological systems have had millions if not billions of years to optimize the reactivity of enzymes through natural selection, and understanding the mechanisms behind many enzymatic systems is exceedingly difficult. Nicks and Hille reviewed a series of proposed mechanisms of the Mo- and W-containing formate dehydrogenases.<sup>17-22</sup> Interestingly, there have been no experimentally supported mechanisms that involved a metal hydride (only one computational study).<sup>23</sup> Other systems like hydrogenases are thought to go through metal hydride intermediates that are often stabilized by a nearby metal.<sup>24</sup> All of the experimentally supported mechanisms for formate dehydrogenase enzymes involve the transfer of a hydride *equivalent* over the course of the reaction. The fate of the proton in the formate oxidation reaction is under scrutiny, but all mechanisms point to a two-electron reduction of the metal center. With no experimentally supported Mo or W hydrides, the proton and electrons become physically separated after the formal hydride transfer from formate. This decoupling of electron and proton equivalents is proposed in a synthetic system where HCO<sub>2</sub><sup>-</sup> is oxidized to CO<sub>2</sub> in a Ni bisdiphosphene system with pendant amines. The basic amine accepts the proton while the Ni center accepts the two electrons<sup>25</sup> (Scheme **0.2**, top). The proton and electron were also separated in hydrogen atom transfer from TEMPOH to a carboxylate 14 Å away from the Fe<sup>III</sup> center that is subsequently reduced to Fe<sup>II</sup> (Scheme **0.2**, bottom).<sup>26</sup> This example is particularly interesting because it uses a relatively acidic proton acceptor, a carboxylate. By separating the proton and electrons, the energy contribution from the p*K<sub>a</sub>* and from the reduction potential become partially decoupled, allowing



for individual tuning of each parameter. Tuning the reduction potentials to more negative potentials will generate stronger hydrides, and tuning the complex to have a more acidic hydride will also generate stronger hydrides.

**Scheme 0.2:** Two systems showing decoupled proton-electron transfer



Looking back to Equation 4 and rearranging the data in Figure 0.3, we can see that there are large variations in  $pK_a$  and reduction potential that cancel out on systems with similar hydricities (Figure 0.4). This result shows that the  $pK_a$  of a metal hydride alone is not inextricably linked to the  $E_{1/2}$ , but there is a definite correlation. By providing some distance between the final resting place of the proton and the electrons, the acidity and the reduction potential of the metal center, this correlation may be broken entirely. In choosing a hydride for a reaction, this separation and decoupling of the acidity and reduction potential may also be useful in determining if the compound will be compatible with the other species in solution. For instance, if electrocatalysis is being attempted on a system that is very sensitive to reduction, a more acidic hydride may be selected to decrease the magnitude of the reduction potential needed to reduce the metal complex.

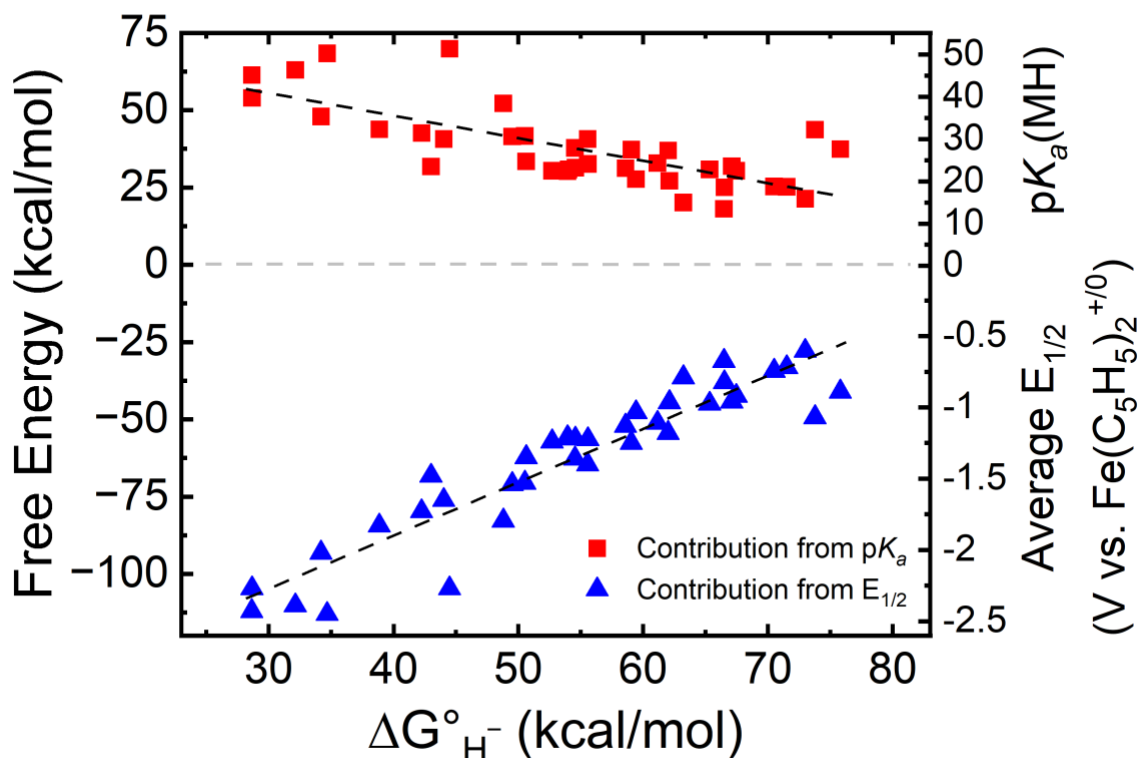


**Figure 0.4:** Alternate plot of the contributions of the  $pK_a$  and the  $E_{1/2}$  of the metal hydride to the hydricity

### Research Goals

The main motive for this dissertation is to use published empirical thermochemical data in the development of systems that (1) reduce  $\text{CO}_2$  at low overpotentials using orthogonal proton electron transfer, (2) reversibly interconvert  $\text{CO}$  and  $\text{CO}_2$ , and (3) convert  $\text{CO}_2$  to methanol using cascade catalysis. First, in studying a synthetic structural model of the active site of W-containing formate dehydrogenase, I present a series of experiments to isolate a protonated intermediate that was proposed to have the same protonation state and oxidation state as the reduced form of the enzyme active site. Through these studies, I show that the formation of a non-biologically relevant dimeric  $\text{W}^{\text{V}}$  compound is very favorable under many conditions and is the preferred decomposition product for many reactions involving either  $\text{W}^{\text{IV}}$  or  $\text{W}^{\text{VI}}$  starting materials.

In the second chapter, I attempt to use thermodynamic considerations to predict the reactivity of a cobalt macrocycle compound in the presence of CO<sub>2</sub> under reductive conditions. Small amounts of the desired reduction product, CO, was formed. However, subsequent unexpected reactivity of the fully reduced Co<sup>I</sup> compound yielded a Co<sup>II</sup> compound with multiple ligand oxidation and reduction reactions. With the unexpected reactivity, further thermochemical studies became unfeasible.

In the third and final chapter, I describe activation of formate for a proposed cascade catalytic cycle for CO<sub>2</sub> reduction to methanol. Use of nonpolar solvents for these reactions is both a drawback and an advantage. Nonpolar solvents like THF lack broadly applicable and self-consistent thermodynamic constants that are necessary to predict the reactivity of metal hydrides. Many pK<sub>a</sub> values reported in nonpolar solvents include separate entries for the donation of a proton in the presence of ions that subsequently pair with the resulting charged molecules as the reactions proceed. Because these processes are not entirely predictable, the reactivity of salts in THF becomes unpredictable as well. Although not explored here, the thermodynamics of these ion pairing interactions have been studied in the context of hydricity<sup>15</sup> and will continue to develop as we start to understand the quantification of the energies of these processes.

## *References*

- (1) Yang, J. Y.; Kerr, T. A.; Wang, X. S.; Barlow, J. M. Reducing CO<sub>2</sub> to HCO<sub>2</sub><sup>-</sup> at Mild Potentials: Lessons from Formate Dehydrogenase. *J. Am. Chem. Soc.* **2020**. <https://doi.org/10.1021/jacs.0c07965>.
- (2) Nations, U. *World population to reach 8 billion on 15 November 2022*. United Nations. <https://www.un.org/en/desa/world-population-reach-8-billion-15-november-2022> (accessed 2022-11-24).

- (3) Tong, D.; Farnham, D. J.; Duan, L.; Zhang, Q.; Lewis, N. S.; Caldeira, K.; Davis, S. J. Geophysical Constraints on the Reliability of Solar and Wind Power Worldwide. *Nat Commun* **2021**, *12* (1), 6146. <https://doi.org/10.1038/s41467-021-26355-z>.
- (4) Durbin, D. J.; Malardier-Jugroot, C. Review of Hydrogen Storage Techniques for on Board Vehicle Applications. *International Journal of Hydrogen Energy* **2013**, *38* (34), 14595–14617. <https://doi.org/10.1016/j.ijhydene.2013.07.058>.
- (5) Wiedner, E. S.; Chambers, M. B.; Pitman, C. L.; Bullock, R. M.; Miller, A. J. M.; Appel, A. M. Thermodynamic Hydricity of Transition Metal Hydrides. *Chem. Rev.* **2016**, *116* (15), 8655–8692. <https://doi.org/10.1021/acs.chemrev.6b00168>.
- (6) Bordwell, F. G. Equilibrium Acidities in Dimethyl Sulfoxide Solution. *Acc. Chem. Res.* **1988**, *21* (12), 456–463. <https://doi.org/10.1021/ar00156a004>.
- (7) Tsay, C.; Livesay, B. N.; Ruelas, S.; Yang, J. Y. Solvation Effects on Transition Metal Hydricity. *J. Am. Chem. Soc.* **2015**, *137* (44), 14114–14121. <https://doi.org/10.1021/jacs.5b07777>.
- (8) Tsay, C.; Yang, J. Y. Electrocatalytic Hydrogen Evolution under Acidic Aqueous Conditions and Mechanistic Studies of a Highly Stable Molecular Catalyst. *J. Am. Chem. Soc.* **2016**, *138* (43), 14174–14177. <https://doi.org/10.1021/jacs.6b05851>.
- (9) Ceballos, B. M.; Tsay, C.; Yang, J. Y. CO<sub>2</sub> Reduction or HCO<sub>2</sub><sup>–</sup> Oxidation? Solvent-Dependent Thermochemistry of a Nickel Hydride Complex. *Chem. Commun.* **2017**, *53* (53), 7405–7408. <https://doi.org/10.1039/C7CC02511D>.
- (10) Ceballos, B. M.; Yang, J. Y. Directing the Reactivity of Metal Hydrides for Selective CO<sub>2</sub> Reduction. *PNAS* **2018**, *115* (50), 12686–12691. <https://doi.org/10.1073/pnas.1811396115>.
- (11) Tsay, C.; Ceballos, B. M.; Yang, J. Y. PH-Dependent Reactivity of a Water-Soluble Nickel Complex: Hydrogen Evolution vs Selective Electrochemical Hydride Generation. *Organometallics* **2019**, *38* (6), 1286–1291. <https://doi.org/10.1021/acs.organomet.8b00558>.

- (12) Ceballos, B. M.; Yang, J. Y. Highly Selective Electrocatalytic CO<sub>2</sub> Reduction by [Pt(Dmpe)<sub>2</sub>]<sup>2+</sup> through Kinetic and Thermodynamic Control. *Organometallics* **2020**, *39* (9), 1491–1496. <https://doi.org/10.1021/acs.organomet.9b00720>.
- (13) Cunningham, D. W.; Barlow, J. M.; Velazquez, R. S.; Yang, J. Y. Reversible and Selective CO<sub>2</sub> to HCO<sub>2</sub><sup>-</sup> Electrocatalysis near the Thermodynamic Potential. *Angewandte Chemie International Edition* **2020**, *59* (11), 4443–4447. <https://doi.org/10.1002/anie.201913198>.
- (14) Cunningham, D. W.; Yang, J. Y. Kinetic and Mechanistic Analysis of a Synthetic Reversible CO<sub>2</sub>/HCO<sub>2</sub><sup>-</sup> Electrocatalyst. *Chem. Commun.* **2020**, *56* (85), 12965–12968. <https://doi.org/10.1039/DoCC05556E>.
- (15) Brereton, K. R.; Smith, N. E.; Hazari, N.; Miller, A. J. M. Thermodynamic and Kinetic Hydricity of Transition Metal Hydrides. *Chem. Soc. Rev.* **2020**, *49* (22), 7929–7948. <https://doi.org/10.1039/DoCS00405G>.
- (16) Reda, T.; Plugge, C. M.; Abram, N. J.; Hirst, J. Reversible Interconversion of Carbon Dioxide and Formate by an Electroactive Enzyme. *PNAS* **2008**, *105* (31), 10654–10658. <https://doi.org/10.1073/pnas.0801290105>.
- (17) Nicks, D.; Hille, R. Molybdenum- and Tungsten-Containing Formate Dehydrogenases and Formylmethanofuran Dehydrogenases: Structure, Mechanism, and Cofactor Insertion. *Protein Science* **2019**, *28* (1), 111–122. <https://doi.org/10.1002/pro.3498>.
- (18) Boyington, J. C.; Gladyshev, V. N.; Khangulov, S. V.; Stadtman, T. C.; Sun, P. D. Crystal Structure of Formate Dehydrogenase H: Catalysis Involving Mo, Molybdopterin, Selenocysteine, and an Fe<sub>4</sub>S<sub>4</sub> Cluster. *Science* **1997**, *275* (5304), 1305–1308. <https://doi.org/10.1126/science.275.5304.1305>.
- (19) Raaijmakers, H. C. A.; Romão, M. J. Formate-Reduced E. Coli Formate Dehydrogenase H: The Reinterpretation of the Crystal Structure Suggests a New Reaction Mechanism. *J Biol Inorg Chem* **2006**, *11* (7), 849–854. <https://doi.org/10.1007/s00775-006-0129-2>.

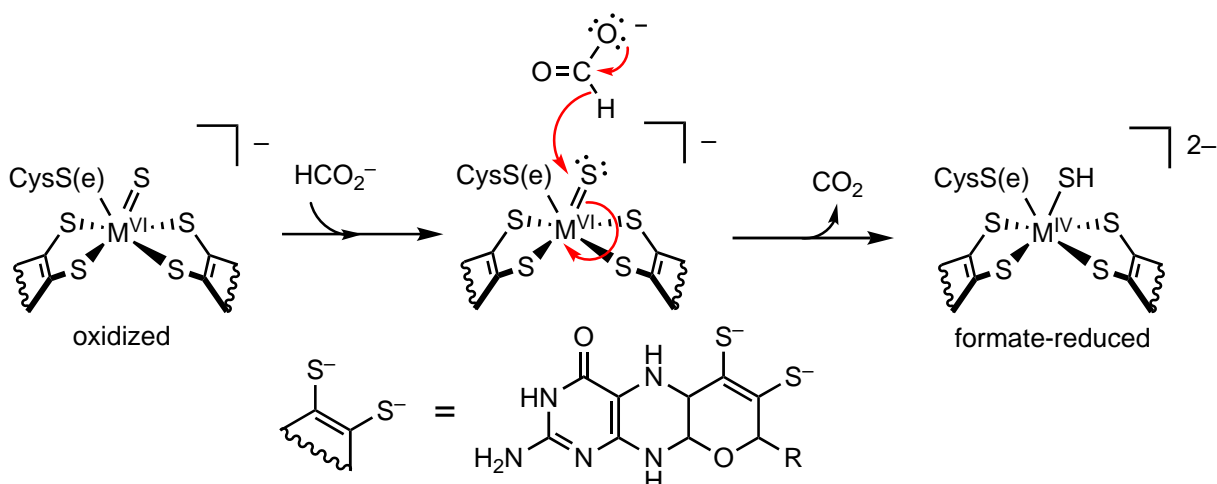
- (20) Hartmann, T.; Schrapers, P.; Utesch, T.; Nimtz, M.; Rippers, Y.; Dau, H.; Mroginski, M. A.; Haumann, M.; Leimkühler, S. The Molybdenum Active Site of Formate Dehydrogenase Is Capable of Catalyzing C–H Bond Cleavage and Oxygen Atom Transfer Reactions. *Biochemistry* **2016**, *55* (16), 2381–2389. <https://doi.org/10.1021/acs.biochem.6b00002>.
- (21) Niks, D.; Duvvuru, J.; Escalona, M.; Hille, R. Spectroscopic and Kinetic Properties of the Molybdenum-Containing, NAD<sup>+</sup>-Dependent Formate Dehydrogenase from *Ralstonia Eutropha*. *J. Biol. Chem.* **2016**, *291* (3), 1162–1174. <https://doi.org/10.1074/jbc.M115.688457>.
- (22) Robinson, W. E.; Bassegoda, A.; Reisner, E.; Hirst, J. Oxidation-State-Dependent Binding Properties of the Active Site in a Mo-Containing Formate Dehydrogenase. *J. Am. Chem. Soc.* **2017**, *139* (29), 9927–9936. <https://doi.org/10.1021/jacs.7b03958>.
- (23) Tiberti, M.; Papaleo, E.; Russo, N.; De Gioia, L.; Zampella, G. Evidence for the Formation of a Mo–H Intermediate in the Catalytic Cycle of Formate Dehydrogenase. *Inorg. Chem.* **2012**, *51* (15), 8331–8339. <https://doi.org/10.1021/ic300863d>.
- (24) Schilter, D.; Camara, J. M.; Huynh, M. T.; Hammes-Schiffer, S.; Rauchfuss, T. B. Hydrogenase Enzymes and Their Synthetic Models: The Role of Metal Hydrides. *Chem. Rev.* **2016**, *116* (15), 8693–8749. <https://doi.org/10.1021/acs.chemrev.6b00180>.
- (25) Galan, B. R.; Schöffel, J.; Linehan, J. C.; Seu, C.; Appel, A. M.; Roberts, J. A. S.; Helm, M. L.; Kilgore, U. J.; Yang, J. Y.; DuBois, D. L.; Kubiak, C. P. Electrocatalytic Oxidation of Formate by [Ni(PR<sub>2</sub>NR'<sub>2</sub>)<sub>2</sub>(CH<sub>3</sub>CN)]<sub>2</sub><sup>+</sup> Complexes. *J. Am. Chem. Soc.* **2011**, *133* (32), 12767–12779. <https://doi.org/10.1021/ja204489e>.
- (26) Warren, J. J.; Menzeleev, A. R.; Kretchmer, J. S.; Miller, T. F.; Gray, H. B.; Mayer, J. M. Long-Range Proton-Coupled Electron-Transfer Reactions of Bis(Imidazole) Iron Tetraphenylporphyrins Linked to Benzoates. *J. Phys. Chem. Lett.* **2013**, *4* (3), 519–523. <https://doi.org/10.1021/jz400029w>.

# Chapter 1: Protonation-Induced Oxidation and Dimerization of a Tungsten Bisdithiolene Complex

## *Introduction*

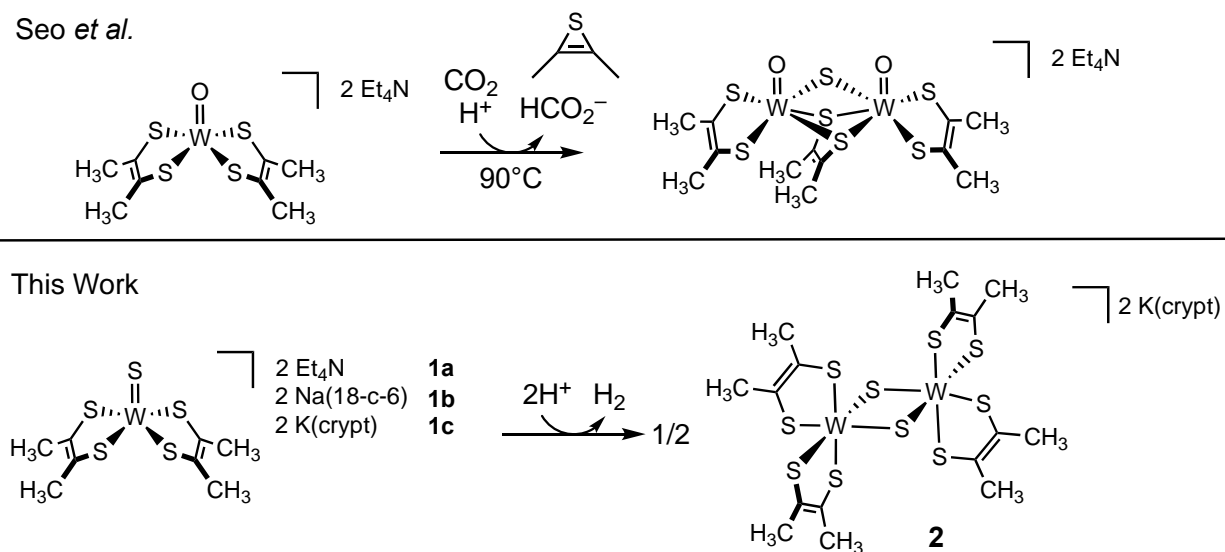
Formate ( $\text{HCO}_2^-$ ) is the product of the reduction of carbon dioxide with a hydride. Formate can serve as a liquid storage medium for  $\text{H}_2$  at ambient pressures,<sup>1,2</sup> as a precursor to value-added chemicals,<sup>3</sup> and as a direct energy storage medium in a formate fuel cell.<sup>4</sup> A metal hydride intermediate is frequently invoked for synthetic catalysts that reduce  $\text{CO}_2$  to  $\text{HCO}_2^-$ .<sup>5</sup> However, in the enzymes that oxidize formate in biology, there is uncertainty on where and how the electrons and proton are transferred over the course of the reaction,<sup>6</sup> and there are few well-supported examples of metal hydrides in natural systems.<sup>7</sup> Understanding the mechanisms of  $\text{HCO}_2^-$  oxidation and  $\text{CO}_2$  reduction in nature can help inspire the design of efficient catalysts for these transformations.

In methylotrophs, organisms that consume and metabolize  $\text{C}_1$  substrates, the formate dehydrogenase (FDH) family of enzymes catalyzes hydride abstraction from  $\text{HCO}_2^-$  to form  $\text{CO}_2$  and the hydride-reduced enzyme active site.<sup>8</sup> Enzymes involved in carbon catabolism have evolved to function at or near the thermodynamic potential of the given reaction. Thus, these enzymes are capable of performing not only  $\text{HCO}_2^-$  oxidation, but also  $\text{CO}_2$  reduction, albeit at a slower rate ( $1500 \text{ s}^{-1}$  and  $500 \text{ s}^{-1}$  respectively for tungsten-containing *S. fumarooxidans* FDH1).<sup>9</sup> A popular proposed mechanism of this reaction involves the transfer of the formate hydride to the molybdenum or tungsten active site as shown in Scheme 1.1.<sup>10</sup>



**Scheme 1.1:** Structure of the oxidized and the formate-reduced active site of a typical FDH where M= Mo, W

Both five- and six-coordinate structural analogues of these tungsten and molybdenum-containing active sites have been developed,<sup>11–17</sup> but formal hydride transfers have only been observed in one example (Scheme 1.2, top),<sup>18</sup> a noncatalytic system where formate was generated from CO<sub>2</sub> at 2 atm at 90°C in the presence of acid. Efficient handling of the protons and electrons in catalytic systems is essential to the function of reversible enzymes and molecular catalysts.<sup>19–21</sup> Here, we study the proton reactivity of three salts of the five-coordinate [W(S<sub>2</sub>C<sub>2</sub>(CH<sub>3</sub>)<sub>2</sub>)<sub>2</sub>]<sup>2-</sup> dianion (Scheme 1.2, bottom).



**Scheme 1.2:** Reactivity shown by Seo *et al.* and reactivity shown here



## Experimental

### General Methods

All manipulations were carried out in open air unless otherwise specified. All reactions with  $P_2S_5$  were performed with two consecutive bleach bubblers in order to neutralize the  $H_2S$  that was released. For manipulations carried out in an inert atmosphere glove box or using standard Schlenk technique, all solid chemicals were dried in vacuo prior to use, and all solvents were dried by passing over a column of molecular sieves or activated alumina and degassed by sparging with Ar. All chemicals were used as received from the supplier unless otherwise specified. Room temperature absorption spectra were collected using a Cary 60 spectrophotometer with fiber-optic connections to a quartz cell in an inert atmosphere glove box. Electronic absorption spectra collected at  $50^\circ C$  were collected on an 8453 Agilent UV-Vis spectrometer with an Unisoku Unispeks cryostat. IR spectra were determined using a Nicolet IS5 FT-IR spectrometer with ID5 ATR attachment in an inert atmosphere glove box or a Shimadzu IRAffinity-1S with ATR attachment in air.  $Ni(S_2C_2(CH_3)_2)_2$ ,<sup>22</sup>  $Et_4NSH$ ,<sup>23</sup>  $W(CO)_3(NCCH_3)_3$ ,<sup>24</sup>  $W(CO)_2(S_2C_2(CH_3)_2)_2$ ,<sup>11</sup> and **1a**<sup>25</sup> were synthesized according to published procedures.  $Ni(dppe)_2(BF_4)_2$  was synthesized by Janice Wong according to literature procedures.

### Synthesis of $[Na(18\text{-crown-6})]_2[WS(S_2C_2(CH_3)_2)_2]$ (**1b**)

In an inert atmosphere glove box filled with  $N_2$ , 20 mg of  $W(CO)_2(S_2C_2(CH_3)_2)_2$  was dissolved in 1 mL THF. In a separate container, 4.7 mg of NaSH and 22.2 mg of 18-crown-6 were suspended in 1 mL of  $CH_3CN$ . The solutions were mixed and stirred for 12 hours. The solution turned to a dark brown color. The solvent was removed, and the solid was redissolved in  $CH_3CN$  and layered with ether, affording 40 mg (93%) of brown crystalline  $[Na(18\text{-crown-6})]_2[WS(S_2C_2(CH_3)_2)_2]$ .  $^1H$  NMR ( $CD_3CN$ , 500 MHz) 2.43 (s, 12H,  $CH_3$ ).  $^{13}C\{^1H\}$  NMR ( $CD_3CN$ , 126 MHz, 233K) 141.91 ( $S_2C_2CH_3$ ), 21.55 ( $S_2C_2CH_3$ ).

### Synthesis of [K(2.2.2-cryptand)]<sub>2</sub>[WS(S<sub>2</sub>C<sub>2</sub>(CH<sub>3</sub>)<sub>2</sub>)] (**1c**)

In an inert atmosphere glove box filled with N<sub>2</sub>, 100 mg of W(CO)<sub>2</sub>(S<sub>2</sub>C<sub>2</sub>(CH<sub>3</sub>)<sub>2</sub>)<sub>2</sub> was dissolved in 5 mL THF. In a separate container, 30.5 mg of KSH and 158 mg of 2.2.2-cryptand were suspended in 5 mL of CH<sub>3</sub>CN. The solutions were mixed, and it was allowed to stir for 12 hours. The solution turned to a dark brown color. The solvent was removed, and the solid was redissolved in CH<sub>3</sub>CN and layered with ether and filtered, affording 230 mg (85%) of brown crystalline [K(2.2.2-cryptand)]<sub>2</sub>[WS(S<sub>2</sub>C<sub>2</sub>(CH<sub>3</sub>)<sub>2</sub>)<sub>2</sub>]. <sup>1</sup>H NMR (CD<sub>3</sub>CN, 500 MHz) 2.44 (br s, 12H, CH<sub>3</sub>).

### Synthesis of [K(2.2.2-cryptand)]<sub>2</sub>[WS(S<sub>2</sub>C<sub>2</sub>(CH<sub>3</sub>)<sub>2</sub>)<sub>2</sub>] (**2**)

In an inert atmosphere glove box filled with N<sub>2</sub>, 23.6 mg of **1c** was dissolved in 5 mL CH<sub>3</sub>CN. 8.6 mg of [Fe(C<sub>5</sub>(CH<sub>3</sub>)<sub>5</sub>)] [OTf] dissolved in 1 mL CH<sub>3</sub>CN was added to the tungsten compound yielding a black solution. The reaction was allowed to proceed for 10 minutes, and the solvent was removed *in vacuo*. The solid was extracted and filtered sequentially through a pipette filter with 10 mL Et<sub>2</sub>O, 10 mL THF, and 20 mL CH<sub>3</sub>CN. The volume of the CH<sub>3</sub>CN fraction was reduced to 1 mL *in vacuo*, and **2** was precipitated from solution with 15 mL Et<sub>2</sub>O. 14.2 mg (89% yield) of **2** was isolated in the form of a black powder. The structure of **2** was confirmed by X-ray crystallography. <sup>1</sup>H NMR (CD<sub>3</sub>CN, 500 MHz) 2.26 (br s, 12H, CH<sub>3</sub>). <sup>13</sup>C{<sup>1</sup>H} NMR (CD<sub>3</sub>CN, 126 MHz) 140.37 (S<sub>2</sub>C<sub>2</sub>CH<sub>3</sub>), 20.63 (S<sub>2</sub>C<sub>2</sub>CH<sub>3</sub>).

### X-ray Absorption Measurements

X-ray absorption measurements around the W L<sub>3</sub> edge were performed by Mackenzie Field at the Stanford Synchrotron Radiation Laboratory (SSRL) on beam line 7-3 at ~ 10 K. The data were collected using a Si(220) φ = 0° double-crystal monochromator. Data sets were collected in fluorescence mode with a 30-element Ge detector. The sample position in the beam was adjusted after each scan so that a previously unexposed portion of the sample was examined.

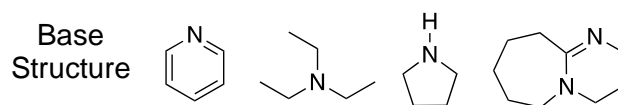
## EXAFS Fitting

The first shell (W-S) of the raw XAS data were fit over the region  $k=3-15 \text{ \AA}^{-1}$  in EXAFSPAK. The scale factor,  $S_0$ , was set to 0.9. Our EXAFS data were fit from  $k=3-15 \text{ \AA}^{-1}$ , giving a resolution of 0.13  $\text{\AA}$ . Energies were calibrated using an iron foil (7111.2 eV).

## Electrochemical Experiments

All electrochemical experiments were performed at 1.0 mM with 200 mM [ $n\text{Bu}_4\text{N}$ ][PF<sub>6</sub>] supporting electrolyte in room temperature CH<sub>3</sub>CN in an inert atmosphere glovebox unless otherwise noted. A 1 mm diameter glassy carbon disk was used as the working electrode with a glassy carbon rod as counter electrode. Measurements were performed against a Ag<sup>+0</sup> nonaqueous quasireference containing a Ag wire in 100 mM [ $n\text{Bu}_4\text{N}$ ][PF<sub>6</sub>] in CH<sub>3</sub>CN, separated from the analyte solution with a glass jacket and a Vycor<sup>TM</sup> frit affixed with PTFE shrink-wrap tubing. All potentials recorded were normalized to the Fe(C<sub>5</sub>H<sub>5</sub>)<sub>2</sub><sup>+0</sup> redox couple.

**Table 1.1:**  $pK_a$ s of relevant bases used in this chapter



Abbreviation	Py <sup>26</sup>	Et <sub>3</sub> N <sup>26</sup>	Pyr <sup>26</sup>	DBU <sup>26</sup>
$pK_a$ THF	5.5	12.5	13.5	16.9
$pK_a$ CH <sub>3</sub> CN	12.53	18.83	19.62	24.31

Note:  $pK_a$ s are reported as the  $pK_a$  of the conjugate acid, B•HOTf or B•HBF<sub>4</sub>. Values in THF do not include effects of ion pairing.

## Results and Discussion

### Synthesis and Characterization

Synthesis of reduced 5-coordinate [ $\text{Et}_4\text{N}$ ]<sub>2</sub>[W(S)(S<sub>2</sub>C<sub>2</sub>(CH<sub>3</sub>)<sub>2</sub>)<sub>2</sub>] (**1a**) was performed according to Holm and coworkers. A brown solid was isolated in 87% yield, and the observed NMR, IR, and electronic absorption spectra are consistent with literature.<sup>11,24,22,25</sup> The reduced complexes [Na(18-crown-6)]<sub>2</sub>[W(S)(S<sub>2</sub>C<sub>2</sub>(CH<sub>3</sub>)<sub>2</sub>)<sub>2</sub>] (**1b**) and [K(2.2.2-

cryptand)]<sub>2</sub>[W(S)(S<sub>2</sub>C<sub>2</sub>(CH<sub>3</sub>)<sub>2</sub>)<sub>2</sub>] (**1c**) were synthesized by stirring two equivalents of anhydrous NaSH and 18-crown-6 or anhydrous KSH and 2.2.2-cryptand (crypt) with W(CO)<sub>2</sub>(S<sub>2</sub>C<sub>2</sub>(CH<sub>3</sub>)<sub>2</sub>)<sub>2</sub>, which both formed the brown solid final products. The <sup>1</sup>H-NMR spectrum for **1b** (bottom) is shown alongside the <sup>1</sup>H-NMR spectra for **1a** (top) and **1c** (middle) in Figure 1.1. The <sup>1</sup>H-NMR spectrum for **1b** shows two resonances. One belongs to two 18-crown-6 molecules chelating sodium ions and the other for the methyl substituents on the anion, with a few minor solvent impurities. Notably, the resonance that is associated with the methyl groups on the anion is significantly sharper than either the Et<sub>4</sub>N<sup>+</sup> and K(crypt)<sup>+</sup> salts, suggesting that the sodium ion coordinated to the terminal sulfido group observed in the crystal structure (Figure 1.2A) also persists in solution, stabilizing the solid-state square pyramidal structure. The <sup>1</sup>H-NMR spectrum of **1c** as shown in Figure 1.1 (middle) shows three resonances for the 2.2.2-cryptand ligand with a very broad resonance near 2.6 ppm, which corresponds to the methyl groups on the anionic metal compound and is consistent with the Et<sub>4</sub>N<sup>+</sup> salt.

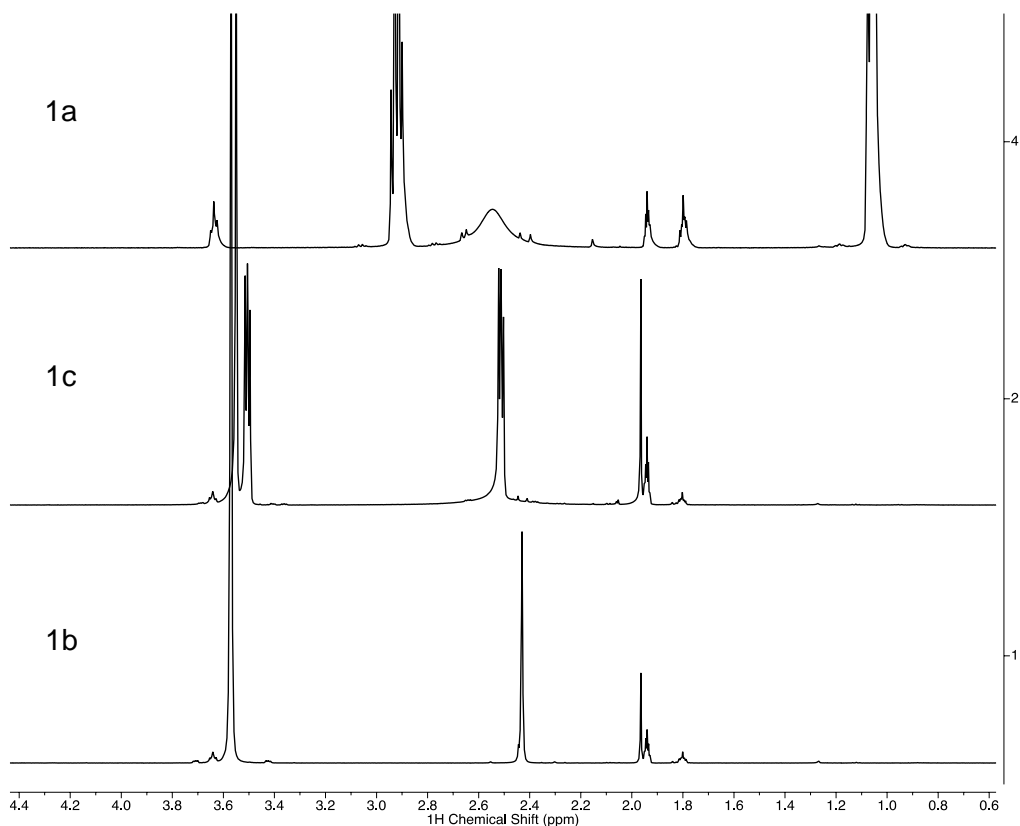


**Figure 1.1:**  $^1\text{H}$ -NMRs of **1a** (top), **1c** (middle), and **1b** (bottom)

Crystals of **1b** and **1c** were grown by vapor diffusion of diethyl ether into a  $\text{CH}_3\text{CN}$  solution of each. The solid-state structures of **1b** and **1c** are shown in Figure 1.2. Because the  $\text{K}^+$  ions are encapsulated, there is no interaction with the terminal sulfido. Even without the interaction with the cation, the square pyramidal structure persists in the solid state, which is consistent with the analogous phenyl substituted dithiolene complex by Holm and coworkers.<sup>11</sup> Low-temperature  $^1\text{H}$ -NMR spectra of **1a** feature sharper peaks corresponding to the dithiolene methyl groups, suggesting the broadness of the resonance is due to a fluxional process (Figure 1.3). Also, by cooling the solution to  $-40^\circ\text{C}$ , a  $^{13}\text{C}\{^1\text{H}\}$  NMR spectrum of **1a** was collected and shown in Figure 1.4.

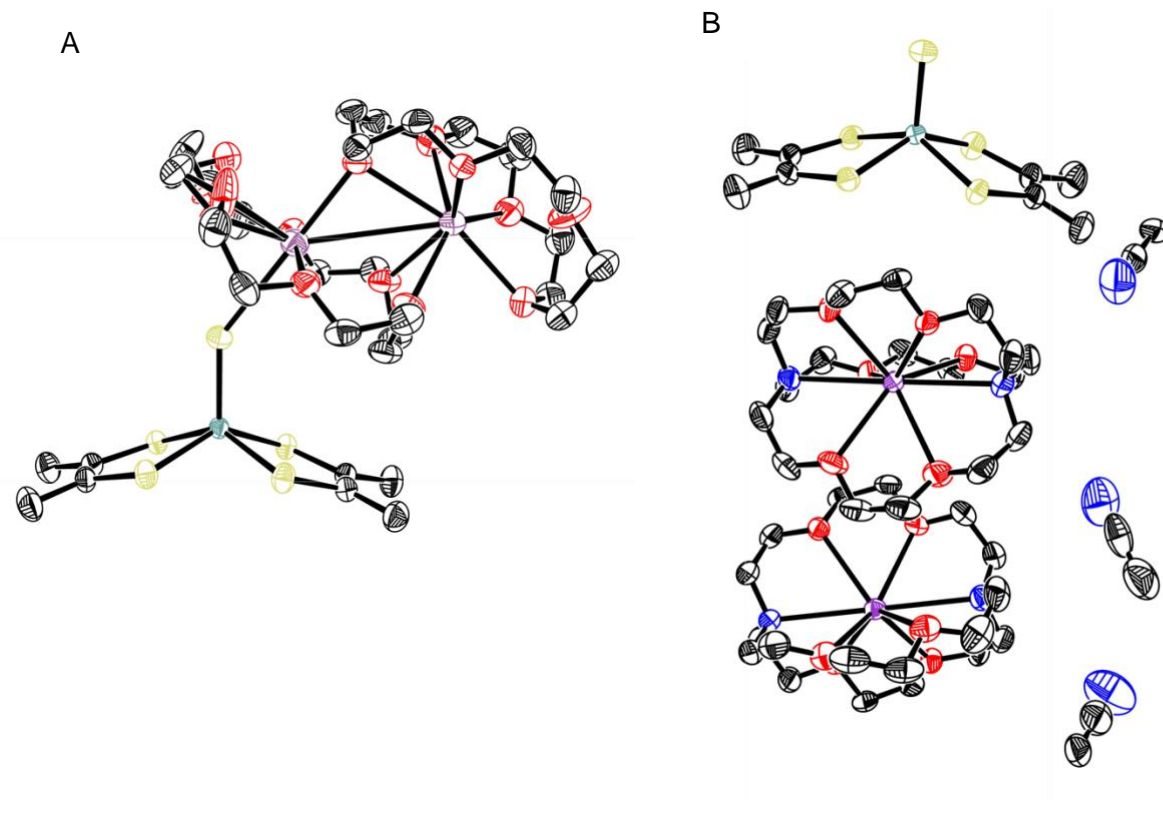


**Figure 1.2:** Solid state crystal structures of (A) **1b** and (B) **1c**. Thermal ellipsoids shown at 90%, hydrogen atoms removed for clarity.

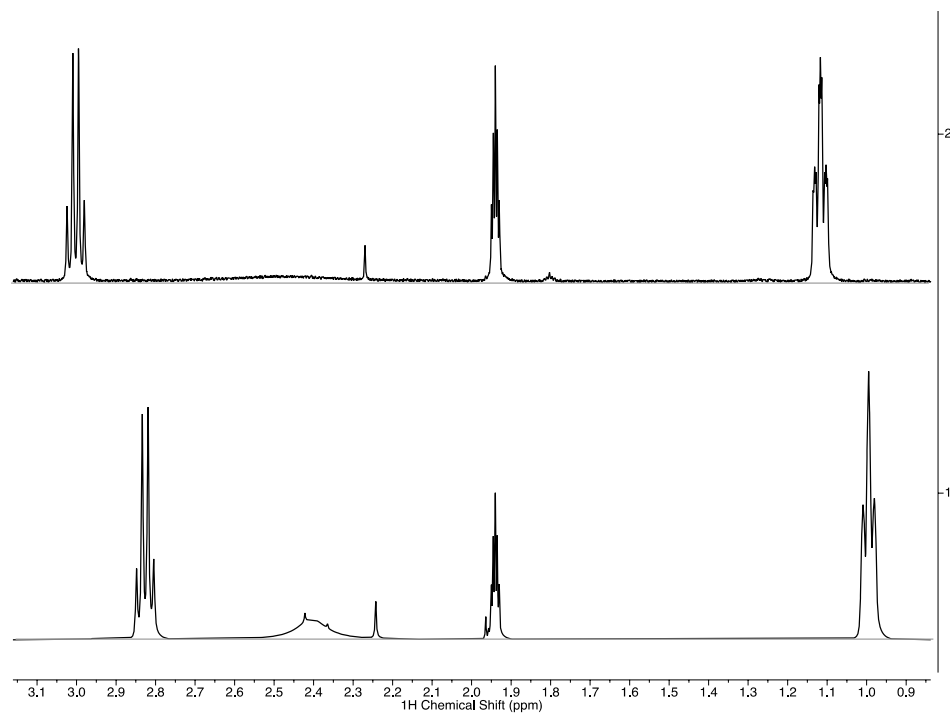


**Figure 1.3:** Room temperature (Top) and  $-40^{\circ}\text{C}$  (Bottom)  $^1\text{H}$ -NMR spectra of **1a**. Each example shows a small impurity ( $<5\%$ ) of what is likely **2**. A straight line is drawn across the baseline in each to guide the eye.

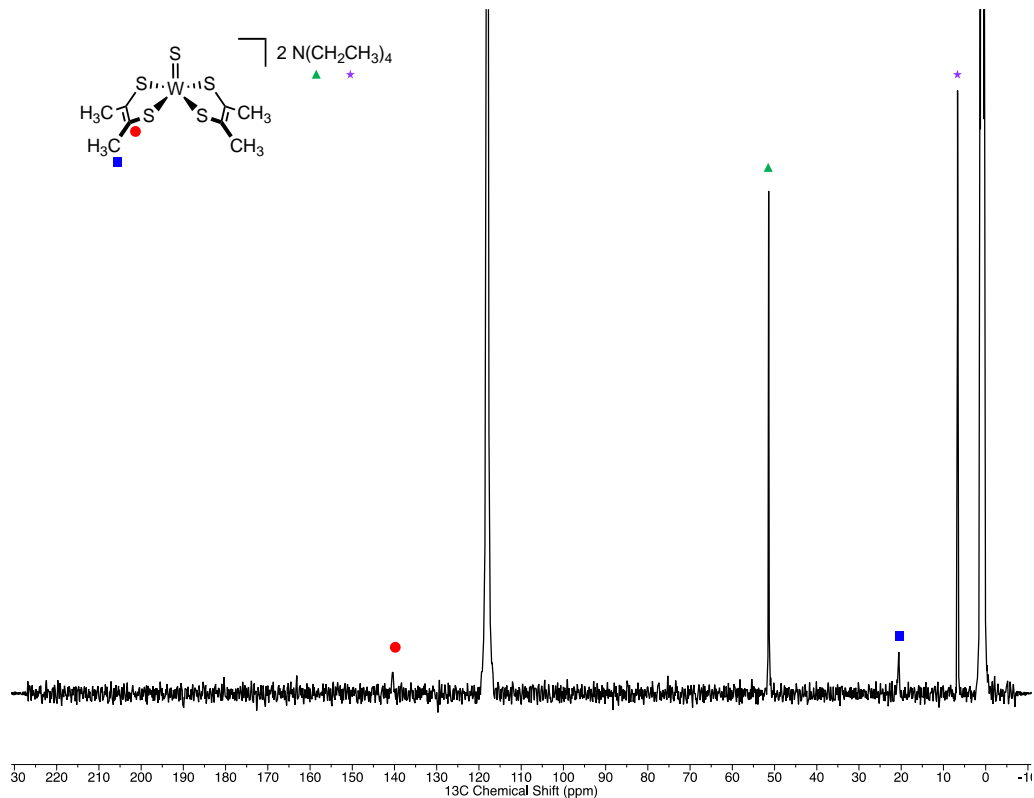


**Figure 1.4:** Low-temperature ( $-40^{\circ}\text{C}$ )  $^{13}\text{C}\{^1\text{H}\}$  NMR of **1a** in  $\text{CD}_3\text{CN}$

Independent synthesis of **2** was performed as a modification of the various synthetic techniques by Holm and coworkers.<sup>25</sup> Instead of  $I_2$  as an oxidant for **1c**, the  $K(\text{crypt})^+$  salt of the  $W^{IV}$  starting material was treated with one equivalent of  $Fe(C_5(CH_3)_5)_2OTf$  to afford an 89% yield of **2**. X-ray diffraction quality crystals were grown by slow diffusion of  $Et_2O$  into a concentrated solution of **2** in  $CH_3CN$ . The structure of **2** was confirmed by single crystal X-ray crystallography.

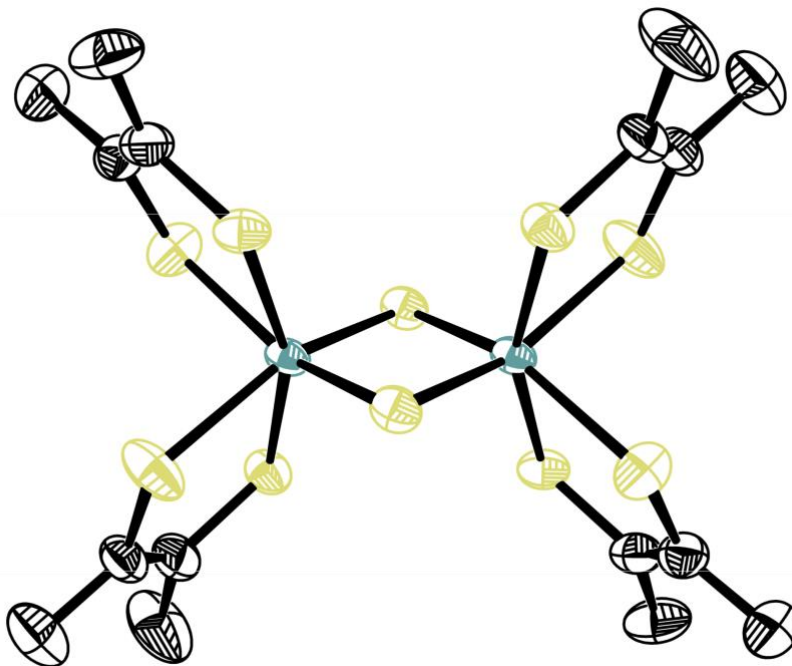


**Figure 1.5:** Solid state crystal structure of **2**. Thermal ellipsoids shown at 90%. Hydrogen atoms and counterions removed for clarity.

The crystal structure of **2** is shown in Figure 1.5. The structure, which contains two  $[K(\text{crypt})]^+$  units confirms that the dimeric tungsten complex is a dianion, pointing to a formally  $W^V$  dimer. Further NMR characterization with no evidence for paramagnetic species in solution suggests this is an antiferromagnetically coupled,  $S=0$  system. The structure in Figure 1.5 is nearly identical to the structure of  $[Et_4N]_2[W(S_2C_2(CH_3)_2)_2]_2$  published by Holm and coworkers. Selected bond metrics for **2** and  $[Et_4N]_2[W(S_2C_2(CH_3)_2)_2]_2$  are shown in Table 1.3 along with selected bond metrics from **1b** and **1c**. There are no major differences between **1c** and **1b** other than their  $\tau_5$  parameter. Both values are close to 0, confirming their near square pyramidal structure, but



having the sodium cation bound to the terminal sulfido (Na-S 2.913Å) further enforces the square pyramidal structure in the solid state for **1b**. The square-pyramidal structure likely persists in solution according to the sharp resonance corresponding to the ligand methyl groups in the <sup>1</sup>H-NMR compared with the others without a cation bound in the solid state.

**Table 1.2:** Bond metrics of crystallized tungsten bisdithiolene species.

	<b>1c</b>	<b>1b</b>	<b>2</b>	<i>[Et<sub>4</sub>N]<sub>2</sub>2<sup>a</sup></i>
<i>W-S<sub>ax</sub><sup>b</sup></i>	2.1818(4)	2.1881(6)	2.3279(5)	2.330(2)
<i>W-S<sub>2</sub></i>	2.3543(4)	2.3513(5)	2.3930(6) <sup>c</sup>	2.382(2) <sup>c</sup>
<i>W-S<sub>3</sub></i>	2.3565(4)	2.3571(6)	2.4362(6) <sup>d</sup>	2.453(2) <sup>d</sup>
<i>W-S<sub>4</sub></i>	2.3506(4)	2.3546(6)	2.4357(9) <sup>d</sup>	2.432(2) <sup>d</sup>
<i>W-S<sub>5</sub></i>	2.3560(4)	2.3594(5)	2.3972(6) <sup>c</sup>	2.391(2) <sup>c</sup>
<i>W-W</i>	---	---	2.9787(5)	3.000(1)
<i>W-S-W</i>	---	---	79.48	79.84
<i>τ<sub>5</sub></i>	0.042	0.0087	---	---
<i>C-C</i>	1.332(2), 1.338(2)	1.337(3), 1.337(3)	1.345(4) 1.349(3) <sup>e</sup>	1.330(9)

C-C bonds are the dithiolene backbone carbons

<sup>a</sup>From Ref. 25

<sup>b</sup>S<sub>5</sub> is the axial terminal sulfido for the monomeric complexes and the bridging sulfido for the dimeric complexes.

<sup>c</sup>Trans to dithiolene

<sup>d</sup>Trans to bridging sulfido

<sup>e</sup>Two sets of C-C bonds exist in this complex. The second set was symmetrically generated, thus omitted.

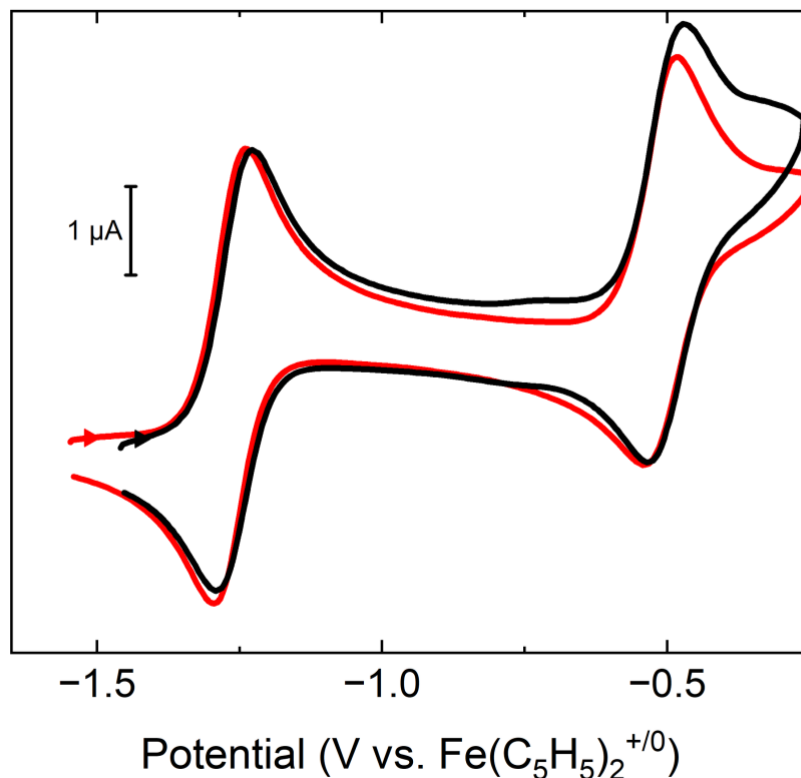
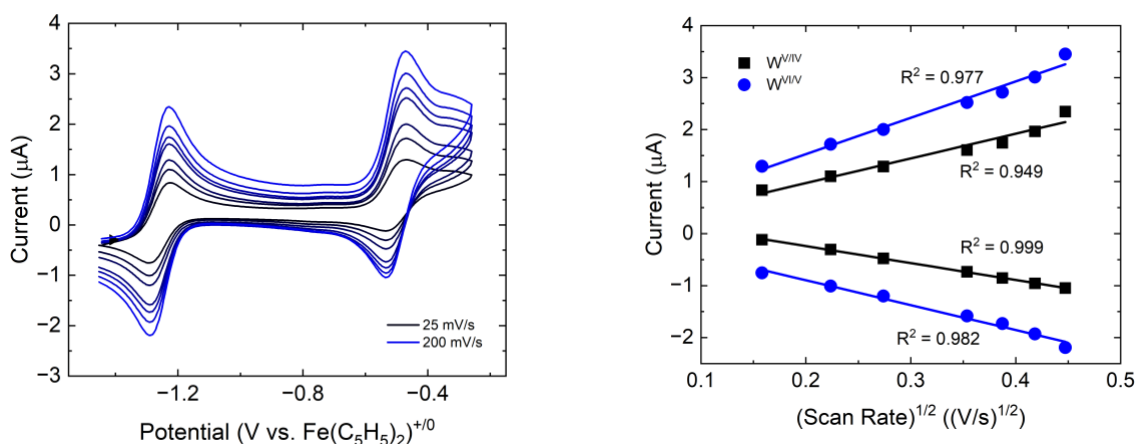
As expected, the bond length between *W* and S<sub>5</sub> increases about 0.15 Å upon dimerization due to the decreased bond order between the tungsten and the sulfur. The *W-S* bond lengths for the **2** and the Et<sub>4</sub>N<sup>+</sup> salt are all within 0.02 Å. The biggest difference is the *W-W* distance, which 0.021 Å shorter in the K(crypt)<sup>+</sup> salt, which is likely due to the temperature of data collection (213 K vs. 90 K here).

## Electrochemical Studies

Cyclic Voltammetry (CV) studies were performed on **1a** and **1c**. The reduction potentials of the W<sup>IV/V</sup> and W<sup>VI/V</sup> redox couples essentially overlay between the two salts. Scan rate dependent studies indicate diffusion-controlled processes (Figure 1.7 and Figure 1.8). The identical reduction potentials indicate that there is no interaction of the countercation with the anion at this concentration in CH<sub>3</sub>CN.

**Table 1.3:** Reduction potentials of tungsten compounds

	$E_{1/2} W^{VI/IV}$	$E_{1/2} W^{VI/V}$
<b>1a</b>	-1.259	-0.503
<b>1c</b>	-1.265	-0.508

**Figure 1.6:** Cyclic voltammogram of 1 mM **1a** (black) and **1c** (red) in CH<sub>3</sub>CN with 100 mM [nBu<sub>4</sub>N][PF<sub>6</sub>] as the supporting electrolyte, glassy carbon disc electrode, glassy carbon rod counter electrode, and Ag<sup>+/0</sup> pseudoreference at 100 mV/s.**Figure 1.7:** Scan-rate dependent cyclic voltammetry studies of **1a** (left). Scan rates shown were 25, 50, 75, 125, 150, 175, and 200 mV/s. The peak currents of the anodic and cathodic waves are shown on the right plotted against (scan rate)<sup>1/2</sup>. The W<sup>IV/V</sup> is shown as black squares, and the W<sup>VI/V</sup> couple is shown as blue circles. Linear regressions were performed on each peak at the various scan rates, and the R<sup>2</sup> values are reported next to the line.

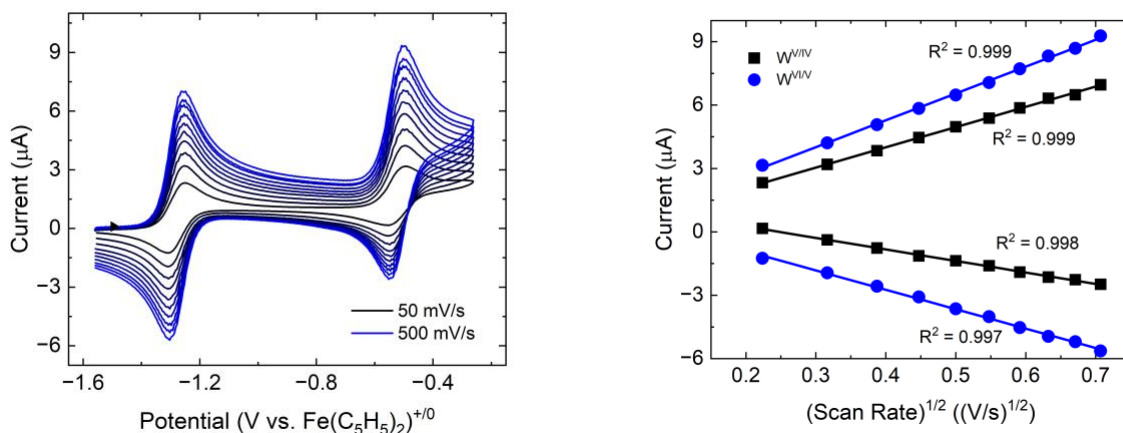


**Figure 1.8:** Scan-rate dependent cyclic voltammetry studies of **1c** (left). Scan rates shown were 50, 100, 150, 200, 250, 300, 350, 400, 450, and 500 mV/s. The peak currents of the anodic and cathodic waves are shown on the right plotted against  $(\text{scan rate})^{1/2}$ . The  $W^{IV/V}$  is shown as black squares, and the  $W^{VI/V}$  couple is shown as blue circles. Linear regressions were performed on each peak at the various scan rates, and the  $R^2$  values are reported next to the line.

Further electrochemical studies were performed on **2**, which had a quasireversible couple at  $-2.2$  V and a complicated oxidation event with anodic events at  $-0.52$  V and  $-0.33$  V, determined by a cycled differential pulse voltammetry experiment (Figure 1.10, bottom), which is a pulsed voltammetric technique that smoothes out the baseline of the cyclic voltammogram when multiple Faradaic events are present. When scan-rate dependent studies were performed on the reductive event, there was no major increase in the oxidative current, which may indicate instability of the reduced product. Also, when the currents are normalized to  $v^{1/2}$ , reversible redox couples under ideal conditions show that all traces overlap (Equation 1, the Randles-Ševčík equation).<sup>27</sup> However, in this case, the reductive event has a larger magnitude at slower scan rates. While diffusion at slow scan rates can cause an increase in the  $v^{1/2}$ -normalized current, it is not expected in this situation since the slowest scan rate is 100 mV/s. The oxidative event, however, does show a slight increase in current of the reduction following oxidation at 500 mV/s.

$$(1) i_p = 0.4463 (n\mathcal{F})^{3/2} AC \sqrt{\frac{vD}{RT}}$$

$i_p$  = peak current,  $n$  = number of electrons in redox event,  $\mathcal{F}$  = the Faraday constant,  $A$  = electrode area,  $C$  = analyte concentration,  $v$  = scan rate,  $D$  = diffusion coefficient,  $R$  = gas constant,  $T$  = temperature.

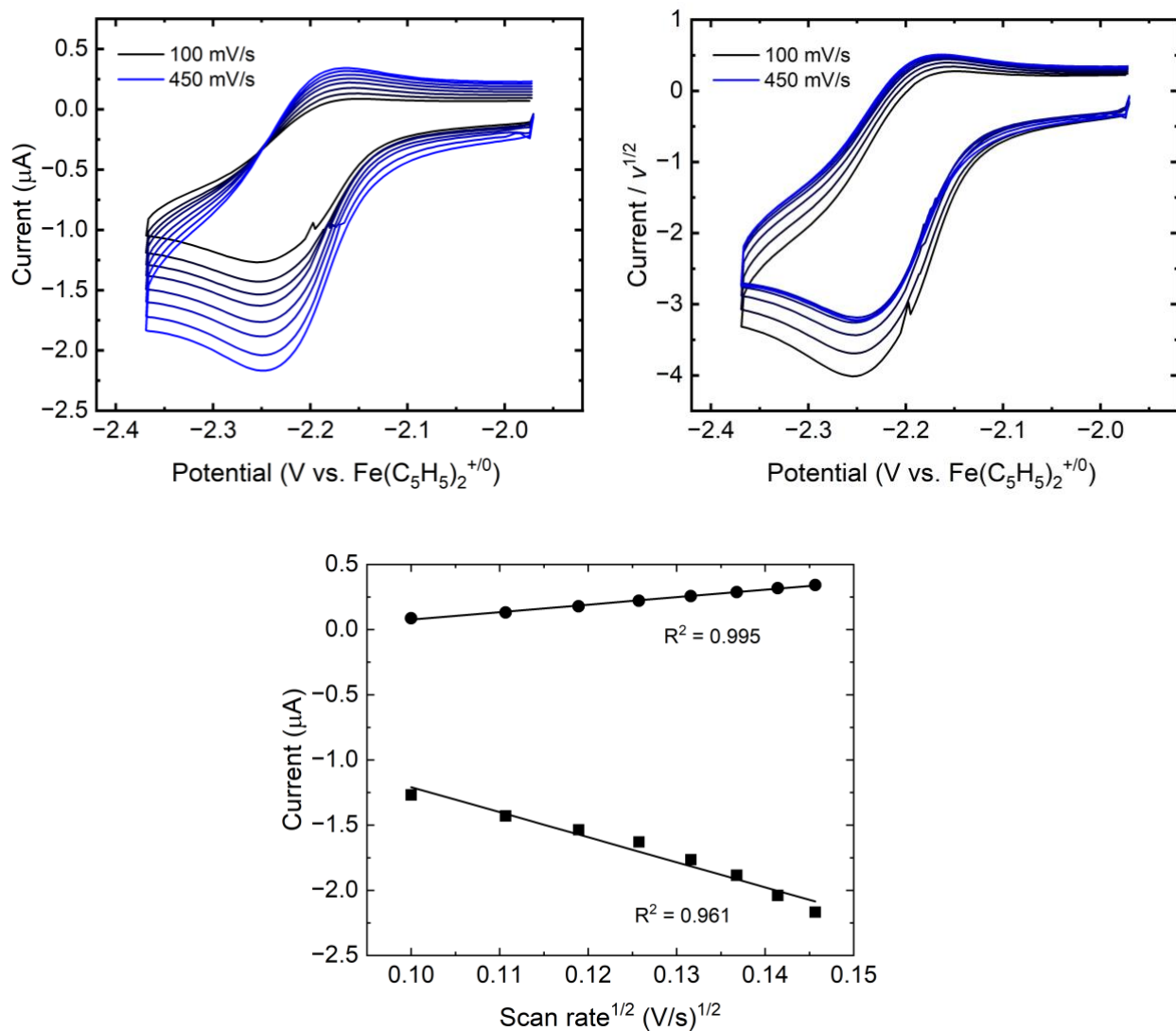


**Figure 1.9:** Scan-rate dependent studies on the reduction of **2**. Scan rates shown were performed at 100, 150, 200, 250, 300, 350, 400, and 450 mV/s. The top left panel shows current response, and the top right panel shows current response normalized to  $(\text{scan rate})^{1/2}$ . The bottom panel shows the peak currents of the anodic and cathodic waves plotted against  $(\text{scan rate})^{1/2}$ . Linear regressions were performed on each peak at the various scan rates, and the  $R^2$  values are reported next to the line.

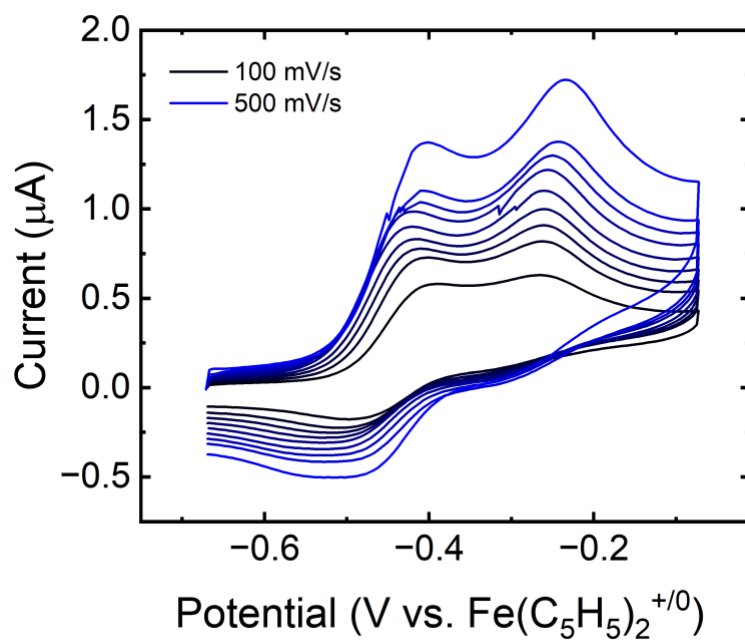


**Figure 1.10:** Scan-rate dependent studies on the oxidation of **2**. Scan rates shown were performed at 100, 150, 200, 250, 300, 350, 400, 450, and 500 mV/s, scanning anodically first.

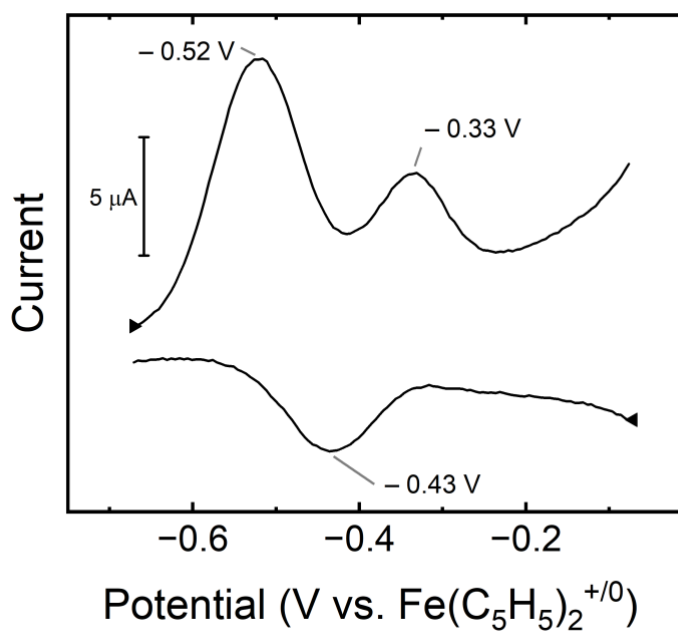


**Figure 1.11:** Cycled differential pulse voltammetry on the oxidation of **2**. Anodic sweep was performed first, followed immediately by the cathodic sweep.

## Protonation of $W^{IV}$ Salts

To access an oxidation and protonation state that is relevant to one of the resting states of the FDH enzyme, the reduced  $W^{IV}$  compound must either be protonated to form the formate-reduced resting state or be oxidized by two electrons to the fully oxidized  $W^{VI}$  state. Previous work by Holm and coworkers has shown that although the two one-electron oxidations of **1a** are reversible chemical oxidations with  $I_2$  results in the  $Et_4N^+$  salt of **2**, a dimeric  $W^V$  compound.<sup>25</sup> Because of the deleterious dimerization that occurs upon chemical oxidation, we treated the  $W^{IV}$  compound with various acids in attempts to isolate a protonated  $W^{IV}$  compound. Upon titrating pyrrolidinium tetrafluoroborate ( $Pyrr \cdot HBF_4$ ) into a solution of **1a** the UV-visible spectrum exhibited an increase in the absorptions at 311, 470, and 669 nm and a decrease in the absorption at 358 nm with two isosbestic points at 302 and 374 nm suggesting conversion of **1a** to a single product (Figure 1.12A). Attempting to determine a  $pK_a$  of the  $W^{IV}$  compound, after protonation, the deprotonation was attempted with DBU, a strong organic base. Adding 4 equivalents of DBU to the solution showed no change that would indicate deprotonation, and upon adding an excess of DBU (approximately 200 equivalents), the protonation was still irreversible (Figure 1.12B). Similarly, treatment of **1c** with four equivalents of acid, followed by excess base yielded no evidence of deprotonation (Figure 1.13), indicating further reaction to a new product or a major reorganization of the ligand environment upon protonation.

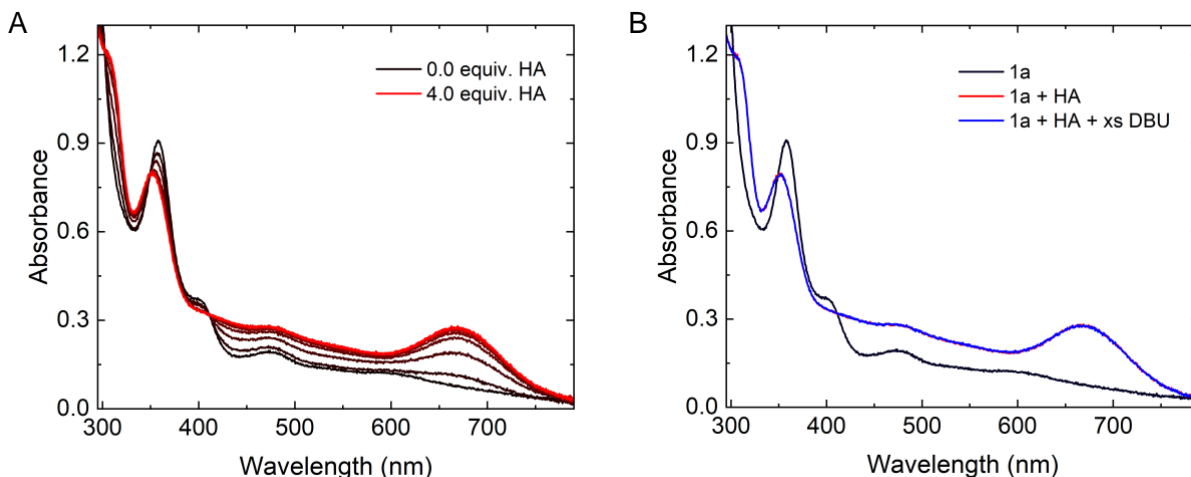


**Figure 1.12:** (A) UV-visible titrations of **1a** with Pyrr•HBF<sub>4</sub> in CH<sub>3</sub>CN and (B) attempted neutralization of acid with DBU

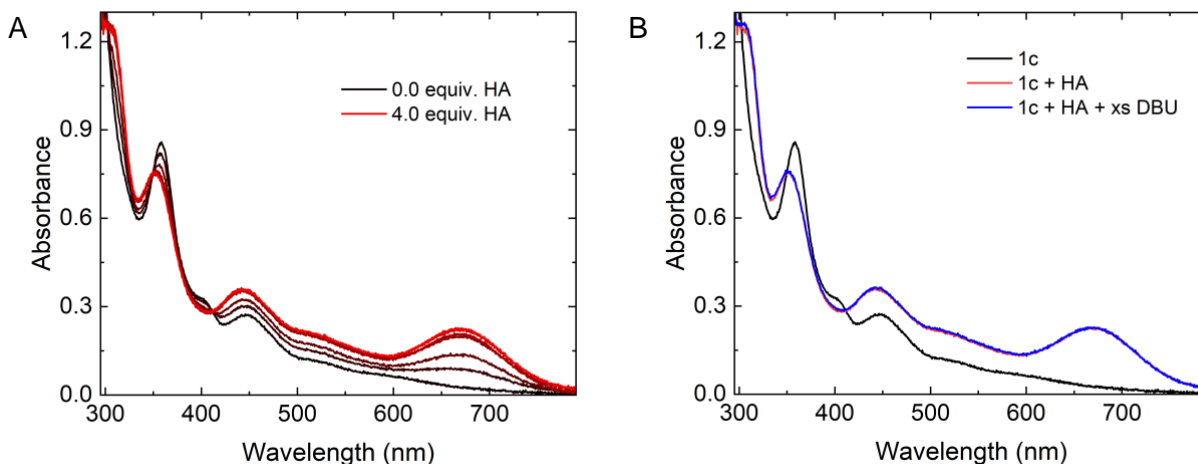


**Figure 1.13:** (A) UV-visible titrations of **1c** with Pyrr•HBF<sub>4</sub> in CH<sub>3</sub>CN. (B) attempted neutralization of acid with DBU

While protonations of **1a** and **1c** lead to single products, as evidenced by isosbestic points at 412 nm and 350 nm in both cases, the new peaks that are formed are similar and follow similar trends with new peaks at 670 nm and 350 nm. There is a difference in the new peaks around 500 nm, where protonation of **1a** with 4 equivalents of Pyrr•HBF<sub>4</sub> (solid black trace, Figure 1.14) produces a new peak at 479 nm with a shoulder at 550 nm while **1c** (dashed black trace, Figure 1.14) produces a new peak at 445 nm with a shoulder at 525 nm. Treatment of **1a** with 5 equivalents of NEt<sub>3</sub>•HBF<sub>4</sub> (blue trace, Figure 1.14) yields a spectrum that is similar to **1a** with

Pyrr•HBF<sub>4</sub>. Using Py•HBF<sub>4</sub> as the proton source for **1a** and **1c**, as with all of the cases, a peak grows in at 570 nm with slight shifts (<5 nm) most of the peaks compared to the Pyrr•HBF<sub>4</sub> samples. One major exception is the growth of the peak at 397 nm, which is not seen in any of the other spectra. With the slight differences among all of the combinations of acid and W compound, we believe that the tungsten-containing products of the reactions are very similar if not identical with the identical peaks at 670 nm and very similar peaks at 351 nm. If not identical products, the differences in the spectra could indicate conjugate base binding to the metal complex.

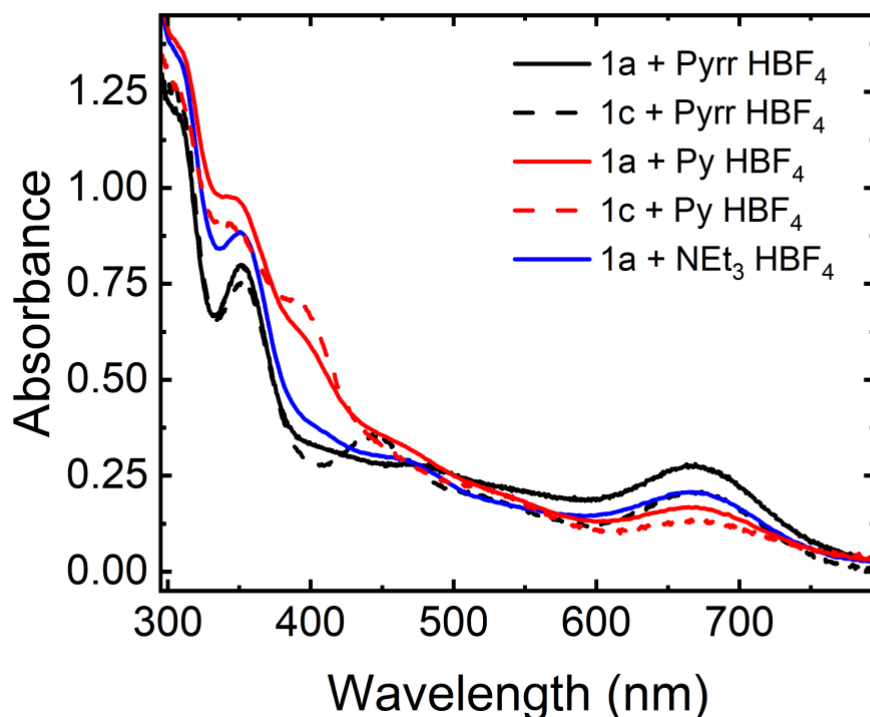


**Figure 1.14:** Comparison of UV-visible titrations of acids into solutions of **1a** and **1c** in CH<sub>3</sub>CN at room temperature. Black traces contain 4 equivalents of Pyrr•HBF<sub>4</sub>, red traces contain 1 equivalent of Py•HBF<sub>4</sub>, and the blue trace contains 5 equivalents of NET<sub>3</sub>•HBF<sub>4</sub>. In solid traces, acids were titrated into solutions of **1a**. In dashed traces, acids were titrated into **1c**.

While we are confident that the treatment of **1a** and **1c** with acids each yield single products based on the UV-visible spectra, the spectrum of the product is not consistent with any known compound. Holm and coworkers showed that decomposition of **1a** and similar compounds occurs to form the Et<sub>4</sub>N<sup>+</sup> salt of **2** under various conditions.<sup>11,17,25</sup> Based on further studies to be



discussed, we detected and isolated **2** from solutions of **1a** or **1c** in the presence of Py•HBF<sub>4</sub>. To investigate this, we treated solutions of **1c** with 1 equivalent of Py•HBF<sub>4</sub> and monitored the reaction over time. At room temperature, shown in Figure 1.15, the red spectrum after reacting for 3 hours is consistent with the spectrum of independently synthesized **2**. Further, with more datapoints in between measurements, the same reaction was performed at 50°C and shown in Figure 1.16. At elevated temperature, the evolution of the reaction is clearly forming **2** over the course of about 2 hours.

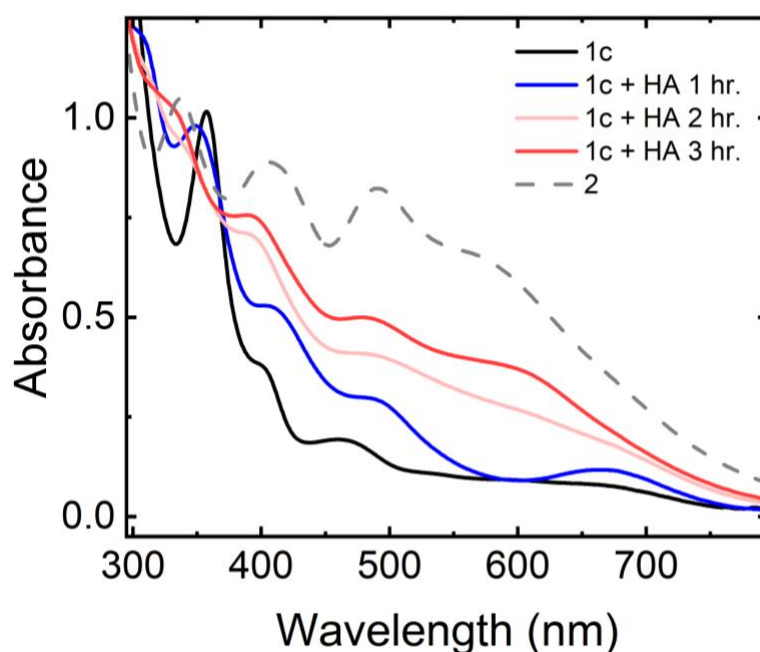


**Figure 1.15:** Time-resolved spectra of the products of the treatment of **1c** with 1 equivalent of Py•HBF<sub>4</sub> in CH<sub>3</sub>CN at room temperature. Black spectrum is of 0.16 mM **1c** in without acid. Blue trace is of **1c** in the presence of 1 equivalent of Py•HBF<sub>4</sub> after 1 hr., salmon trace after 2 hr, and red trace after 3 hr. Gray trace is of independently synthesized **2**.

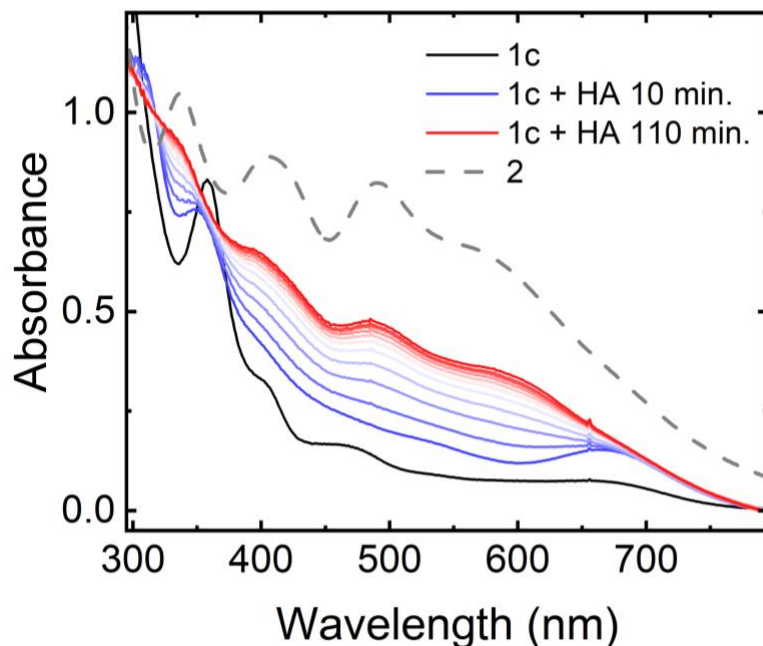


**Figure 1.16:** Time-resolved spectra of the products of the treatment of **1c** with 1 equivalent of  $\text{Py}\cdot\text{HBF}_4$  in  $\text{CH}_3\text{CN}$  at  $50^\circ\text{C}$ . Black spectrum is of  $0.16\text{ mM}$  **1c** in without acid. Blue trace is of **1c** in the presence of  $\text{Py}\cdot\text{HBF}_4$  after 10 minutes. As the reaction proceeds, after the first blue spectrum, further spectra are reported in 30 minute increments, ending in the red spectrum at 270 min. The gray dashed spectrum is of independently synthesized **2**.

Assuming clean conversion from the direct product of protonation to **2**, the concentration of the direct product of protonation (**1cH**) can be estimated as a function of the concentration of **2**, shown in Equation 2 where the initial concentration of **1c** was  $160\ \mu\text{M}$  at  $t = 0$  and assuming full conversion to **1cH** at  $t = 10\text{ min}$  (Equation 3) and full conversion of **1cH** to **2** at  $t=110\text{ min}$ . (Equation 4). Because we assume that the concentration of **1c** is 0 at  $t \geq 10\text{ min}$ , the absorbance of the solution at a given wavelength can be expressed as Equation 5. Taking into account Equations 2, 3, 4, and the fact that absorbance and concentration are proportional for a given compound at a given wavelength, the concentration of **1cH** can be estimated at each time point by the ratio of the change of absorbance at a given time and the total change in absorbance from  $t = 10\text{ min}$  to  $t = 110\text{ min}$  (Equation 6, expanded form in Equation 7).

$$(2) [1cH]_{t \geq 10\text{ min.}} \approx 160\ \mu\text{M} - [2]_{t \geq 10\text{ min.}}$$

$$(3) [1cH]_{t = 10\text{ min.}} \approx 160\ \mu\text{M} = [1c]_{t = 0}$$

$$(4) [2]_{t=110 \text{ min.}} \approx 160 \mu\text{M} = [1c]_{t=0}$$

$$(5) Abs_t \approx Abs_{1cH,t} + Abs_{2,t}$$

$$(6) [1cH]_t \approx 160 \mu\text{M} \times \frac{|\Delta Abs_t|}{|\Delta Abs_{tot}|}$$

$$(7) [1cH]_t \approx 160 \mu\text{M} \times \frac{|Abs_{t=110 \text{ min.}} - Abs_t|}{|Abs_{t=110 \text{ min.}} - Abs_{t=10 \text{ min.}}|}$$

Having estimated the concentration of **1cH** in the reaction mixture over time, we can plot a function of the concentration of **1cH** over time and find that the  $\ln[1cH]$  vs. time plot is linear (Figure 1.17) indicating the transformation of **1cH** to **2** follows a 1<sup>st</sup> order observed rate. This strongly suggests that the collision of two molecules of **1cH** is not a plausible rate-determining step for the overall conversion of **1cH** to **2**, which would likely follow 2<sup>nd</sup> order behavior since **2** is a dimer. Overall, the data here show that the mechanism of the conversion of **1c** to **2** through protonation is complicated and may involve multiple steps not considered here.

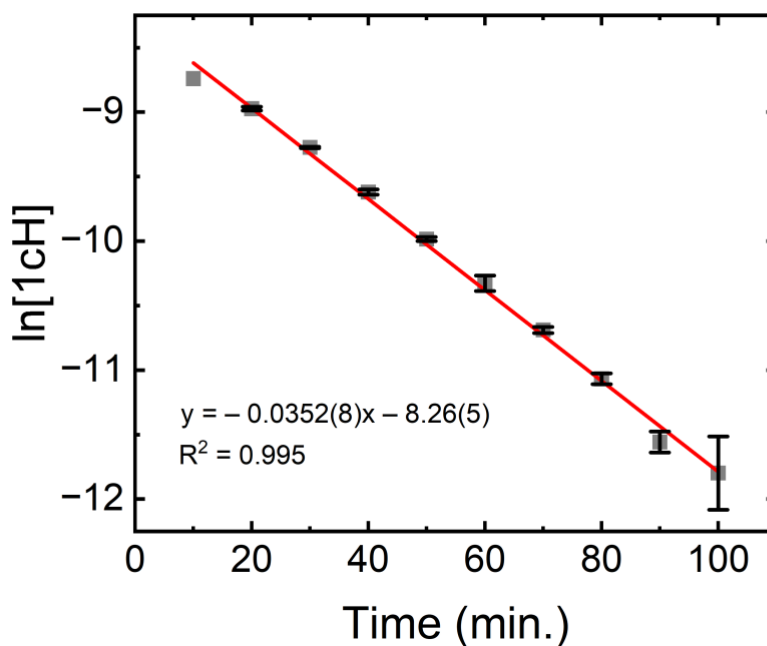
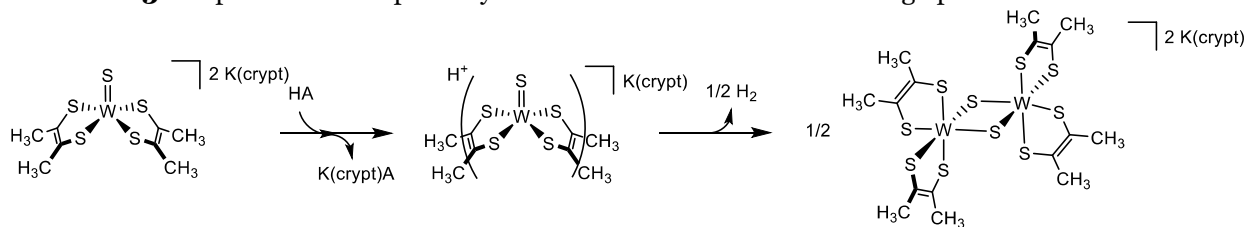


**Figure 1.17:** Plot of  $\ln(1cH)$  vs. time showing a linear relationship.  $[1cH]$  at each time point was calculated by determining the average of the values found at each time point using Equation 7 for  $\lambda = 338, 406, 490,$  and  $570 \text{ nm}$ . Error bars are the propagated errors from the standard deviations of those calculations.

The UV-visible titrations of acids into solutions of **1a** and **1c** have clearly shown that there is clean conversion to **1aH** and **1cH**, respectively. After allowing solutions of **1c** and Py•HBF<sub>4</sub> to react for longer periods of time, the conversion of **1cH** to **2** is also clean especially at elevated temperatures. To characterize the products of the reaction further, a series of <sup>1</sup>H NMR studies were performed with a set of them shown in Figure 1.18 (next page). In each of the experiments, solutions of **1a** were treated with 1 equivalent of Py•HBF<sub>4</sub>. Concerningly, the resulting <sup>1</sup>H NMR spectra for **1aH** are inconsistent with multiple resonances growing in. A consistent feature among the spectra is the appearance of resonances at 4.57 and 2.26 ppm which correspond closely to H<sub>2</sub> and **2**, respectively. In one experiment, when treating **1c** with 1 equivalent of Py•HBF<sub>4</sub>, a black crystalline solid precipitated, and the structure was confirmed to be **2** by single crystal XRD. All subsequent experiments in attempting to isolate **1cH** have resulted in **2**, which were confirmed by unit cell analyses on the black single crystals that formed from the reactions.

From these <sup>1</sup>H NMR studies and the UV-visible titrations, we are confident that rather than the oxidative pathways shown in the generation of **2** and in the previous studies by Holm, the reaction proceeds through a protonation pathway, which ultimately leads to the formation of H<sub>2</sub> and the final product (Scheme 1.3).

**Scheme 1.3:** Proposed reaction pathway for the conversion of **1c** to **2** through protonation



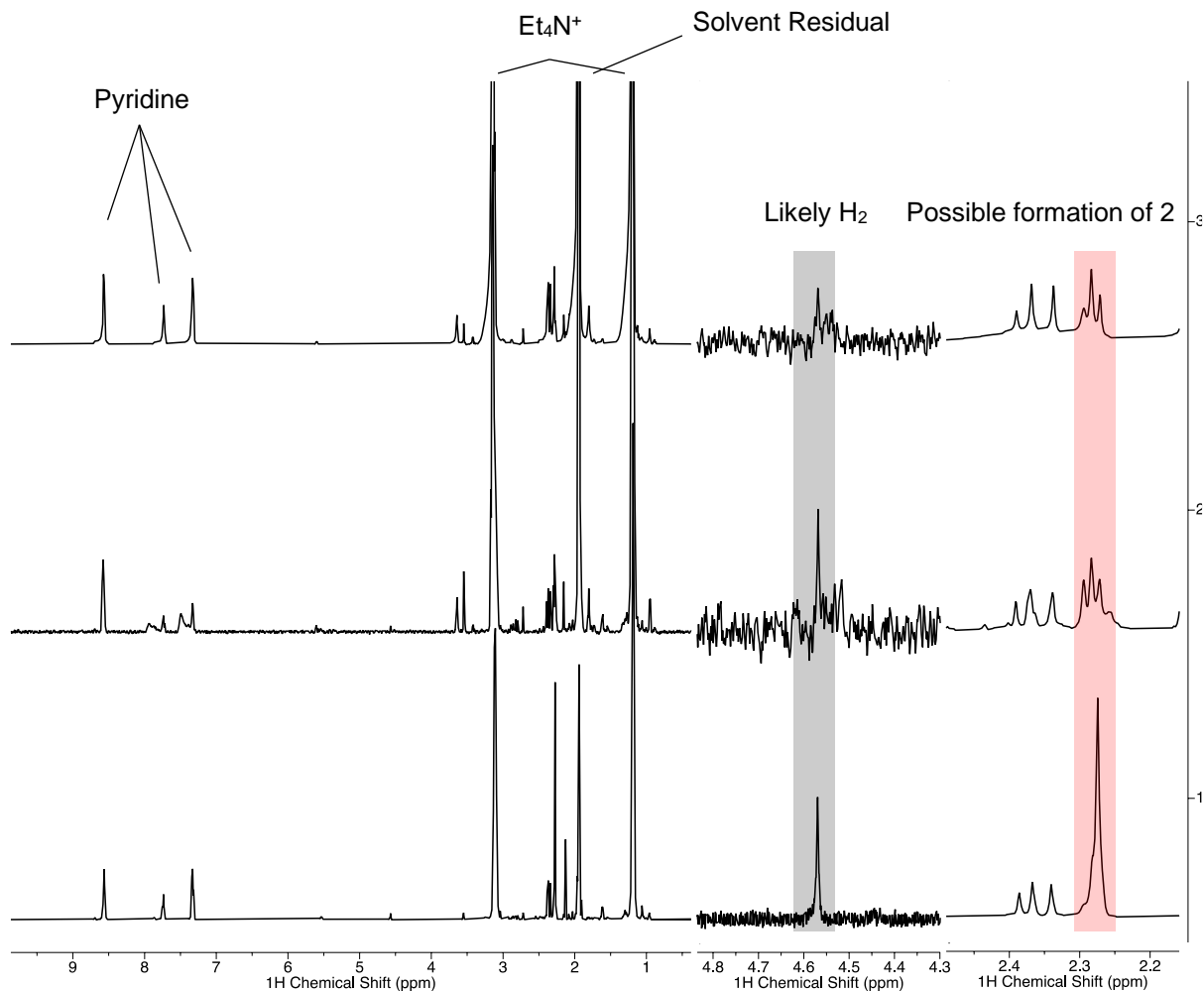


**Figure 1.18:**  $^1\text{H}$  NMR of the protonation of **1a** showing evidence for  $\text{H}_2$  and **2** after protonation by  $\text{Py}\cdot\text{HBF}_4$

### X-ray Absorption Spectroscopy

While the structures of the WIV compounds, **1a-c**, and the dimeric  $\text{W}^{\text{V}}$  compound, **2**, are clear, full characterization of the protonated forms or the immediate product after protonation of the WIV compounds has been elusive. To explore the structure of intermediate **1aH**, X-ray absorption spectroscopy was performed Mackenzie Field at the W  $L_3$  edge (10206.8 eV) on samples containing **1a** and **1a** with 1 equivalent of  $\text{Py}\cdot\text{HBF}_4$ . Samples were prepared by dropping 20 mM solutions of **1a** and freshly prepared **1a** with 1 equivalent of  $\text{Py}\cdot\text{HBF}_4$  (**1aH**) into a frozen sample cup in a liquid nitrogen cooled cold well in an inert atmosphere glove box. The energies were calibrated to the Fe K edge of Fe foil (7111.2 eV). Figure 1.19 shows the energy of the edge for

**1a**, a  $W^{IV}$  complex, was 10213.2(2) eV, and for the protonated complex (**1aH**), the energy was 10214.4(2). This 1.2 eV shift to higher binding energies can be associated with an increase in oxidation state of the metal center.<sup>28</sup> An increase in oxidation state is only expected upon protonation if the species formed formally oxidizes the metal center, which can be the case if the most basic site is at the metal center, forming a  $W^{VI}$  hydride.

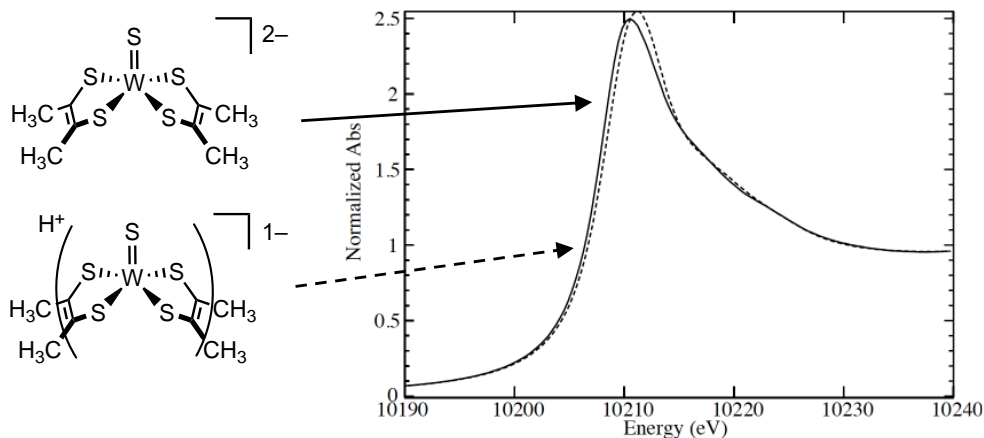


**Figure 1.19:** Comparison of W  $L_3$  edge energies. The solid line represents **1a**, while the dotted line represents protonated **1aH**

## EXAFS

EXAFS fits of the XAS spectra and Fourier transforms for **1a** (Figure 1.20, top) and its protonated form (**1aH**) (Figure 1.20, bottom) were performed by Mackenzie Field. Upon protonation, there was no significant change in the bond lengths between the tungsten center and either of the sulfurs on the bisdithiolene ligands or the terminal sulfido. The lack of significant lengthening in the axial W-S bond is strongly indicative that this sulfur atom is not the site of protonation.

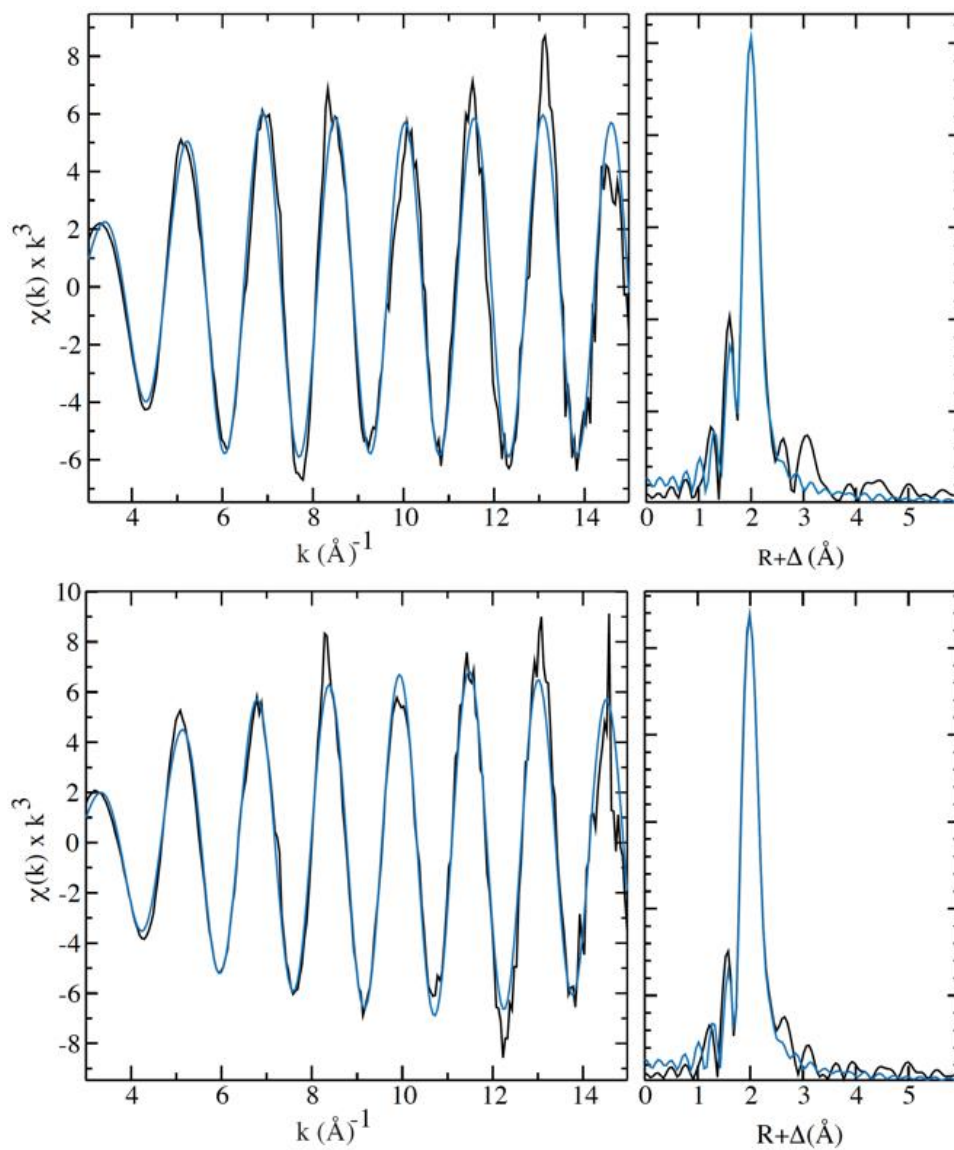


**Figure 1.20:** EXAFS data and Fourier transforms for **1a** (top) and **1aH** (bottom). Raw data is shown in black, and the best fit data is shown in light blue.

**Table 1.4:** EXAFS best fit bond metrics for W-S bonds in **1a** and **1aH**.

Sample	EQUATORIAL W-S			AXIAL W=S			Eo(eV)
	N	R(Å)	$\sigma^2(\text{Å}^2)$	N	R(Å)	$\sigma^2(\text{Å}^2)$	
<b>1a</b>	4	2.36	0.0016	1	2.19	0.0024	-6.4(2)
<b>1aH</b>	4	2.37	0.0016	1	2.18	0.0051	-7.6(2)

After showing previously that the major product of protonation of **1c** is **2**, an alternate fit, **1aH<sub>alt</sub>**, was performed by Field (Table 1.5) showing major differences between the crystallographically characterized **2** and the best fit with a large Debye-Waller factor for the W-W scattering. With these data, we are confident that the EXAFS data for **1aH** are inconsistent with either **1a** or **2**. This may be confirmed with EXAFS analysis of **2**.

**Table 1.5:** EXAFS best fit bond metrics for protonated **1a** modeled as **2**

Sample	Method	W-S			W-W		
		N	R(Å)	$\sigma^2(\text{Å}^2)$	N	R(Å)	$\sigma^2(\text{Å}^2)$
<b>1aH<sub>alt</sub></b>	EXAFS	6	2.39	0.00376	1	3.07	0.01247
<b>2</b>	XRD		2.3863(6)			2.9787(5)	

## Electrochemical Characterization of Protonation Products

Further electrochemical studies were performed to gain insight into the products of protonation of the monomeric tungsten complexes. As Py•HBF<sub>4</sub> was titrated by 1/3 equivalents into a solution of **1a** (Figure 1.21), the W<sup>VI/V</sup> and W<sup>V/IV</sup> couples become less pronounced as a cathodic event grows in at -2.25 V, which corresponds closely to an irreversible cathodic event in the independently synthesized dimer, **2**, shown in Figure 1.22 in blue. Also, there is a possibly quasireversible event centered at -1.1 V that has a current response that is inconsistent with the number of equivalents of Py•HBF<sub>4</sub> added. To explore this further, Figure 1.22 (red) shows a time-dependent study of the protonation of **1c** with Py•HBF<sub>4</sub> where one equivalent of pyridinium tetrafluoroborate was added to a solution of **1c**, and multiple cyclic voltammetry experiments were performed over the course of 7 minutes. A wide cyclic voltammogram of **1c** is shown in black in Figure 1.22 for reference. The loss of the event coupled with the growth of reductions and oxidations that are similar to the dimer suggest the dimer, **2** (shown in blue in Figure 1.22), is a possible decomposition product in the electrochemical cell.



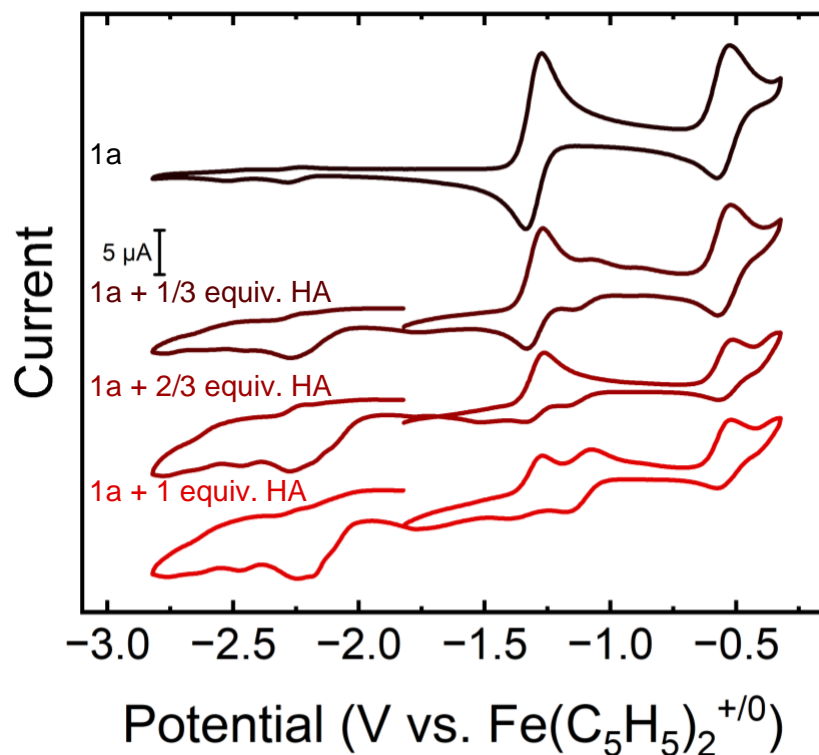


**Figure 1.21:** Cyclic voltammetry studies of the protonation products of 5 mM **1a**. the black trace shows the current response of **1a** without acid, and in each subsequent trace 1/3 equivalent of Py•HBF<sub>4</sub> was added to the analyte solution, totaling 1 equivalent in the red trace.

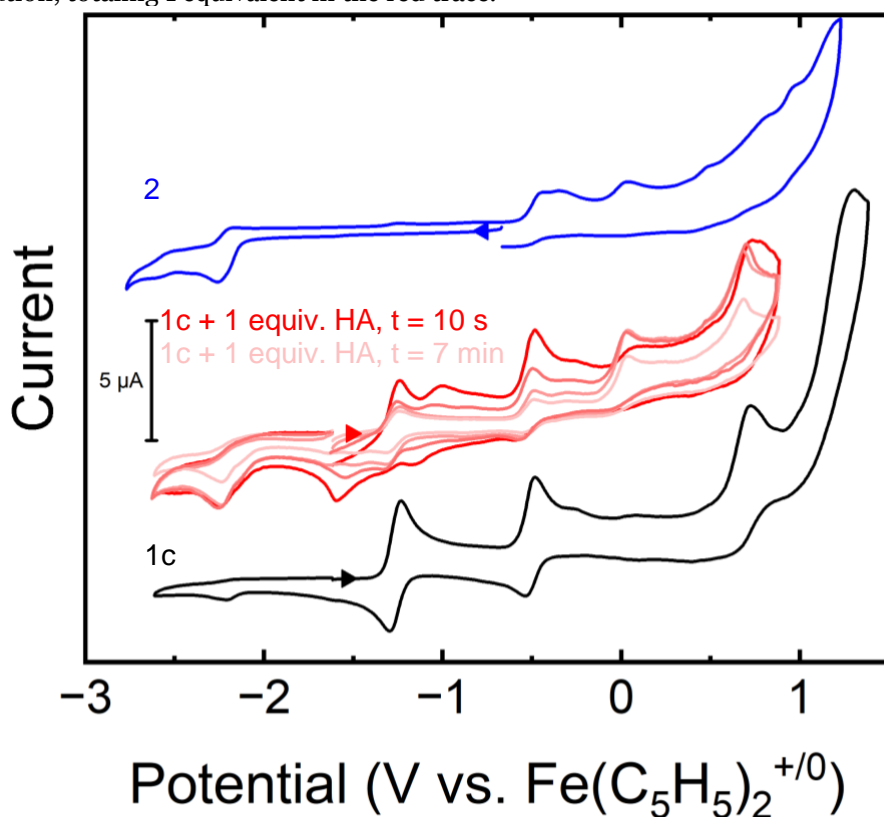


**Figure 1.22:** Cyclic voltammograms of tungsten compounds. Blue: **2**. Black: **1c**. Red: Sequential cyclic voltammograms of **1c** in the presence of 1 equivalent of Py•HBF<sub>4</sub> over the course of 7 min.

## Hydride Transfer Studies of **1aH**

In an attempt to confirm the presence of a hydride, samples of **1a** treated with 1 equivalent of  $\text{Py}\cdot\text{HBF}_4$  were treated with various hydride acceptors according to Scheme **1.4**, and the hydride-reduced products were measured by comparing  $^1\text{H}$ -NMR or  $^{31}\text{P}$ -NMR integrations to an internal standard. The results of the hydride transfer studies are summarized in Table **1.6**. Using  $\text{Ni}(\text{dppe})_2^{2+}$ , a significant amount of  $\text{NiH}(\text{dppe})_2^+$  was formed in the reaction, but the resulting  $^{31}\text{P}$ -NMR showed many resonances corresponding to various decomposition products, none of which were identifiable. In calculating the conversion for this sample, the lower bound was established by integrating the resonance corresponding to the Ni-H against all other resonances in the  $^{31}\text{P}$ -NMR, and the upper bound was set by assuming a 1:1 conversion and dividing the integration of the Ni-H resonance by the sum of the integrations of the resonances of the Ni-H and the  $\text{Ni}^{\text{II}}$  starting material. The  $^{31}\text{P}$ -NMR spectra of  $[\text{HNi}(\text{dppe})_2][\text{BF}_4]$ ,  $[\text{Ni}(\text{dppe})_2][\text{BF}_4]_2$ , and the reaction mixture after 30 minutes and 72 hours are shown in Figure **1.23**. The chemical shifts were referenced to an external standard capillary of 0.1 M triphenylphosphate ( $\text{OP}(\text{OPh})_3$ ) in  $\text{CD}_3\text{CN}$  (17 ppm).<sup>29</sup>

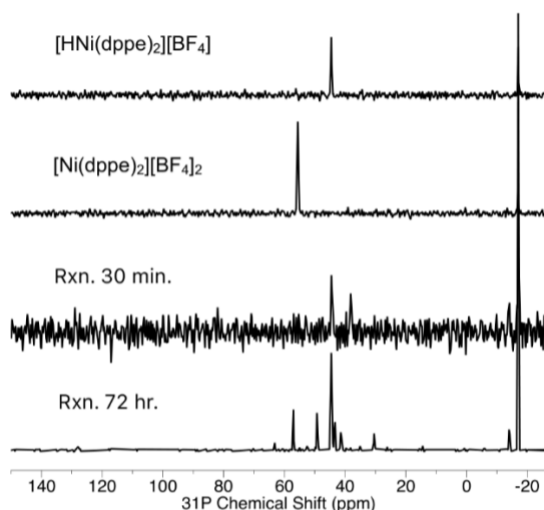


**Figure 1.23:**  $^{31}\text{P}$  NMR study of hydride transfer from **1aH** to  $[\text{Ni}(\text{dppe})_2][\text{BF}_4]_2$ . The first 3 spectra were collected at 162 MHz using a Bruker DRX400, and the last at was collected 243 MHz on a Bruker AVANCE600.

Treating the protonated tungsten compound with  $\text{CCl}_4$ , a common diagnostic hydride acceptor, showed a broad resonance that grew in at 2.32 ppm in the  $^1\text{H-NMR}$  suggesting some reaction with  $\text{CCl}_4$ , but no  $\text{CHCl}_3$  was formed. Finally, using a very strong hydride acceptor, trityl tetrafluoroborate ( $[\text{CPh}_3][\text{BF}_4]$ ), about 36% conversion to triphenylmethane was observed by observing the methyl proton resonance. Interestingly, no resonances belonging to trityl remain shortly after adding it, and the resonances that do remain (the other 64% of the reported conversion) are shifted. The resonance associated with the proton ortho to the methyl carbon shifts downfield by 1 ppm. The shifted resonances are inconsistent with  $\text{Ph}_3\text{SH}$ <sup>30</sup> and the dimerized trityl radical.<sup>31</sup> We propose  $\text{W}^{\text{IV}}(\text{SCPh}_3)(\text{S}_2\text{C}_2(\text{CH}_3)_2)_2^-$  as a possible explanation. Ultimately, these hydride transfer studies showed that although there may be some form of hydride equivalents in solution, the conversion is unpredictable.

**Scheme 1.4:** Attempted hydride transfer studies



**Table 1.6:** Results of hydride transfer studies

Sample	Hydride Acceptor	Hydricity of M-H (kcal/mol)	Conversion to M-H
1	$\text{Ni}(\text{dppe})_2^{2+}$	62.8 <sup>5,32</sup>	30-68%
2	$\text{CCl}_4$	---	0%
3	$\text{CPh}_3^+$	99 <sup>33</sup>	36% <sup>a</sup>

<sup>a</sup>Significant amount of other phenyl-containing product present. Structure proposed to be  $\text{W}^{\text{IV}}(\text{SCPh}_3)(\text{S}_2\text{C}_2(\text{CH}_3)_2)_2^-$ .

## Infrared Studies on Protonated **1a** and Density Functional Analysis

To further characterize the products of protonation, IR studies were performed in hopes of identifying a W-H or S-H stretch as an intermediate to the formation of **2**. Additionally, various protonation states of the tungsten compound were analyzed using DFT analysis. Four possible protonation locations, two sulfur-based protonation sites and two tungsten-based protonation sites, are proposed on the  $W^{IV}$  starting material as shown in Scheme S1. The ground state free energies were calculated in Gaussian16<sup>34</sup> (GaussView<sup>35</sup> GUI) using B3LYP<sup>36</sup> with the LANL2dz<sup>37</sup> effective core potential on the W atom with the D95V<sup>38</sup> basis set, and on all other atoms, 6-311+G(d,p)<sup>39,40</sup> was used. All were calculated using a singlet ground state. Vibrational frequencies were scaled by 0.9619.<sup>41</sup>

The calculated energies for the various protonation locations are summarized in Table **1.7** along with the calculated relevant IR stretch, formal oxidation state on the metal center, and selected bond lengths. Similar to experimental Group 6 M-SH compounds,<sup>42,43</sup> the calculated stretching frequencies were  $2540\text{ cm}^{-1}$  and  $2543\text{ cm}^{-1}$  for the sulfido SH (A) and dithiolene SH (B), respectively. The calculated stretching frequencies for the equatorial hydride (C) and the axial hydride (D) vary greatly from each other. Published W-H IR stretching frequencies tend to depend on oxidation state where a lower oxidation state gives a lower stretching frequency. Published experimental W-H stretching frequencies (including the highest energy W-H stretches for compounds with multiple stretching modes) are usually  $1875 \pm 75\text{ cm}^{-1}$ .<sup>44-48</sup> The calculated W-H stretching frequency for C agrees well with both calculated and experimental literature values while D, which optimized to a much higher energy ground state, falls outside of the expected region.

**Table 1.7:** Tabulated selected metrics for the DFT geometry-optimized structures of protonated  $W(S)[S_2C_2(CH_3)_2]_2^{2-}$

Protonation State				
	A	B	C	D
Calculated free energy relative to A (kcal/mol)	---	6.01	-1.75	27.23
$\nu_{\text{calc}}$ MH or SH ( $\text{cm}^{-1}$ )	2540	2543	1909	1631
W formal oxidation state	+4	+4	+6	+6
W- $S_{\text{eq}}$ average (standard deviation)	2.357(2)	2.41(6)	2.454(8)	2.42001(2)
W- $S_{\text{ax}}$	2.37103	2.17518	2.16160	2.23907

ATR-IR spectra were collected on drop cast samples of **1a** freshly mixed with 1 equiv. of  $\text{Py}\cdot\text{HBF}_4$  (Figure 1.24) and **1a** with  $\text{Py}\cdot\text{DOTf}$  (Figure 1.25). In the sample treated with the protonated acid, a peak appears at  $1937\text{ cm}^{-1}$ , which agrees with both literature precedent for tungsten hydrides and the DFT calculated IR stretches for C ( $1909\text{ cm}^{-1}$ ). As expected for a W-H formed from protonation, when treated with the deuterated acid, a peak that would correspond to a W-H stretch was not present. The DFT-calculated W-D stretch was  $1395\text{ cm}^{-1}$ , which agrees very well with the harmonic oscillator approximation for the experimental data ( $1392\text{ cm}^{-1}$ ). An IR stretching frequency near  $1390\text{ cm}^{-1}$  falls very close to some of the lower energy stretching frequencies for the tetraethylammonium ion, so identifying a W-D stretching mode was unsuccessful. For both experiments, the simulated transmission spectra (red or blue) are shown overlaid with the experimental spectra (black).

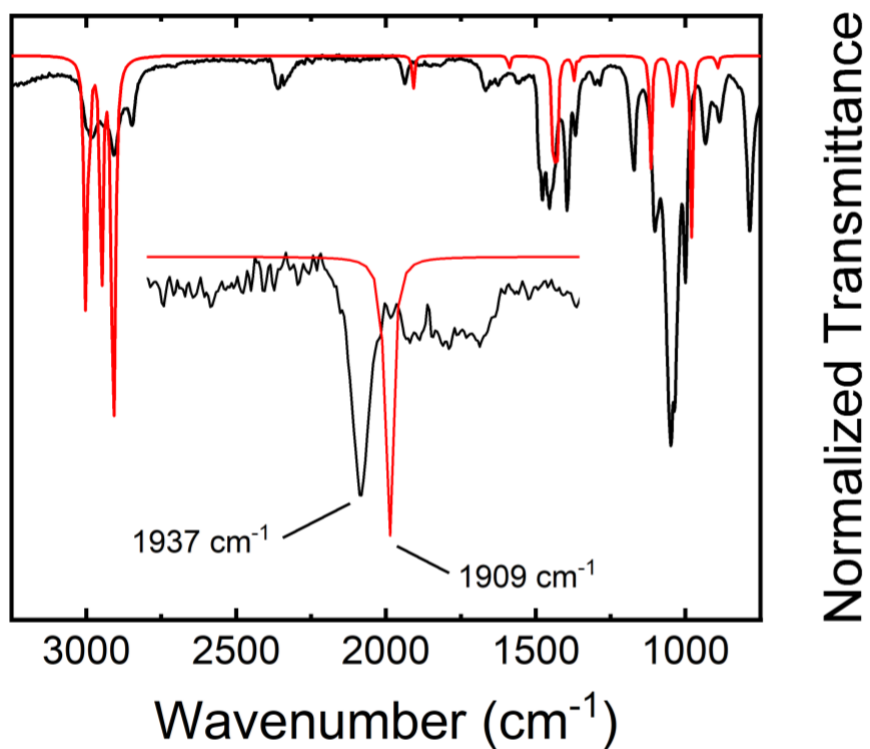


**Figure 1.24:** Infrared spectrum of **1a** treated with 1 equivalent of Py·HBF<sub>4</sub> (black) and DFT-simulated spectrum (red)

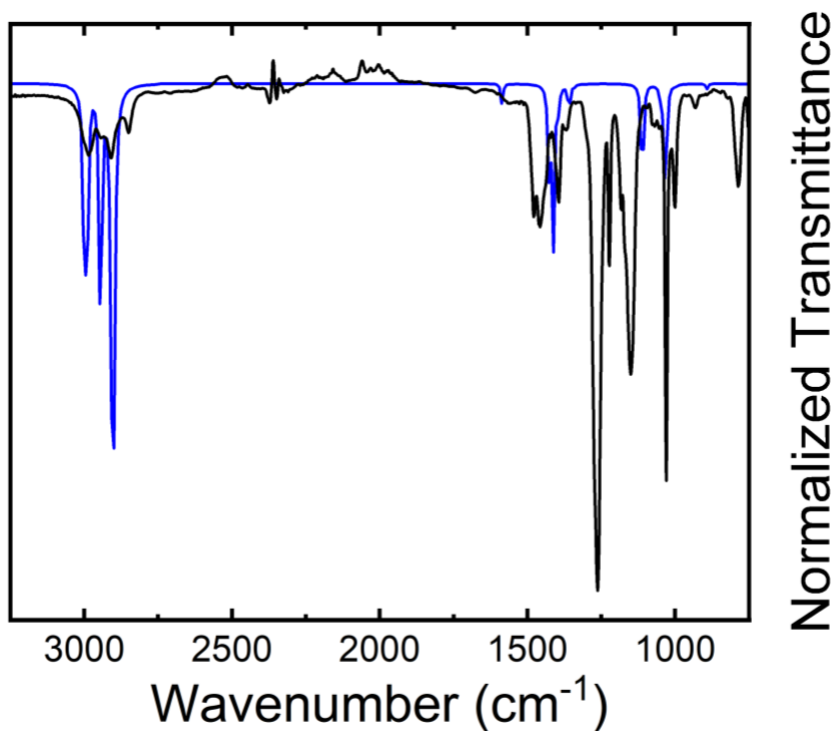


**Figure 1.25:** Infrared Spectrum of **1a** treated with 1 equivalent of Py·DOTf (black) and the DFT-simulated spectrum (blue)

The optimized geometry for structure C showed a pseudo-pentagonal prismatic coordination environment with near perfect  $C_{2v}$  symmetry and is shown in Figure 1.26. The calculated  $S_{ax}$ -W-H angle was  $88.45^\circ$ , and the  $S_{ax}$ -W- $S_{eq}$  angles were  $110.24^\circ$  and  $103.88^\circ$  for the sulfur atoms closest to the hydride and furthest from the hydride, respectively, which indicates a slight downward cant of the closer sulfur atoms from a plane perpendicular to the W- $S_{ax}$  bond. Two crystallographically characterized examples of tungsten hydrides have previously been reported that show unconventional hydrides similar to the one calculated in protonation state C. The compound with CSD access code BENFEG<sup>49</sup> shows a pentagonal bipyramidal ligand environment with two bisdimethylphosphinoethane (dmpe) ligands in the equatorial plane with the hydride and a borylalkylidyne ligand trans to a chloride. NUCTAG<sup>50</sup> is a formally  $W^{IV}$  compound in a pseudo- $C_{3v}$  tripodal ligand environment with a highly dissociated formyl group, leading to a hydride that points out of the equatorial plane with an axial CO ligand.

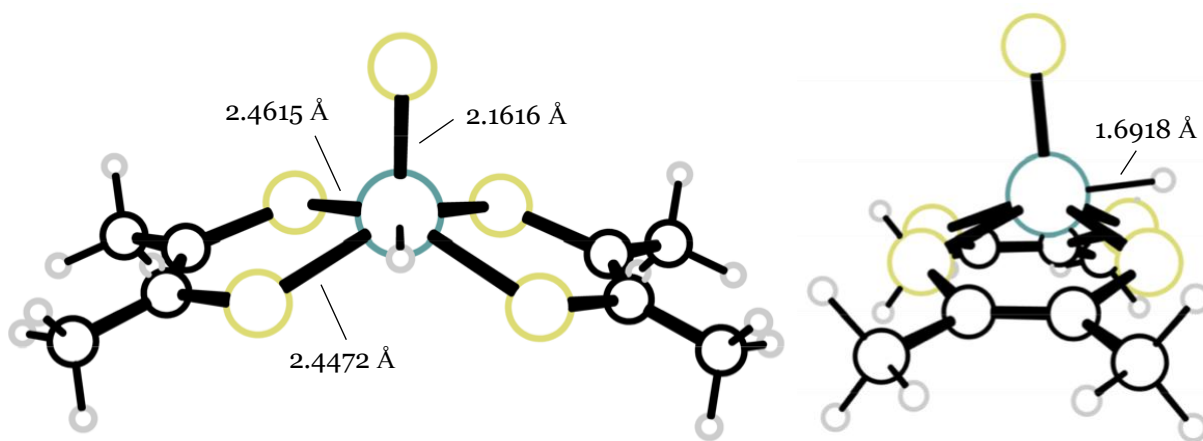


**Figure 1.26:** DFT optimized structure of protonation state C from two angles with selected bond lengths

The average equivalent W-S bond lengths are also shown in Table 1.7 in order to compare with EXAFS data, which is unable to distinguish among identical scatterers with very similar bond lengths. Table 1.8 shows a comparison of experimentally determined bond lengths for **1a** and **1aH** with the calculated bond metrics for the  $W^{IV}$  anion,  $W(S)[S_2C_2(CH_3)_2]_2^{2-}$  and calculated structure C, the equatorial  $W^{VI}$  hydride. The single crystal X-ray diffraction studies agree very well with the

EXAFS data for the parent  $W^{IV}$  compound while the DFT optimized structure tends to overestimate the W-S bond lengths by about 0.045 Å for the equatorial sulfur atoms and about 0.025 Å for the axial sulfur atom. Comparing the EXAFS-determined bond lengths to the DFT-optimized structures, there is no perfect match, but considering overall trends, the W-S bond lengths showed only minor changes of bond lengths in the protonated form. The equatorial W-S bonds show a very slight lengthening while the axial W-S bond shows a very slight shortening in the EXAFS fit. The DFT-calculated bond length changes were generally larger in magnitude than the changes seen in the EXAFS fit. A showed a major lengthening of the axial W-S bond consistent with the formation of a sulfhydryl group from a sulfido and a shortening of the W- $S_{eq}$  bonds. B had a very large variation of W- $S_{eq}$  bond lengths, ranging from 2.38 to 2.50 Å and a shortening of the W- $S_{ax}$  bond by 0.05 Å. Both tungsten hydrides modeled showed an increase in the W- $S_{eq}$  bonds, but while D showed a lengthening of the W- $S_{ax}$  bond, C showed a shortening. Although the DFT-calculated bond length changes are significantly greater than the changes shown in the EXAFS fit, the only one that follows the general trend is C.

**Table 1.8:** Selected bond lengths found using single crystal XRD (for **1b** and **1c**), EXAFS (for **1a** and **1aH**), and computational methods for deprotonated and protonated  $W(S)[S_2C_2(CH_3)_2]_2^{2-}$

	<b>Deprotonated</b>				<b>Protonated</b>	
	<b>1b</b>	<b>1c</b>	EXAFS <sup>a</sup>	DFT	EXAFS <sup>b</sup>	DFT (C)
W- $S_{eq}$	2.356(3) <sup>c</sup>	2.354(3) <sup>c</sup>	2.36	2.40051	2.37	2.454(8)
W- $S_{ax}$	2.1881(6)	2.1818(4)	2.19	2.21020	2.18	2.16160

<sup>a</sup>**1a** dissolved in acetonitrile and flash frozen in liquid nitrogen

<sup>b</sup>**1a** dissolved in acetonitrile, treated with one equivalent of Py•HBF<sub>4</sub> and promptly flash frozen in liquid nitrogen

<sup>c</sup>average (standard deviation)

Although similar basis sets and methods have been used before in literature,<sup>51–54</sup> we sought to validate the relative calculated energies and bond lengths presented here. Two basis sets with a lower level of theory were used for geometry optimization and frequency calculations, 6-31+G(d,p) and D95V. Additionally, the B3P86 functional was used with the D95V basis set. All calculations were performed using the LANL2dz effective core potential. The free energies relative



to A using different methods are compared in Figure 1.27. The same general trend for the difference in free energy among the 4 protonation states holds fairly well among all methods. The equatorial tungsten hydride, C, is the lowest in energy in every case. Using the D95V basis set, the equatorial hydride was much lower in energy by 7.3 kcal/mol compared to only 0.9 kcal/mol for the 6-31+g(d,p) basis set.

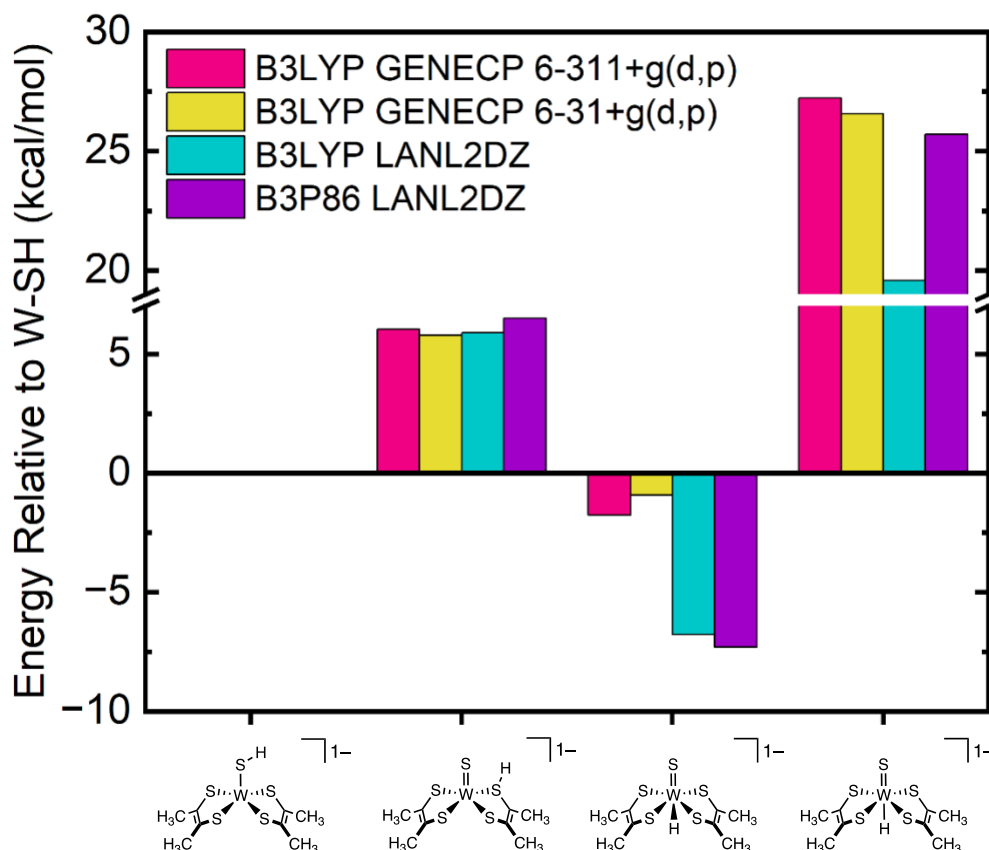
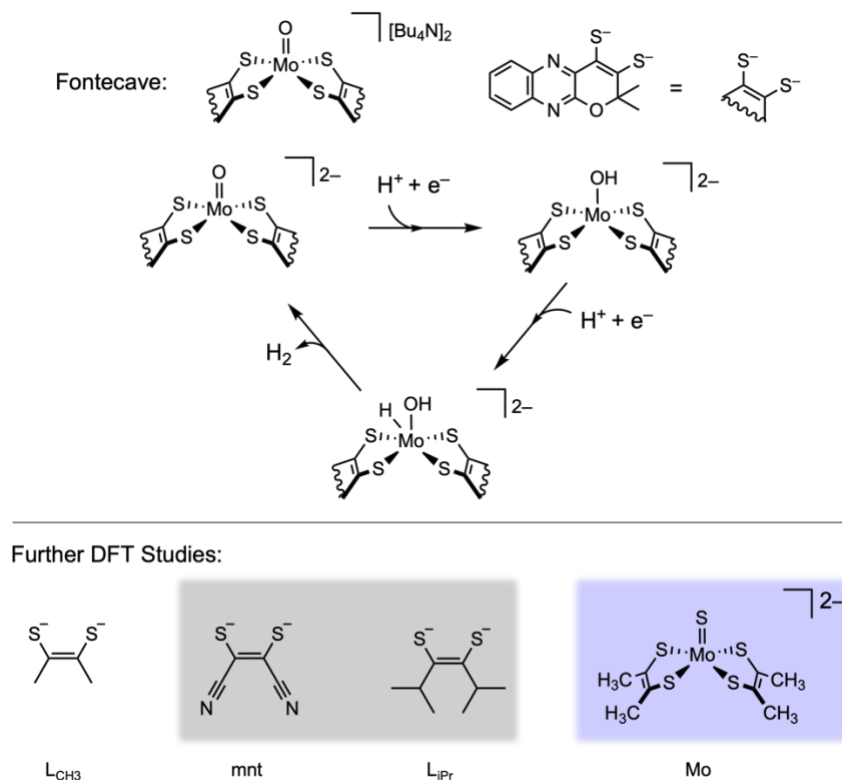


**Figure 1.27:** Plot of relative energies of the various protonation states of  $WS(S_2C_2(CH_3)_2)H$  using various basis sets and an alternate method. B3LYP GENECP experiments were performed with the LANL2dz basis set and core potential on the tungsten center with the other specified basis set on all other atoms.

In all of the basis sets and the two methods tried, the energy for the equatorial tungsten hydride was always lowest in energy in the likely oversimplified ligand set that we chose to model the FDH system. Presumptively, Fontecave and coworkers were unable to perform  $CO_2$  reduction with their  $Mo^{IV}$  oxo system that has a more complicated bisdithiolene set that more closely models

the molybdopterin cofactor (Scheme 1.5). However, they were able to show both electrochemical and photochemical H<sub>2</sub> evolution that, through DFT studies, was proposed to go through a protonation of the oxo as the first step, but also subsequent metal reduction and protonation of the metal, forming a Mo(OH)H compound.<sup>55,56</sup> To study the contribution of the ligand and the metal to the location of first protonation, preliminary studies were performed in the same fashion as before with the dimethyldithiolene ligand (L<sub>CH<sub>3</sub></sub>) replaced with a dicyanodithiolene (mnt) or a diisopropylidithiolene (L<sub>iPr</sub>), and in another set of calculations, W was replaced with Mo.

**Scheme 1.5:** Published work by Fontecave and coworkers and alternate ligand sets for DFT studies



Geometry optimization and energy calculations were performed using B3LYP, LANL2DZ core potential and basis set on the metal, and 6-311+G(d,p) on all other atoms as before on three variations of the W bisdithiolene compound. The DFT-calculated relative energies for the three selected protonation states is shown in Figure 1.28. The axial hydride that was modeled in previous experiments was excluded because of its significantly higher energy in all other cases. In

comparison with the  $L_{CH_3}$  compound, using the  $L_{iPr}$  ligand showed essentially no change in the relative energies of the protonation states. Methyl groups and isopropyl groups have very similar hammet parameters,<sup>57</sup> so intramolecular sterics probably have no effect on the protonation site.

When the *mnt* ligand, containing cyano groups, is modeled (orange, Figure **1.28**), the relative energies change significantly. Being moderately electron-withdrawing, the cyano group pulls electron density from the rest of the ligand, yielding a less basic metal thiolate by 3.9 kcal/mol compared to  $L_{CH_3}$  (yellow, Figure **1.28**). This electron-withdrawing effect extends to the W center where the calculated energy difference between the two hydrides is 6.0 kcal/mol, yielding a W-H optimized structure that is 4.3 kcal/mol higher in energy than the W-SH, meaning that the terminal sulfido has become the most basic site. Further, when the W is replaced with Mo (blue, Figure **1.28**), the energy of the hydride is 12.0 kcal/mol higher than the W-SH. Similar Mo compounds have been synthesized,<sup>58</sup> but we expect the Mo analogue to be even less stable to protonation than the W compound. While the **1a** and **1c** exhibited reversible electrochemical processes for both the  $W^{VI/V}$  and the  $W^{IV/V}$  redox couples, the similar molybdenum compounds only show reversibility of the  $Mo^{IV/V}$  redox couple at scan rates  $> 300$  mV/s.<sup>58</sup>

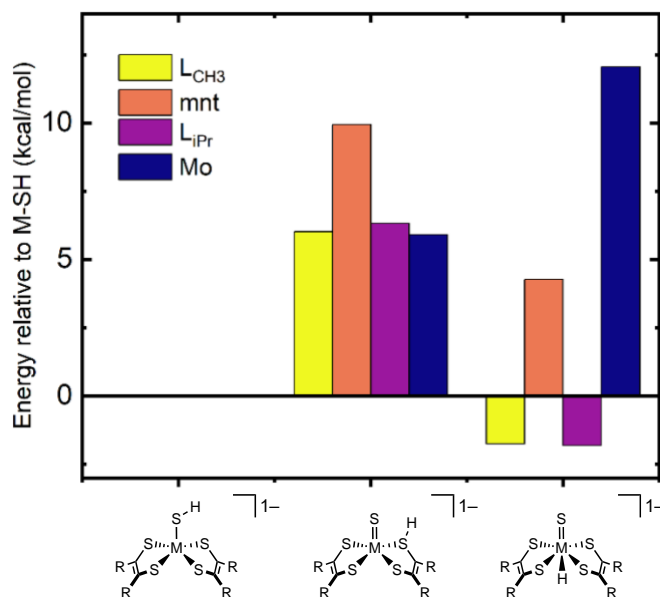
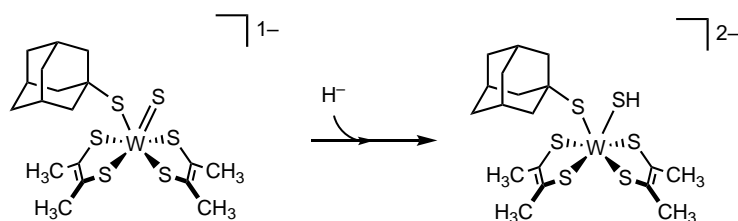


**Figure 1.28:** Relative DFT-calculated energies of various compounds similar to **1a**

## Six-Coordinate FDH Analogues

In the 5-coordinate tungsten studies, the guiding principle was to investigate the interconversion of a synthetic analogue of both the oxidized and formate-reduced FDH enzyme active site. The  $W^{IV}$  compound studied was in the proper oxidation state but deprotonated in comparison to the formate-reduced active site. Additionally, while it bears some structural resemblance to the enzyme active site, it is missing a thiolate or selenolate ligand that would be structurally similar to the cysteinate or selenocysteinate ligand. To investigate the consequences of this 6<sup>th</sup> ligand, some preliminary studies were performed on the 6-coordinate  $W^{VI}$  compound,  $[Et_4N]W(S)(SAd)[S_2C_2(CH_3)_2]_2$  in an attempt to generate an analogue of the FDH active site formate-reduced and protonated form (Scheme 1.6). Previous work by Holm and coworkers<sup>59</sup> showed that this reaction product was relatively unstable and consistently decomposed to the previously discussed  $W^V$ - $W^V$  dimer during attempts to grow diffraction quality crystals. Nonetheless, hydride transfer reactions were attempted with  $Bu_4NHCO_2$ ,  $Et_4NBH_4$ , and  $LiBHET_3$ .

**Scheme 1.6:** Potential structure of hydride-reduced 6-coordinate tungsten compound



The  $W^{VI}$  compound (Sample 1, Figure 1.29) displays only three resonances in the  $^1H$  NMR spectrum, two broad resonances corresponding to the adamantyl protons, and a sharp resonance at 2.28 ppm (red box, , Figure 1.29) corresponding to the methyl protons on the dithiolene ligand; other resonances in the spectrum at 3.11 and 1.18 ppm belong to the  $Et_4N^+$  counteranion. Decomposition was monitored over 11 days (Sample 2, Figure 1.29). Significant decomposition can be seen in the  $^1H$ -NMR spectrum with multiple resonances appearing over the course of monitoring, including one resonance at 2.26 ppm (blue highlight, Figure 1.29), ascribed to the aforementioned  $W^V$ - $W^V$  dimer (**2**). Surprisingly, when any of the hydride donors are added, the

only new resonance in the 2.1-2.5 ppm region is the one corresponding to the dimer. The fate of the adamantyl thiolate group is unknown in the cases with reductants, we speculate that by reducing each tungsten by one electron, the thiolate dimerizes as well (Scheme 1.7)

**Table 1.9:** NMR studies of 6-coordinate  $W^{VI}$  compounds

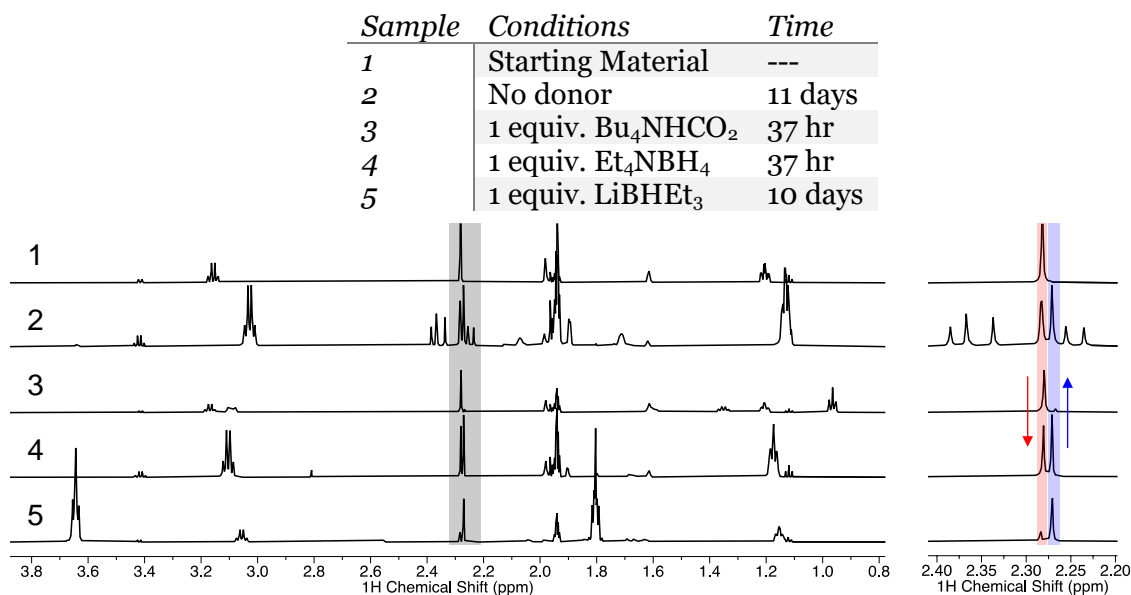
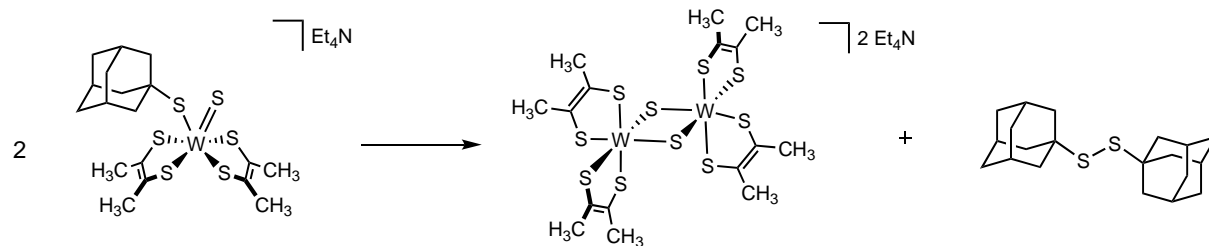


**Figure 1.29:**  $^1H$ -NMR spectra of the reaction of  $[Et_4N]W(S)(SAd)[S_2C_2(CH_3)_2]_2$  with hydride donors in  $CD_3CN$

**Scheme 1.7:** Proposed reaction pathway for the decomposition of  $[Et_4N]W(S)(SAd)[S_2C_2(CH_3)_2]_2$



## Conclusions and Outlook

The protonation of the  $W^{IV}$  monomeric salt,  $[K(\text{crypt})]_2W(S)[S_2C_2(CH_3)_2]_2$ , yields a dimeric formally  $W^V$ - $W^V$  species. Crystallographically, it is very similar to the published structure which contains a  $Et_4N^+$  countercation. By mass balance, an equivalent of  $H_2$  is formed. DFT studies, IR analysis, and EXAFS suggest the direct product of protonation is a  $W^{VI}$  hydride. Without clean

conversion via NMR-scale protonation studies or other structural information, showing first order reaction kinetics and inconclusive hydride transfer studies, we note that the direct product of protonation may be a mixture of products or one not considered here. In the studies of the 6-coordinate tungsten compound, the  $W^V$ - $W^V$  dimer once again was the major product of the reaction, showing definitively that the dimeric compound is a thermodynamic sink that is difficult to overcome in studying the reactivity of these compounds.

The possibility of finding a system that forms a stable  $W^{IV}$ -SH is nonetheless existent. DFT calculations suggest that electron-withdrawing groups may be able to stabilize the protonated product of the reaction, however, dimerization will likely continue to be an issue. Future experiments on this work could involve extending to the more stable group 6 metal oxos, which should be less susceptible to dimerization.

## *Crystallographic Information*

### **Crystallographic Information for 1b**

The data for jyy186 were collected from a shock-cooled single crystal at 88(2) K on a Bruker SMART APEX II three-circle diffractometer with a sealed X-ray tube using a equatorial mounted graphite as monochromator and a Bruker Apex II CCD detector. The diffractometer was equipped with a low temperature device and used  $\text{MoK}_\alpha$  radiation ( $\lambda = 0.71073 \text{ \AA}$ ). All data were integrated with SAINT and a multi-scan absorption correction using SADABS was applied.<sup>60,61</sup> The structure was solved by direct methods using SHELXS and refined by full-matrix least-squares methods against  $F^2$  by SHELXL-2018/3 using ShelXle.<sup>62,63</sup> All non-hydrogen atoms were refined with anisotropic displacement parameters. All C-bound hydrogen atoms were refined isotropic on calculated positions using a riding model with their  $U_{\text{iso}}$  values constrained to 1.5 times the  $U_{\text{eq}}$  of their pivot atoms for terminal  $\text{sp}^3$  carbon atoms and 1.2 times for all other carbon atoms. Disordered moieties were refined using bond lengths restraints and displacement parameter restraints. This report and the CIF file were generated using FinalCif.<sup>64</sup>

### **Refinement Details:**

All non-hydrogen atoms were refined anisotropically. Most were refined without restraints or constraints. Part of the crown ethers was disordered with an approximate ratio of 85:15. ADPs for O11, C12, and C13 were restrained to similar values to O11b, C12b, and C13b. All hydrogen atoms were refined using a riding model with disorder refined on the methyl groups on the dithiolene ligand.

## Crystallographic Information for 1c

The data for jyy187 were collected from a shock-cooled single crystal at 133(2)K on a Bruker SMART APEX II three-circle diffractometer with a fine-focus sealed tube using a equatorial mounted graphite as monochromator and a Bruker Apex II CCD detector. The diffractometer was equipped with a low temperature device and used  $\text{MoK}\alpha$  radiation ( $\lambda = 0.71073 \text{ \AA}$ ). All data were integrated with SAINT and a multi-scan absorption correction using SADABS was applied.<sup>60,61</sup> The structure was solved by direct methods using SHELXS and refined by full-matrix least-squares methods against  $F^2$  by SHELXL-2018/3 using ShelXle.<sup>62,63</sup> All non-hydrogen atoms were refined with anisotropic displacement parameters. The hydrogen atoms were refined isotropically on calculated positions using a riding model with their  $U_{\text{iso}}$  values constrained to 1.5 times the  $U_{\text{eq}}$  of their pivot atoms for terminal  $\text{sp}^3$  carbon atoms and 1.2 times for all other carbon atoms. This report and the CIF file were generated using FinalCif.<sup>64</sup>

### Refinement Details:

All non-hydrogen atoms were refined anisotropically. All hydrogen atoms were refined using a riding model.



## Crystallographic Information for 2

The data for jyy191 were collected from a shock-cooled single crystal at 133(2) K on a Bruker SMART APEX II three-circle diffractometer with a fine-focus sealed tube using a equatorial mounted graphite as monochromator and a Bruker Apex II CCD detector. The diffractometer was equipped with a low temperature device and used  $\text{MoK}\alpha$  radiation ( $\lambda = 0.71073 \text{ \AA}$ ). All data were integrated with SAINT and a multi-scan absorption correction using SADABS was applied.<sup>60,61</sup> The structure was solved by direct methods using SHELXS and refined by full-matrix least-squares methods against  $F^2$  by SHELXL-2018/3 using ShelXle.<sup>62,63</sup> All non-hydrogen atoms were refined with anisotropic displacement parameters. All C-bound hydrogen atoms were refined isotropic on calculated positions using a riding model with their  $U_{\text{iso}}$  values constrained to 1.5 times the  $U_{\text{eq}}$  of their pivot atoms for terminal  $\text{sp}^3$  carbon atoms and 1.2 times for all other carbon atoms. This report and the CIF file were generated using FinalCif.<sup>64</sup>

### Refinement Details:

All non-hydrogen atoms were refined anisotropically with no constraints or restraints. All hydrogen atoms were refined using a riding model. SQUEEZE,<sup>65</sup> implemented in Platon,<sup>66,67</sup> was used to remove what appeared to be a heavily disordered partial occupancy acetonitrile molecule.

**Table 1.10:** Crystallographic data for 1b, 1c, and 2

	<b>1b</b>	<b>1c</b>	<b>2</b>
<i>Empirical formula</i>	C <sub>32</sub> H <sub>60</sub> Na <sub>2</sub> O <sub>12</sub> S <sub>5</sub> W	C <sub>50</sub> H <sub>93</sub> K <sub>2</sub> N <sub>7</sub> O <sub>12</sub> S <sub>5</sub> W	C <sub>52</sub> H <sub>96</sub> K <sub>2</sub> N <sub>4</sub> O <sub>12</sub> S <sub>10</sub> W <sub>2</sub>
<i>Formula weight</i>	1026.93	1406.66	1735.82
<i>Temperature [K]</i>	88(2)	133(2)	133(2)
<i>Crystal system</i>	monoclinic	monoclinic	triclinic
<i>Space group (number)</i>	<i>P</i> 2 <sub>1</sub> / <i>n</i> (14)	<i>P</i> 2 <sub>1</sub> / <i>n</i> (14)	<i>P</i> $\bar{1}$ (2)
<i>a [Å]</i>	12.0912(5)	13.7869(8)	12.2383(11)
<i>b [Å]</i>	15.3159(6)	23.2461(13)	13.1315(12)
<i>c [Å]</i>	22.6502(9)	20.2756(12)	13.3719(12)
<i>α [°]</i>	90	90	117.2007(13)
<i>β [°]</i>	94.1743(6)	96.5522(9)	93.0683(15)
<i>γ [°]</i>	90	90	99.6978(14)
<i>Volume [Å<sup>3</sup>]</i>	4183.4(3)	6455.7(6)	1863.0(3)
<i>Z</i>	4	4	1
<i>ρ<sub>calc</sub> [gcm<sup>-3</sup>]</i>	1.630	1.447	1.547
<i>μ [mm<sup>-1</sup>]</i>	3.087	2.139	3.529
<i>F(000)</i>	2096	2920	878
<i>Crystal size [mm<sup>3</sup>]</i>	0.242×0.229×0.124	0.414×0.249×0.208	0.300×0.257×0.215
<i>Crystal color</i>	brown	brown	purple
<i>Crystal shape</i>	prism	prism	irregular
<i>Radiation</i>	MoK <sub>α</sub> (λ=0.71073 Å)	MoK <sub>α</sub> (λ=0.71073 Å)	MoK <sub>α</sub> (λ=0.71073 Å)
<i>2θ range [°]</i>	3.21 to 63.01 (0.68 Å)	2.68 to 61.59 (0.69 Å)	3.41 to 61.05 (0.70 Å)
<i>Index ranges</i>	-17 ≤ h ≤ 17 -22 ≤ k ≤ 22 -31 ≤ l ≤ 32	-19 ≤ h ≤ 19 -33 ≤ k ≤ 33 -29 ≤ l ≤ 29	-17 ≤ h ≤ 17 -18 ≤ k ≤ 18 -19 ≤ l ≤ 19
<i>Reflections collected</i>	66114	99430	45889
<i>Independent reflections</i>	13122 R <sub>int</sub> = 0.0281 R <sub>sigma</sub> = 0.0238	19467 R <sub>int</sub> = 0.0362 R <sub>sigma</sub> = 0.0262	10927 R <sub>int</sub> = 0.0572 R <sub>sigma</sub> = 0.0433
<i>Completeness to θ = 25.242°</i>	100.0 %	100.0 %	100.0 %
<i>Data / Restraints / Parameters</i>	13122/18/514	19467/0/701	10927/0/376
<i>Goodness-of-fit on F<sup>2</sup></i>	1.044	1.029	1.065
<i>Final R indexes [I ≥ 2σ(I)]</i>	R <sub>1</sub> = 0.0201 wR <sub>2</sub> = 0.0390	R <sub>1</sub> = 0.0203 wR <sub>2</sub> = 0.0474	R <sub>1</sub> = 0.0228 wR <sub>2</sub> = 0.0549
<i>Final R indexes [all data]</i>	R <sub>1</sub> = 0.0243 wR <sub>2</sub> = 0.0403	R <sub>1</sub> = 0.0247 wR <sub>2</sub> = 0.0490	R <sub>1</sub> = 0.0248 wR <sub>2</sub> = 0.0558
<i>Largest peak/hole [eÅ<sup>-3</sup>]</i>	0.89/-1.24	0.95/-0.33	0.83/-0.93

## References

- (1) Laurency, G.; Fellay, C.; Dyson, P. Hydrogen Production from Formic Acid. US20100068131A1, March 18, 2010. <https://patents.google.com/patent/US20100068131A1/en?q=Laurency%2c+C>. (accessed 2019-10-14).
- (2) Fellay, C.; Dyson, P. J.; Laurency, G. A Viable Hydrogen-Storage System Based On Selective Formic Acid Decomposition with a Ruthenium Catalyst. *Angewandte Chemie International Edition* **2008**, *47* (21), 3966–3968. <https://doi.org/10.1002/anie.200800320>.
- (3) Álvarez, A.; Bansode, A.; Urakawa, A.; Bavykina, A. V.; Wezendonk, T. A.; Makkee, M.; Gascon, J.; Kapteijn, F. Challenges in the Greener Production of Formates/Formic Acid, Methanol, and DME by Heterogeneously Catalyzed CO<sub>2</sub> Hydrogenation Processes. *Chem. Rev.* **2017**, *117* (14), 9804–9838. <https://doi.org/10.1021/acs.chemrev.6b00816>.
- (4) An, L.; Chen, R. Direct Formate Fuel Cells: A Review. *Journal of Power Sources* **2016**, *320*, 127–139. <https://doi.org/10.1016/j.jpowsour.2016.04.082>.
- (5) Wiedner, E. S.; Chambers, M. B.; Pitman, C. L.; Bullock, R. M.; Miller, A. J. M.; Appel, A. M. Thermodynamic Hydricity of Transition Metal Hydrides. *Chem. Rev.* **2016**, *116* (15), 8655–8692. <https://doi.org/10.1021/acs.chemrev.6b00168>.
- (6) Niks, D.; Hille, R. Molybdenum- and Tungsten-Containing Formate Dehydrogenases and Formylmethanofuran Dehydrogenases: Structure, Mechanism, and Cofactor Insertion. *Protein Science* **2019**, *28* (1), 111–122. <https://doi.org/10.1002/pro.3498>.
- (7) Schilter, D.; Camara, J. M.; Huynh, M. T.; Hammes-Schiffer, S.; Rauchfuss, T. B. Hydrogenase Enzymes and Their Synthetic Models: The Role of Metal Hydrides. *Chem. Rev.* **2016**, *116* (15), 8693–8749. <https://doi.org/10.1021/acs.chemrev.6b00180>.

- (8) Popov, V. O.; Lamzin, V. S. NAD<sup>+</sup>-Dependent Formate Dehydrogenase. *Biochemical Journal* **1994**, *301* (3), 625–643. <https://doi.org/10.1042/bj3010625>.
- (9) Bassegoda, A.; Madden, C.; Wakerley, D. W.; Reisner, E.; Hirst, J. Reversible Interconversion of CO<sub>2</sub> and Formate by a Molybdenum-Containing Formate Dehydrogenase. *J. Am. Chem. Soc.* **2014**, *136* (44), 15473–15476. <https://doi.org/10.1021/ja508647u>.
- (10) Maia, L. B.; Fonseca, L.; Moura, I.; Moura, J. J. G. Reduction of Carbon Dioxide by a Molybdenum-Containing Formate Dehydrogenase: A Kinetic and Mechanistic Study. *J. Am. Chem. Soc.* **2016**, *138* (28), 8834–8846. <https://doi.org/10.1021/jacs.6b03941>.
- (11) Goddard, C. A.; Holm, R. H. Synthesis and Reactivity Aspects of the Bis(Dithiolene) Chalcogenide Series [WIVQ(S<sub>2</sub>C<sub>2</sub>R<sub>2</sub>)<sub>2</sub>]<sub>2</sub><sup>-</sup> (Q = O, S, Se). *Inorg. Chem.* **1999**, *38* (23), 5389–5398. <https://doi.org/10.1021/ic9903329>.
- (12) Lim, B. S.; Donahue, J. P.; Holm, R. H. Synthesis and Structures of Bis(Dithiolene)Molybdenum Complexes Related to the Active Sites of the DMSO Reductase Enzyme Family. *Inorg. Chem.* **2000**, *39* (2), 263–273. <https://doi.org/10.1021/ic9908672>.
- (13) Sung, K.-M.; Holm, R. H. Substitution and Oxidation Reactions of Bis(Dithiolene)Tungsten Complexes of Potential Relevance to Enzyme Sites. *Inorg. Chem.* **2001**, *40* (18), 4518–4525. <https://doi.org/10.1021/ic010421x>.
- (14) Lim, B. S.; Holm, R. H. Bis(Dithiolene)Molybdenum Analogues Relevant to the DMSO Reductase Enzyme Family: Synthesis, Structures, and Oxygen Atom Transfer Reactions and Kinetics. *J. Am. Chem. Soc.* **2001**, *123* (9), 1920–1930. <https://doi.org/10.1021/ja003546u>.

- (15) Enemark, J. H.; Cooney, J. J. A.; Wang, J.-J.; Holm, R. H. Synthetic Analogues and Reaction Systems Relevant to the Molybdenum and Tungsten Oxotransferases. *Chem. Rev.* **2004**, *104* (2), 1175–1200. <https://doi.org/10.1021/cr020609d>.
- (16) Jiang, J.; Holm, R. H. An Expanded Set of Functional Groups in Bis(Dithiolene)Tungsten(IV,VI) Complexes Related to the Active Sites of Tungstoenzymes, Including WIV–SR and WVI–O(SR). *Inorg. Chem.* **2004**, *43* (4), 1302–1310. <https://doi.org/10.1021/ic030301k>.
- (17) Groysman, S.; Wang, J.-J.; Tagore, R.; Lee, S. C.; Holm, R. H. A Biomimetic Approach to Oxidized Sites in the Xanthine Oxidoreductase Family: Synthesis and Stereochemistry of Tungsten(VI) Analogue Complexes. *J. Am. Chem. Soc.* **2008**, *130* (38), 12794–12807. <https://doi.org/10.1021/ja804000k>.
- (18) Seo, J.; Shearer, J.; Williard, P. G.; Kim, E. Reactivity of a Biomimetic W(IV) Bis-Dithiolene Complex with CO<sub>2</sub> Leading to Formate Production and Structural Rearrangement. *Dalton Trans.* **2019**, *48* (47), 17441–17444. <https://doi.org/10.1039/C9DT03906F>.
- (19) Yang, J. Y.; Kerr, T. A.; Wang, X. S.; Barlow, J. M. Reducing CO<sub>2</sub> to HCO<sub>2</sub><sup>–</sup> at Mild Potentials: Lessons from Formate Dehydrogenase. *J. Am. Chem. Soc.* **2020**, *142* (46), 19438–19445. <https://doi.org/10.1021/jacs.0c07965>.
- (20) Barlow, J. M.; Yang, J. Y. Thermodynamic Considerations for Optimizing Selective CO<sub>2</sub> Reduction by Molecular Catalysts. *ACS Cent. Sci.* **2019**, *5* (4), 580–588. <https://doi.org/10.1021/acscentsci.9b00095>.
- (21) Cunningham, D. W.; Barlow, J. M.; Velazquez, R. S.; Yang, J. Y. Reversible and Selective CO<sub>2</sub> to HCO<sub>2</sub><sup>–</sup> Electrocatalysis near the Thermodynamic Potential. *Angewandte Chemie*

- International Edition* **2020**, *59* (11), 4443–4447.  
<https://doi.org/10.1002/anie.201913198>.
- (22) Schrauzer, G. N.; Mayweg, V. P. Preparation, Reactions, and Structure of Bis(dithio- $\alpha$ -diketone) Complexes of Nickel, Palladium, and Platinum<sup>1,2</sup>. *J. Am. Chem. Soc.* **1965**, *87* (7), 1483–1489. <https://doi.org/10.1021/ja01085a014>.
- (23) Lau, N.; Zakharov, L. N.; Pluth, M. D. Modular Tripodal Receptors for the Hydrosulfide (HS<sup>-</sup>) Anion. *Chem. Commun.* **2018**, *54* (19), 2337–2340. <https://doi.org/10.1039/C7CC09405A>.
- (24) Tate, D. P.; Knipple, W. R.; Augl, J. M. Nitrile Derivatives of Chromium Group Metal Carbonyls. *Inorg. Chem.* **1962**, *1* (2), 433–434. <https://doi.org/10.1021/ic50002a052>.
- (25) Sung, K.-M.; Holm, R. H. Substitution and Oxidation Reactions of Bis(dithiolene)Tungsten Complexes of Potential Relevance to Enzyme Sites. *Inorg. Chem.* **2001**, *40* (18), 4518–4525. <https://doi.org/10.1021/ic010421x>.
- (26) Tshepelevitsh, S.; Kütt, A.; Lõkov, M.; Kaljurand, I.; Saame, J.; Heering, A.; Plieger, P. G.; Vianello, R.; Leito, I. On the Basicity of Organic Bases in Different Media. *European Journal of Organic Chemistry* **2019**, *2019* (40), 6735–6748. <https://doi.org/10.1002/ejoc.201900956>.
- (27) Zanello, P. *Inorganic Electrochemistry*; 2003. <https://doi.org/10.1039/9781847551146>.
- (28) Kubin, M.; Guo, M.; Kroll, T.; Löchel, H.; Källman, E.; L. Baker, M.; Mitzner, R.; Gul, S.; Kern, J.; Föhlisch, A.; Erko, A.; Bergmann, U.; Yachandra, V.; Yano, J.; Lundberg, M.; Wernet, P. Probing the Oxidation State of Transition Metal Complexes: A Case Study on How Charge and Spin Densities Determine Mn L-Edge X-Ray Absorption Energies. *Chemical Science* **2018**, *9* (33), 6813–6829. <https://doi.org/10.1039/C8SC00550H>.

- (29) Ghosh, G.; Greer, A. A Fluorinated Phosphite Traps Alkoxy Radicals Photogenerated at the Air/Solid Interface of a Nanoparticle. *Journal of Physical Organic Chemistry* **2020**, *33* (12), e4115. <https://doi.org/10.1002/poc.4115>.
- (30) Yamamoto, N.; Sato, Y.; Kayaki, Y.; Ikariya, T. Synthesis and Reactivity of Cp\*IrIII Complexes with a C–S Chelate Displaying Metal/Sulfur Bifunctionality. *Organometallics* **2018**, *37* (19), 3342–3352. <https://doi.org/10.1021/acs.organomet.8b00562>.
- (31) Chen, Y.; Li, J.; Jiang, W.; Zhao, J.; Zhu, H.; Muhammed, S.; Parameswaran, P.; Roesky, H. W. A C2-Linked Bis-Silene Formed without Using Metals and the Transformation into the Bis-Silyl and Bis-Silylium C4-Cumulenes. *Organometallics* **2020**, *39* (23), 4282–4286. <https://doi.org/10.1021/acs.organomet.0c00368>.
- (32) Berning, D. E.; Noll, B. C.; DuBois, D. L. Relative Hydride, Proton, and Hydrogen Atom Transfer Abilities of [HM(Diphosphine)<sub>2</sub>]PF<sub>6</sub> Complexes (M = Pt, Ni). *J. Am. Chem. Soc.* **1999**, *121* (49), 11432–11447. <https://doi.org/10.1021/ja991888y>.
- (33) Ilic, S.; Alherz, A.; Musgrave, C. B.; Glusac, K. D. Thermodynamic and Kinetic Hydricities of Metal-Free Hydrides. *Chem. Soc. Rev.* **2018**, *47* (8), 2809–2836. <https://doi.org/10.1039/C7CS00171A>.
- (34) Frisch, M. J.; Trucks, G. W.; Schlegel, H. B.; Scuseria, G. E.; Robb, M. A.; Cheeseman, J. R.; Scalmani, G.; Barone, V.; Petersson, G. A.; Nakatsuji, H.; Li, X.; Caricato, M.; Marenich, A. V.; Bloino, J.; Janesko, B. G.; Gomperts, R.; Mennucci, B.; Hratchian, H. P.; Ortiz, J. V.; Izmaylov, A. F.; Sonnenberg, J. L.; Williams-Young, D.; Ding, F.; Lipparini, F.; Egidi, F.; Goings, J.; Peng, B.; Petrone, A.; Henderson, T.; Ranasinghe, D.; Zakrzewski, V. G.; Gao, J.; Rega, N.; Zheng, G.; Liang, W.; Hada, M.; Ehara, M.; Toyota, K.; Fukuda, R.; Hasegawa, J.; Ishida, M.; Nakajima, T.; Honda, Y.; Kitao, O.; Nakai, H.; Vreven, T.; Throssell, K.; Montgomery, J. A., Jr.; Peralta, J. E.; Ogliaro, F.; Bearpark, M. J.; Heyd, J.

- J.; Brothers, E. N.; Kudin, K. N.; Staroverov, V. N.; Keith, T. A.; Kobayashi, R.; Normand, J.; Raghavachari, K.; Rendell, A. P.; Burant, J. C.; Iyengar, S. S.; Tomasi, J.; Cossi, M.; Millam, J. M.; Klene, M.; Adamo, C.; Cammi, R.; Ochterski, J. W.; Martin, R. L.; Morokuma, K.; Farkas, O.; Foresman, J. B.; Fox, D. J. Gaussian~16 Revision C.01, 2016.
- (35) Dennington, R.; Keith, T. A.; Millam, J. M. GaussView Version 6, 2019.
- (36) Lee, C.; Yang, W.; Parr, R. G. Development of the Colle-Salvetti Correlation-Energy Formula into a Functional of the Electron Density. *Phys. Rev. B* **1988**, *37* (2), 785–789. <https://doi.org/10.1103/PhysRevB.37.785>.
- (37) Hay, P. J.; Wadt, W. R. Ab Initio Effective Core Potentials for Molecular Calculations. Potentials for the Transition Metal Atoms Sc to Hg. *J. Chem. Phys.* **1985**, *82* (1), 270–283. <https://doi.org/10.1063/1.448799>.
- (38) Dunning, Thom. H.; Hay, P. J. Gaussian Basis Sets for Molecular Calculations. In *Methods of Electronic Structure Theory*; Schaefer, H. F., Ed.; Modern Theoretical Chemistry; Springer US: Boston, MA, 1977; pp 1–27. [https://doi.org/10.1007/978-1-4757-0887-5\\_1](https://doi.org/10.1007/978-1-4757-0887-5_1).
- (39) McLean, A. D.; Chandler, G. S. Contracted Gaussian Basis Sets for Molecular Calculations. I. Second Row Atoms, Z=11–18. *J. Chem. Phys.* **1980**, *72* (10), 5639–5648. <https://doi.org/10.1063/1.438980>.
- (40) Krishnan, R.; Binkley, J. S.; Seeger, R.; Pople, J. A. Self-consistent Molecular Orbital Methods. XX. A Basis Set for Correlated Wave Functions. *J. Chem. Phys.* **1980**, *72* (1), 650–654. <https://doi.org/10.1063/1.438955>.
- (41) Andersson, M. P.; Uvdal, P. New Scale Factors for Harmonic Vibrational Frequencies Using the B3LYP Density Functional Method with the Triple- $\zeta$  Basis Set 6-311+G(d,p). *J. Phys. Chem. A* **2005**, *109* (12), 2937–2941. <https://doi.org/10.1021/jp045733a>.



- (42) Iwasa, K.; Seino, H.; Mizobe, Y. Syntheses of New Mo(II) and W(II) Mono(Hydrosulfido) Complexes and Their Conversion into Di- and Tetranuclear Sulfido-Bridged Heterobimetallic Complexes. *Journal of Organometallic Chemistry* **2009**, *694* (23), 3775–3780. <https://doi.org/10.1016/j.jorganchem.2009.07.032>.
- (43) Smith, S. J.; Whaley, C. M.; Rauchfuss, T. B.; Wilson, S. R.  $MS_2(Me_2PC_2H_4PMe_2)_2$  (M = Mo, W): Acid–Base Properties, Proton Transfer, and Reversible Protonolysis of Sulfido Ligands. *Inorg. Chem.* **2006**, *45* (2), 679–687. <https://doi.org/10.1021/ic051443c>.
- (44) Cho, H.-G.; Andrews, L.; Marsden, C. Infrared Spectra of  $CH_3-CrH$ ,  $CH_3-WH$ ,  $CH_2WH_2$ , and  $CH:WH_3$  Formed by Activation of  $CH_4$  with Cr and W Atoms. *Inorg. Chem.* **2005**, *44* (21), 7634–7643. <https://doi.org/10.1021/ic051090h>.
- (45) H. Green, M. L.; Parkin, G.; Mingqin, C.; Prout, K. Trimethylphosphine–Tungsten Chemistry: Hydrido, Silyl, Fluoro, Hydroxy, and Aquo Derivatives: Crystal Structure of  $[W(PMe_3)_4H_2(OH)_2F]F$ . *Journal of the Chemical Society, Chemical Communications* **1984**, *0* (21), 1400–1402. <https://doi.org/10.1039/C39840001400>.
- (46) Wang, X.; Andrews, L.; Infante, I.; Gagliardi, L. Infrared Spectra of the  $WH_4(H_2)_4$  Complex in Solid Hydrogen. *J. Am. Chem. Soc.* **2008**, *130* (6), 1972–1978. <https://doi.org/10.1021/ja077322o>.
- (47) Kaesz, H. D.; Saillant, R. B. Hydride Complexes of the Transition Metals. *Chem. Rev.* **1972**, *72* (3), 231–281. <https://doi.org/10.1021/cr60277a003>.
- (48) Martin, J. T. Organometallic Nitrosyl Hydrides of Tungsten, University of British Columbia, Vancouver, 1987. <https://open.library.ubc.ca/media/stream/pdf/831/1.0060388/1>.
- (49) van der Eide, E. F.; Piers, W. E.; Romero, P. E.; Parvez, M.; McDonald, R. Reaction of Bis(Pentafluorophenyl)Borane with Methylidyne Complexes: Synthesis and

- Characterization of a Cationic Tungsten(VI) Borylalkylidyne Hydride. *Organometallics* **2004**, *23* (3), 314–316. <https://doi.org/10.1021/om034318m>.
- (50) Dobbs, D. A.; Schrock, R. R.; Davis, W. M. Reactions of [(Me<sub>3</sub>SiNCH<sub>2</sub>CH<sub>2</sub>)<sub>3</sub>N]WH with Dihydrogen, Olefins, Acetylenes, Carbon Monoxide, n-Butylisocyanide and Azobenzene. *Inorganica Chimica Acta* **1997**, *263* (1), 171–180. [https://doi.org/10.1016/S0020-1693\(97\)05647-8](https://doi.org/10.1016/S0020-1693(97)05647-8).
- (51) Ryde, U.; Schulzke, C.; Starke, K. Which Functional Groups of the Molybdopterin Ligand Should Be Considered When Modeling the Active Sites of the Molybdenum and Tungsten Cofactors? A Density Functional Theory Study. *J Biol Inorg Chem* **2009**, *14* (7), 1053–1064. <https://doi.org/10.1007/s00775-009-0548-y>.
- (52) Hofmann, M. Density Functional Theory Studies of Model Complexes for Molybdenum-Dependent Nitrate Reductase Active Sites. *J Biol Inorg Chem* **2007**, *12* (7), 989–1001. <https://doi.org/10.1007/s00775-007-0271-5>.
- (53) Fritscher, J.; Hrobárik, P.; Kaupp, M. Computational Studies of EPR Parameters for Paramagnetic Molybdenum Complexes. II. Larger MoV Systems Relevant to Molybdenum Enzymes. *Inorg. Chem.* **2007**, *46* (20), 8146–8161. <https://doi.org/10.1021/ic070341e>.
- (54) Leopoldini, M.; Russo, N.; Toscano, M.; Dulak, M.; Wesolowski, T. A. Mechanism of Nitrate Reduction by *Desulfovibrio Desulfuricans* Nitrate Reductase—A Theoretical Investigation. *Chemistry – A European Journal* **2006**, *12* (9), 2532–2541. <https://doi.org/10.1002/chem.200500790>.
- (55) Porcher, J.-P.; Fogeron, T.; Gomez-Mingot, M.; Derat, E.; Chamoreau, L.-M.; Li, Y.; Fontecave, M. A Bioinspired Molybdenum Complex as a Catalyst for the Photo- and Electroreduction of Protons. *Angew. Chem. Int. Ed.* **2015**, *54* (47), 14090–14093. <https://doi.org/10.1002/anie.201505607>.

- (56) Porcher, J.-P.; Fogeron, T.; Gomez-Mingot, M.; Chamoreau, L.-M.; Li, Y.; Fontecave, M. Synthesis and Reactivity of a Bio-Inspired Dithiolene Ligand and Its Mo Oxo Complex. *Chem. Eur. J.* **2016**, *22* (13), 4447–4453. <https://doi.org/10.1002/chem.201504373>.
- (57) Hansch, C.; Leo, A.; Taft, R. W. A Survey of Hammett Substituent Constants and Resonance and Field Parameters. *Chemical Reviews* **1991**, *91* (2), 165–195. <https://doi.org/10.1021/cr00002a004>.
- (58) Sugimoto, H.; Tano, H.; Suyama, K.; Kobayashi, T.; Miyake, H.; Itoh, S.; Mtei, R. P.; Kirk, M. L. Chalcogenidobis(Ene-1,2-Dithiolate)Molybdenum(IV) Complexes (Chalcogenide E = O, S, Se): Probing MoE and Ene-1,2-Dithiolate Substituent Effects on Geometric and Electronic Structure. *Dalton Trans.* **2011**, *40* (5), 1119–1131. <https://doi.org/10.1039/CoDT00871K>.
- (59) Groysman, S.; Holm, R. H. Synthesis and Structures of Bis(Dithiolene)Tungsten(IV,VI) Thiolate and Selenolate Complexes: Approaches to the Active Sites of Molybdenum and Tungsten Formate Dehydrogenases. *Inorg. Chem.* **2007**, *46* (10), 4090–4102. <https://doi.org/10.1021/ic062441a>.
- (60) Bruker. SAINT.
- (61) Krause, L.; Herbst-Irmer, R.; Sheldrick, G. M.; Stalke, D. Comparison of Silver and Molybdenum Microfocus X-Ray Sources for Single-Crystal Structure Determination. *J Appl Cryst* **2015**, *48* (1), 3–10. <https://doi.org/10.1107/S1600576714022985>.
- (62) Sheldrick, G. A Short History of SHELX. *Acta Crystallographica Section A* **2008**, *64* (1), 112–122. <https://doi.org/doi:10.1107/S0108767307043930>.
- (63) Sheldrick, G. M. Crystal Structure Refinement with SHELXL. *Acta Cryst C* **2015**, *71* (1), 3–8. <https://doi.org/10.1107/S2053229614024218>.

- (64) Kratzert, D. FinalCif. [HTTPS://dkratzert.de/finalcif.html](https://dkratzert.de/finalcif.html).
- (65) Spek, A. L. PLATON SQUEEZE: A Tool for the Calculation of the Disordered Solvent Contribution to the Calculated Structure Factors. *Acta Cryst C* **2015**, *71* (1), 9–18. <https://doi.org/10.1107/S2053229614024929>.
- (66) Spek, A. L. Single-Crystal Structure Validation with the Program PLATON. *J Appl Cryst* **2003**, *36* (1), 7–13. <https://doi.org/10.1107/S0021889802022112>.
- (67) Spek, A. L. Structure Validation in Chemical Crystallography. *Acta Cryst D* **2009**, *65* (2), 148–155. <https://doi.org/10.1107/S090744490804362X>.

## Chapter 2: Studies of Cobalt Macrocyclic Compounds for CO<sub>2</sub> Reduction

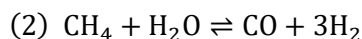
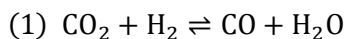
### *Introduction*

Many enzymes in nature exhibit reversible catalysis, including carbon monoxide dehydrogenases (CODHs)<sup>1,2</sup> and formate dehydrogenases (FDHs).<sup>3,4</sup> By the principle of microscopic reversibility, reversible catalysts must operate near the thermodynamic potential, or the standard Gibbs free energy, of the reaction.<sup>5</sup> However, performing these reactions reversibly using synthetic complexes has proven to be difficult. There are currently only two examples of synthetic homogeneous catalysts capable of both oxidizing HCO<sub>2</sub><sup>-</sup> and reducing CO<sub>2</sub> at significant rates, a bi-directional CO<sub>2</sub> reduction by Kang and co-workers<sup>6</sup> and our recently published reversible platinum bisdiphosphine catalyst.<sup>7</sup> Both of these complexes interconvert CO<sub>2</sub> and HCO<sub>2</sub><sup>-</sup>, a potentially useful energy storage medium. The difference, however, between reversible and bidirectional distinguishes the two catalysts from each other in a significant way. Reversible catalysts are a subset of bidirectional catalysts, catalysts that can function in both directions for a given reaction. Reversible catalysts operate with significant rates near the thermodynamic potential for said reaction in both directions, thus functioning with a minimal overpotential.<sup>5</sup> In Kang's example, the peak potentials for CO<sub>2</sub> reduction and HCO<sub>2</sub><sup>-</sup> oxidation with their Ir pincer compound differed by ~1 V.<sup>6</sup> In our example, with an electrode potential of -1.64 V vs. Fe(C<sub>5</sub>H<sub>5</sub>)<sub>2</sub><sup>+ / 0</sup>, the difference in energy from products to reactants, which can be thought of as a type of overpotential, was only 1.1 kcal/mol or 48 mV.<sup>7,8</sup>

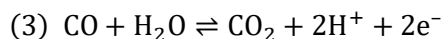
While the reversible interconversion of CO<sub>2</sub> and HCO<sub>2</sub><sup>-</sup> showed that using these thermodynamic considerations in rational design of the catalytic systems, HCO<sub>2</sub><sup>-</sup> has limited applicability in an industrial setting. In order to utilize reduced CO<sub>2</sub> in chemical processes, a more

useful product is CO, which can be mixed with H<sub>2</sub> to make synthesis gas, a feedstock for industrial chemical processes as well as a precursor to chemical fuels.<sup>9</sup>

One process commonly used today to produce carbon monoxide is the water gas shift reaction, described in Equation 1. This reversible reaction is carried out at high temperatures on various metal oxide and some noble metal catalysts.<sup>10</sup> Two major issues arise from the H<sub>2</sub> required for the reaction: first, it is most commonly sourced from the steam reforming of methane, a greenhouse gas itself and a fossil fuel. Second, high temperatures and pressures are required to convert methane to H<sub>2</sub>.<sup>11</sup> The chemical equation for steam reforming of methane is shown in Equation 2.

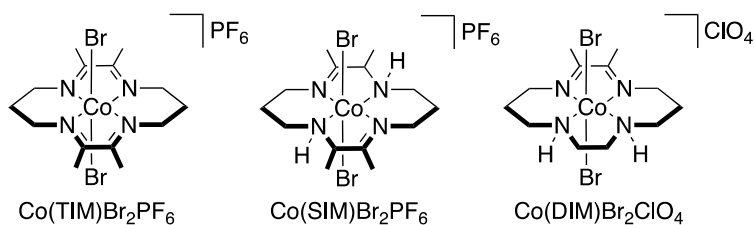


In order to avoid the use of hydrogen as a starting material for the reduction of CO<sub>2</sub> to CO, protons and electrons can be used as an equivalent of H<sub>2</sub>. CODH enzymes perform CO<sub>2</sub> to CO reduction reversibly with the use of proton and electron equivalents rather than molecular hydrogen, shown in Equation 3.

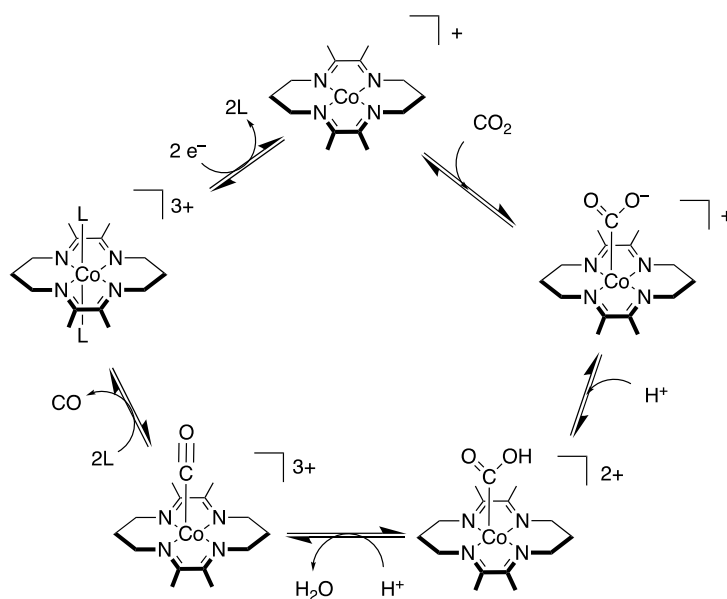


Our group has shown that leveling the energy landscape, minimizing the overall energy change of any step in a catalytic cycle, is an effective means of achieving reversible catalysis, so I set out to attempt this on the 2 H<sup>+</sup>, 2 e<sup>-</sup> reduction of CO<sub>2</sub> to CO and H<sub>2</sub>O. Several cobalt and nickel macrocyclic complexes have shown promise as CO<sub>2</sub> reduction electrocatalysts since 1980<sup>12-14</sup> after their syntheses in the 1970s by Busch and coworkers.<sup>15,16</sup> Interestingly, Lewis and coworkers showed that not only are many of these competent CO<sub>2</sub> reduction catalysts, but in certain solvent conditions, they also reversibly bind CO<sub>2</sub>.<sup>17</sup> This reversible binding of CO<sub>2</sub> gives us a thermodynamic handle to start with in the development of a reversible CO<sub>2</sub> reduction catalyst.

The complexes for this study are shown in Scheme 2.1 along with a proposed mechanism for CO<sub>2</sub> reduction using similar Co macrocycle complexes in Scheme 2.2.<sup>18</sup>



**Scheme 2.1:** Structures of compounds targeted in this study



**Scheme 2.2:** Proposed mechanism for the reversible reduction of CO<sub>2</sub> using a Co(TIM) species as a template

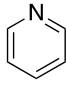
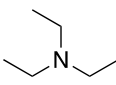
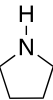
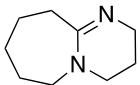
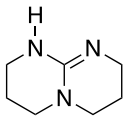
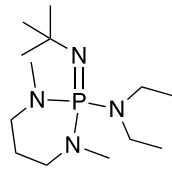
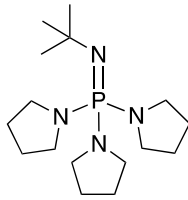
## Experimental

### General Methods

All manipulations were carried out under an N<sub>2</sub> atmosphere in a Vacuum Atmospheres glovebox. All chemicals were used as received from the supplier unless otherwise noted. All electrochemical analysis was performed in dry and degassed solvents that were purified by sparging with argon and passing over an alumina column using a solvent purification system (JC Meyer Solvent Systems) and stored over 3Å molecular sieves. [nBu<sub>4</sub>N][PF<sub>6</sub>] was purified by 3x recrystallization

from hot EtOH and dried overnight in a vacuum oven. Ferrocene was purified by sublimation. Synthesis of triflic acid salts, <sup>t</sup>Bu-P<sub>1</sub>-Pyrr•HOTf, BEMP•HOTf, TBD•HOTf, were performed on a Schlenk line by adding triflic acid (1.05 equiv.) dropwise to the base dissolved in dry Et<sub>2</sub>O, filtered in air, and dried under vacuum overnight before transferring to the inert atmosphere glove box. Synthesis of tetrafluoroboric acid salts, DBU•HBF<sub>4</sub>, pyrrolidine•HBF<sub>4</sub>, Et<sub>3</sub>N•HBF<sub>4</sub>, and pyridine•HBF<sub>4</sub>, were synthesized by adding newly purchased 50% HBF<sub>4</sub>•OEt<sub>2</sub> in Et<sub>2</sub>O to the base dissolved in dry Et<sub>2</sub>O. Use of older HBF<sub>4</sub> solutions yielded sticky oils.

**Table 2.1:** Structures of conjugate bases used in this chapter

Base Structure							
Abbreviation	Py <sup>19</sup>	Et <sub>3</sub> N <sup>19</sup>	Pyrr <sup>19</sup>	DBU <sup>19</sup>	TBD <sup>19</sup>	BEMP <sup>19</sup>	<sup>t</sup> Bu-P <sub>1</sub> -Pyrr <sup>20</sup>
pK <sub>a</sub> THF	5.5	12.5	13.5	16.9	21.0	19.0	20.2
pK <sub>a</sub> CH <sub>3</sub> CN	12.53	18.83	19.62	24.31	26.02	27.63	28.42

Note: pK<sub>a</sub>s are reported as the pK<sub>a</sub> of the conjugate acid, B•HOTf or B•HBF<sub>4</sub>. Values in THF do not include effects of ion pairing.

## Physical Methods

NMR data were collected on a Bruker DRX500 spectrometer with BBO probe, a Bruker DRX500 spectrometer with TCI cryoprobe, or a Bruker AVANCE600 Spectrometer with CBBFO cryoprobe and normalized to the proteo solvent impurity of the respective deuterated solvent.<sup>21</sup> UV-Visible spectra were collected on a Agilent Cary-60 spectrophotometer using fiber optic feed throughs to a nitrogen-filled glovebox.

## Electrochemical Techniques

All electrochemical experiments were performed on a Pine Wavedriver 10 bipotentiostat under an atmosphere of N<sub>2</sub> or CO<sub>2</sub>. All cyclic voltammetry (CV) experiments were performed with 1 mM equivalent initial amount of Co complex in solution in 100 mM [<sup>n</sup>Bu<sub>4</sub>N][PF<sub>6</sub>] in CH<sub>3</sub>CN or THF



(tetrahydrofuran) as noted on a 1 mm diameter glassy carbon disk electrode, glassy carbon rod counter electrode, and a quasireference electrode which consisted of a silver wire in a jacketed tube with a Vycor frit tip and filled with 100mM [<sup>n</sup>Bu<sub>4</sub>N][PF<sub>6</sub>] in CH<sub>3</sub>CN or THF, and the CVs were referenced to the E<sub>1/2</sub> of the Fe(C<sub>5</sub>H<sub>5</sub>)<sub>2</sub><sup>+ / 0</sup> couple using a ferrocene internal standard. All cyclic voltammograms are shown at a scan rate of 100 mV/s unless otherwise noted. Bulk electrolysis experiments were performed in an H-shaped cell with a fine glass frit separating the two compartments and sealed with Teflon-lined caps with seals around the electrodes. Carbon fabric electrodes were used for both the working and counter electrodes, and the quasireference electrode described above. A drop of Hg was included in the working electrode side to amalgamate any Co<sup>0</sup> particles. On the counter electrode side, 10 equivalents of ferrocene (with respect to the total amount of the Co complex, dissolved and undissolved) was added. Significant solubility issues arose with all of the Co complexes in THF, which made the true concentration of analyte in THF solution less than 1 mM and are henceforth labeled as saturated solutions of Co complex. Spectroelectrochemical analysis was performed using the aforementioned spectrophotometer setup using a Pine quartz cell and honeycomb electrode setup using the above described quasireference electrode rather than the built in Ag<sup>+ / 0</sup> reference.

#### Synthesis of Co(TIM)Br<sub>2</sub>PF<sub>6</sub>

Diaminopropane•2HBr (19.45 g) was synthesized fresh from diaminopropane (8.8 g) and excess 48% HBr resulting in a 69% yield. 19.45 g of diaminopropane•2HBr was suspended in 50 mL of methanol and cooled in an ice bath. 7.10 g of biacetyl was added to the cold solution in 20 mL of methanol. KOH (4.63 g) was dissolved in 50 mL of methanol and added dropwise to the biacetyl/diaminopropane solution ensuring the temperature stayed below 5°C. After the addition was complete, it was allowed to stir while cooled by the ice bath for 15 minutes. A solution of Co(OAc)<sub>2</sub>•4H<sub>2</sub>O (10.46 g) in 100 mL of methanol was added to the reaction mixture. The resulting mixture was stirred overnight. NH<sub>4</sub>PF<sub>6</sub> (6.72 g) was added, and the solution was cooled and

filtered, yielding 6.16 g (24% yield) of dark green  $\text{Co}(\text{TIM})\text{Br}_2\text{PF}_6$ . UV-vis  $\lambda_{\text{max}}$ , nm ( $\epsilon$ ,  $\text{M}^{-1}\text{cm}^{-1}$ ) 283 (56700), 400 (3270), 601 (83).  $^1\text{H}$  NMR ( $\text{CD}_3\text{CN}$ , 600 MHz) 4.12 (8H, m), 2.71 (12H, s) 2.58 (4H, m).

#### Synthesis of $\text{Co}(\text{SIM})\text{Br}_2\text{PF}_6$

5.3g of  $\text{Co}(\text{TIM})\text{Br}_2\text{PF}_6$  was suspended in 350 mL of methanol. 4.4 mL of 50% hypophosphorous acid was added to the suspension. The solution rapidly turned to a dark purple, then brown, then eventually green. After 1 hour of stirring, 5 mL HBr and 5 g  $\text{NH}_4\text{PF}_6$  was added to precipitate  $\text{Co}(\text{SIM})\text{Br}_2\text{PF}_6$  (0.81 g, 39% yield).  $^1\text{H}$ -NMR (500MHz,  $\text{CD}_3\text{CN}$ , ppm): 5.23 (2H, s), 3.91 (2H, s), 3.87 (4H, s), 3.11 (4H, t), 2.68 (2H, m), 2.40 (2H, s), 2.34 (6H, s), 1.61 (6H, d). UV-vis  $\lambda_{\text{max}}$ , nm ( $\epsilon$ ,  $\text{M}^{-1}\text{cm}^{-1}$ ) 210 (21900), 262 (10500), 312(16500), 387 (3220), 661 (68).

#### Synthesis of $\text{Co}(\text{DIM})\text{Br}_2\text{ClO}_4$

Synthesized by Alessandra Zito according to literature procedure.<sup>15</sup>  $^1\text{H}$  NMR ( $\text{CD}_3\text{CN}$ , 600 MHz) 5.45 (2H, s), 4.29 (2H, d), 3.77 (2H, t), 3.15 (2H, q), 2.96 (2H, dd), 2.84 (4H, m), 2.71 (6H, s), 2.40 (2H, dd), 2.11 (2H, m). UV-vis  $\lambda_{\text{max}}$ , nm ( $\epsilon$ ,  $\text{M}^{-1}\text{cm}^{-1}$ ) 210 (32300), 260 (18100), 300 (32200), 389 (3450), 636 (133).

### *Results and Discussion*

#### Synthesis and Characterization

$\text{Co}(\text{TIM})\text{Br}_2\text{PF}_6$ ,<sup>15</sup>  $\text{Co}(\text{SIM})\text{Br}_2\text{PF}_6$ ,<sup>16</sup> and  $\text{Co}(\text{DIM})\text{Br}_2\text{ClO}_4$ <sup>22</sup> were synthesized according to modified literature procedures to form the dibromides rather than the published dichloride analogues.  $^1\text{H}$  and  $^{13}\text{C}$ -NMR spectra of  $\text{Co}(\text{SIM})\text{Br}_2\text{PF}_6$  matched the NMR spectra of the same complexes that were fully characterized by Alessandra Zito, and the others matched literature reports.

## Electrochemical Analysis

In order to explore the electrochemical properties of  $\text{Co}(\text{TIM})\text{Br}_2\text{PF}_6$ ,  $\text{Co}(\text{SIM})\text{Br}_2\text{PF}_6$ , and  $\text{Co}(\text{DIM})\text{Br}_2\text{ClO}_4$ , cyclic voltammograms of each complex are shown in Figure **2.1**. Each of the electrochemical experiments were performed in tetrahydrofuran (THF) with 100 mM  $[\text{nBu}_4\text{N}][\text{PF}_6]$  as a supporting electrolyte and referenced to the  $\text{Fe}(\text{C}_5\text{H}_5)_2^{+/\circ}$  couple.  $\text{Co}(\text{TIM})\text{Br}_2\text{PF}_6$ ,  $\text{Co}(\text{SIM})\text{Br}_2\text{PF}_6$ , and  $\text{Co}(\text{DIM})\text{Br}_2\text{ClO}_4$  are sparingly soluble in THF, so 5 mg of each were added to the electrolyte solution forming a saturated solution of each. Later studies on  $\text{Co}(\text{SIM})\text{Br}_2\text{PF}_6$  showed the maximum concentration in THF to be no more than 0.063 mM.

The cyclic voltammogram of  $\text{Co}(\text{TIM})\text{Br}_2\text{PF}_6$  (blue trace, Figure **2.1**) shows three reductive events centered at  $-0.590$ ,  $-0.864$ , and  $-2.030$  V vs.  $\text{Fe}(\text{C}_5\text{H}_5)_2^{+/\circ}$ . Cyclic voltammograms of  $\text{Co}(\text{SIM})\text{Br}_2\text{PF}_6$  (black trace, Figure **2.1**) show two quasi-reversible couples, which are attributed to the  $\text{Co}^{\text{III}/\text{II}}$  and  $\text{Co}^{\text{II}/\text{I}}$  couples at  $-0.587$  and  $-1.880$  V vs.  $\text{Fe}(\text{C}_5\text{H}_5)_2^{+/\circ}$ , respectively. These potentials are consistent with previously reported values.<sup>17</sup>  $\text{Co}(\text{DIM})\text{Br}_2\text{ClO}_4$  (red trace, Figure **2.1**) showed two reductive events centered at  $-0.556$  and  $-1.42$  V vs.  $\text{Fe}(\text{C}_5\text{H}_5)_2^{+/\circ}$  and an irreversible reduction ( $E_{\text{pc}}$ ) at  $-2.09$  V vs.  $\text{Fe}(\text{C}_5\text{H}_5)_2^{+/\circ}$ . Lewis and coworkers assigned the  $\text{Co}^{\text{II}/\text{I}}$  reduction events at  $-0.76$ ,  $-1.80$ , and  $-1.31$  V for the  $\text{Co}(\text{TIM})$ ,  $\text{Co}(\text{SIM})$ , and  $\text{Co}(\text{DIM})$  complexes, respectively, but given their potentials and similar ligand environment, it is likely that the reductive events in all of the complexes near  $-0.6$  and  $-2.0$  V vs.  $\text{Fe}(\text{C}_5\text{H}_5)_2^{+/\circ}$  are metal based, while the third intermediate reductive event seen in  $\text{Co}(\text{TIM})\text{Br}_2\text{PF}_6$  and  $\text{Co}(\text{DIM})\text{Br}_2\text{ClO}_4$  are likely ligand-based due to the conjugated pi system in the ligand being easy to reduce in both the TIM and DIM ligands<sup>23</sup> while no such conjugation exists in the SIM ligand.

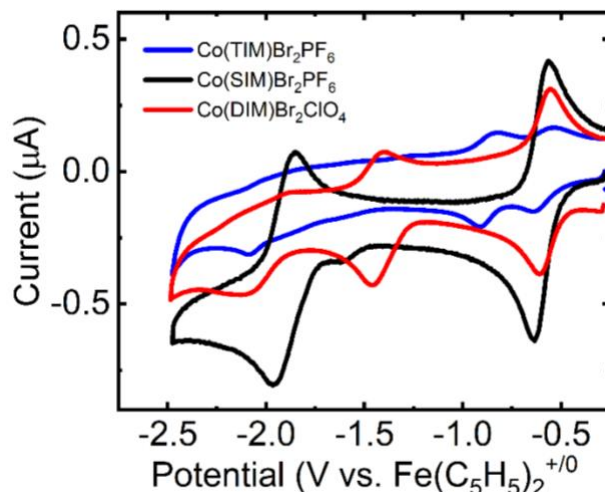


**Figure 2.1:** Cyclic voltammograms of saturated solutions of Co(TIM)Br<sub>2</sub>PF<sub>6</sub> (Blue), Co(SIM)Br<sub>2</sub>PF<sub>6</sub> (Black), and Co(DIM)Br<sub>2</sub>ClO<sub>4</sub> (Red) in 100 mM [nBu<sub>4</sub>N][PF<sub>6</sub>] in THF

**Table 2.2:** Measured reduction potentials and CO<sub>2</sub> binding constants of Co complexes

Complex	$E_{1/2}$ Co <sup>III/II</sup>	$E_{1/2}$ L <sup>0/-1</sup>	$E_{1/2}$ Co <sup>II/I</sup>	$E_{1/2}$ Co <sup>II/I</sup> under CO <sub>2</sub>	$K_{CO_2}$ (THF)	$K_{CO_2}$ (DMSO) <sup>17</sup>
Co(TIM)Br <sub>2</sub> PF <sub>6</sub>	-0.590	-0.864	-2.03	-1.97	310	<4
Co(SIM)Br <sub>2</sub> PF <sub>6</sub>	-0.601	N/A	-1.91	-1.75	73000	1.0(3)•10 <sup>5</sup>
Co(DIM)Br <sub>2</sub> ClO <sub>4</sub>	-0.556	-1.42	-2.09	---	---	<4

K values reported in M<sup>-1</sup>,

$E_{1/2}$  values reported in V vs. Fe(C<sub>5</sub>H<sub>5</sub>)<sub>2</sub><sup>+0</sup>

## CO<sub>2</sub> Binding

CO<sub>2</sub> was previously reported to reversibly bind to Co(TIM)Br<sub>2</sub>PF<sub>6</sub>, Co(SIM)Br<sub>2</sub>PF<sub>6</sub>, and Co(DIM)Br<sub>2</sub>ClO<sub>4</sub>, when they are in the formal Co<sup>I</sup> oxidation state.<sup>17</sup> In the proposed mechanism for CO<sub>2</sub> reduction to CO in Scheme 2.2, CO<sub>2</sub> binds the metal center first, followed by protonation, cleavage of the C-O bond, and eventual release of CO from the Co<sup>III</sup> center. Lewis and coworkers determined that the binding constants for CO<sub>2</sub> were <4 M<sup>-1</sup> for both Co(TIM)Br<sub>2</sub>PF<sub>6</sub> and Co(DIM)Br<sub>2</sub>ClO<sub>4</sub>, and 1.0 x 10<sup>5</sup> for M<sup>-1</sup> Co(SIM)Br<sub>2</sub>PF<sub>6</sub> in DMSO.<sup>17</sup> Equation 4 is based on the Nernst equation, where q is the number of CO<sub>2</sub> molecules bound to the reduced species. The  $E_{1/2}$  of the Co<sup>II/I</sup> couple of the complex with 1 atmosphere of CO<sub>2</sub> ( $E_{1/2}$ ) and the  $E_{1/2}$  of the Co<sup>II/I</sup> couple under an atmosphere of N<sub>2</sub> ( $E^{\circ}$ ) were used to estimate the binding constant of CO<sub>2</sub> to the complex ( $K_{CO_2}$ ) through a single point measurement.

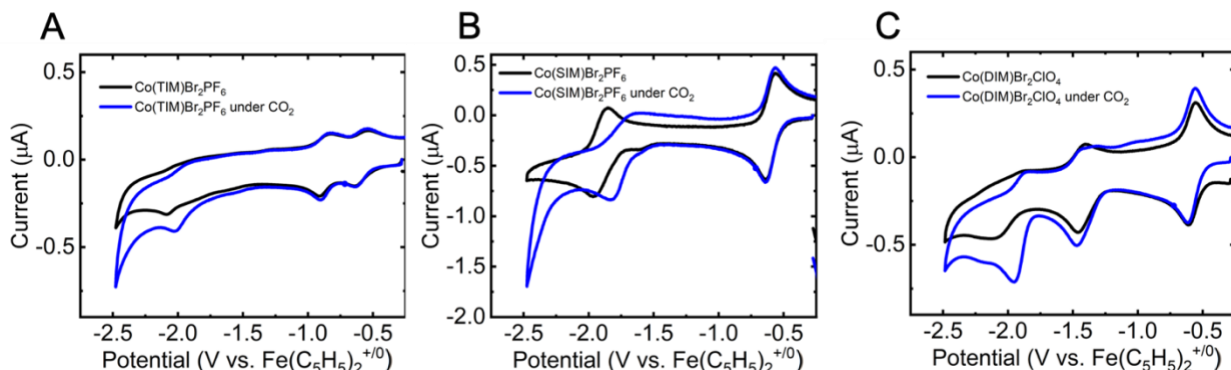


**Figure 2.2:** Cyclic voltammograms of Co(TIM)Br<sub>2</sub>PF<sub>6</sub> (A), Co(SIM)Br<sub>2</sub>PF<sub>6</sub> (B), and Co(DIM)Br<sub>2</sub>ClO<sub>4</sub> (C) in THF (black traces) and under CO<sub>2</sub> (blue traces) in 100mM [<sup>n</sup>Bu<sub>4</sub>N][PF<sub>6</sub>].

$$(4) E_{1/2} = E^{o'} + \frac{RT}{nF} \ln(K_{CO_2}) + q \frac{RT}{nF} \ln[CO_2]$$

In order to better understand the interaction of the three cobalt complexes with CO<sub>2</sub>, CVs were performed of Co(TIM)Br<sub>2</sub>PF<sub>6</sub>, Co(SIM)Br<sub>2</sub>PF<sub>6</sub>, and Co(DIM)Br<sub>2</sub>ClO<sub>4</sub> under an atmosphere of CO<sub>2</sub> and are shown in Figure 2.2 compared to the CVs under N<sub>2</sub>. CO<sub>2</sub> was bubbled through each solution for 5 minutes using a THF pre-bubbler in order to minimize the loss of THF from the solution of analyte. The concentration of CO<sub>2</sub> in solution was estimated to be 340 mM, which is the maximum concentration of CO<sub>2</sub> in a solution of THF at 25°C.<sup>24</sup>

The cyclic voltammograms of Co(TIM)Br<sub>2</sub>PF<sub>6</sub>, Co(SIM)Br<sub>2</sub>PF<sub>6</sub>, and Co(DIM)Br<sub>2</sub>ClO<sub>4</sub> under CO<sub>2</sub> show a shift in the potential of the Co<sup>II/I</sup> redox couple. Using Equation 4, the binding constants of CO<sub>2</sub> to each complex were estimated in THF based on single point measurements at the CO<sub>2</sub> concentration of 340 mM assuming that only one CO<sub>2</sub> molecule binds per cobalt center and are compiled in Table 2.2. While the CO<sub>2</sub> binding constant calculated here in THF for the reduced Co(SIM) compound (7.3 • 10<sup>5</sup> M<sup>-1</sup>) lies close to the value reported by Lewis and coworkers in DMSO (1.0(3) • 10<sup>5</sup> M<sup>-1</sup>), our calculated binding constant for the reduced Co(TIM) compound (310 M<sup>-1</sup>) is significantly higher than that estimated by others (<4 M<sup>-1</sup>) based on our suggested reassignment of the Co<sup>II/I</sup> couple. Further studies on CO<sub>2</sub> binding with these compounds should

include the variation of CO<sub>2</sub> concentration in order to minimize error in the highly reduction potential-dependent calculation.

### Electrocatalytic Studies

After showing the shift in potential that is associated with CO<sub>2</sub> binding, the next step in the proposed catalytic mechanism is to protonate the bound CO<sub>2</sub>. Two weak acids were chosen for this study, <sup>t</sup>Bu-P<sub>1</sub>-Pyrr•HOTf and BEMP•HOTf because of their minimal interaction with the reduced Co(SIM) species (Figure 2.3). While a slight increase in current is seen with BEMP•HOTf (red trace), no current increase is observed with <sup>t</sup>Bu-P<sub>1</sub>-Pyrr•HOTf (blue trace). Use of stronger acids, DBU•HBF<sub>4</sub> and Pyrr•HOTf, showed large increases in current along with an anodic shift in onset potential, which is consistent with catalytic hydrogen evolution. The increase in current upon addition of BEMP•HOTf was deemed insignificant in this situation because the Co<sup>II/I</sup> couple in the presence of CO<sub>2</sub> occurs at a potential that is about 160 mV more positive than under N<sub>2</sub>. We hypothesize that hydrogen evolution may be disfavored when these more positive potentials are used.

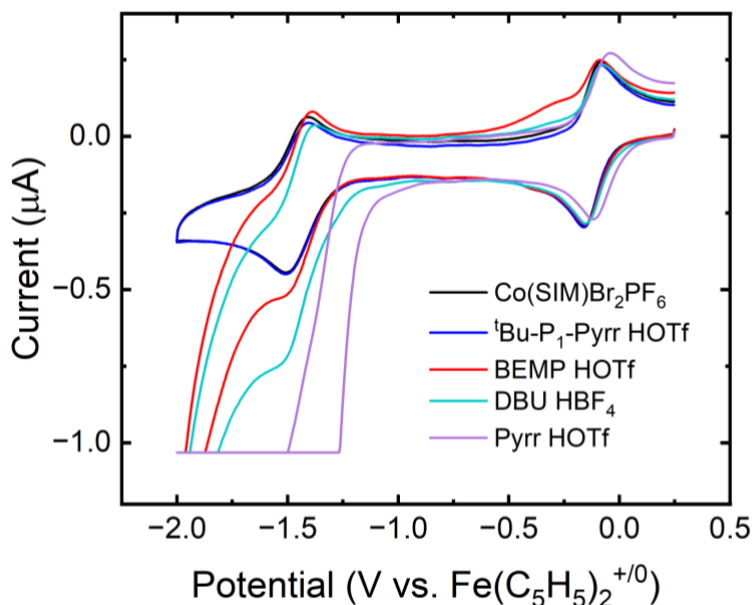


**Figure 2.3:** Cyclic voltammograms of a saturated solution of Co(SIM)Br<sub>2</sub>PF<sub>6</sub> with acids in 100 mM [<sup>n</sup>Bu<sub>4</sub>N][PF<sub>6</sub>] in THF under an atmosphere of N<sub>2</sub>. Acids were sequentially added in 10 equivalents based on a target 1 mM concentration. Note: Due to issues with the potentiostat, currents below -1 μA are not shown.

Co(SIM)Br<sub>2</sub>PF<sub>6</sub> was chosen for the major part of these studies for a few reasons: there are no ligand centered reductions that complicate analysis and more reversible reductions under both N<sub>2</sub> and CO<sub>2</sub>. It also has the highest relative solubility of the three complexes in THF. Previous studies by Dr. Steven Chabolla and Alessandra Zito have observed that the Co<sup>II/I</sup> is more reversible in THF than in CH<sub>3</sub>CN. The CVs of Co(SIM)Br<sub>2</sub>PF<sub>6</sub> under CO<sub>2</sub> in the presence of <sup>t</sup>Bu-P<sub>1</sub>-Pyrr•HOTf (pK<sub>a</sub> = 20.2) and BEMP•HOTf (pK<sub>a</sub> = 19.0) (two weak phosphazine acids) are shown in Figure 2.4. Upon adding CO<sub>2</sub>, a slight increase in current is noted at about -2.3 V, which could be associated with the reduction of the Co<sup>II</sup>(SIM)CO<sub>2</sub> species or onset of catalysis. Adding varying concentrations and strengths of acids, the current continues to increase, suggesting that the CO<sub>2</sub> bound species is indeed reacting with the acids in solution and converting the CO<sub>2</sub> to a reduced species.

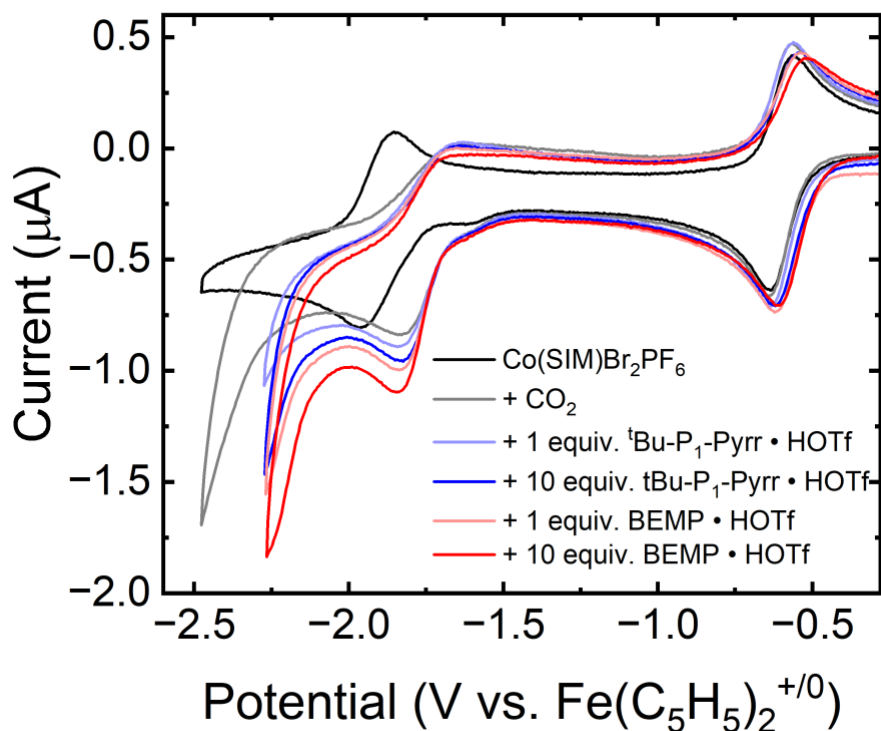


**Figure 2.4:** Cyclic voltammograms of Co(SIM)Br<sub>2</sub>PF<sub>6</sub> with CO<sub>2</sub> and weak acids in 100 mM [<sup>n</sup>Bu<sub>4</sub>N][PF<sub>6</sub>] in THF. Experiments were performed under an atmosphere of N<sub>2</sub> (black trace) or CO<sub>2</sub> (all other traces) and <sup>t</sup>Bu-P<sub>1</sub>-Pyrr•HOTf (blue), BEMP•HOTf (red).

Cyclic voltammograms of  $\text{Co}(\text{TIM})\text{Br}_2\text{PF}_6$  and  $\text{Co}(\text{DIM})\text{Br}_2\text{ClO}_4$  were performed under similar conditions, and they are plotted in Figure 2.5 and Figure 2.6, respectively. Each compound has a shift in the peak potential of the  $\text{Co}^{\text{II/I}}$  reduction that indicates  $\text{CO}_2$  binding. The lack of a pronounced return oxidation wave as with the parent compound indicates irreversibility, making this an  $\text{E}_r\text{C}_{\text{irr}}$  process (a reversible electrochemical process followed by a irreversible chemical process).<sup>25</sup> This irreversibility may be caused by tight binding of  $\text{CO}_2$  to the metal center or additional chemical processes after reduction. Both compounds have an increase in current after  $\text{CO}_2$  addition, which led to a far more pronounced reductive event in  $\text{Co}(\text{DIM})\text{Br}_2\text{ClO}_4$ . Addition of the weak acids to these solutions of Co complexes led to further increases in current that may also be indicative of catalysis. Additionally, in the  $\text{Co}(\text{DIM})$  case, there was a 57 mV positive shift in peak potential of what we are attributing to the ligand-centered reduction after the addition of acid to the  $\text{CO}_2$  saturated solution. A possible explanation for the shift is a fast irreversible chemical step after reduction, likely protonation and possible reduction of the conjugated ligand backbone of DIM. The shift in the ligand reduction potential is not correlated with a shift in the  $\text{Co}^{\text{II/I}}$  couple, which actually shifts to slightly more negative peak potentials after the addition of the acids.



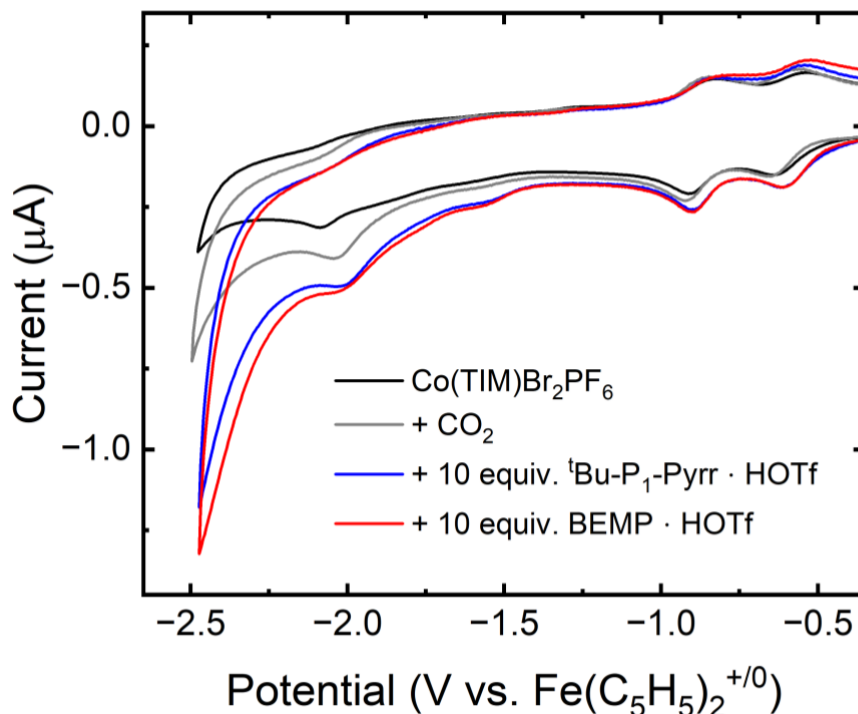


**Figure 2.5:** Cyclic voltammograms of Co(TIM)Br<sub>2</sub>PF<sub>6</sub> with CO<sub>2</sub> and acids in 100 mM [<sup>n</sup>Bu<sub>4</sub>N][PF<sub>6</sub>] in THF. Experiments were performed under N<sub>2</sub> (black) or in the presence of CO<sub>2</sub> (gray) with <sup>t</sup>Bu-P<sub>1</sub>-Pyrr•HOTf (blue) and BEMP•HOTf (red).

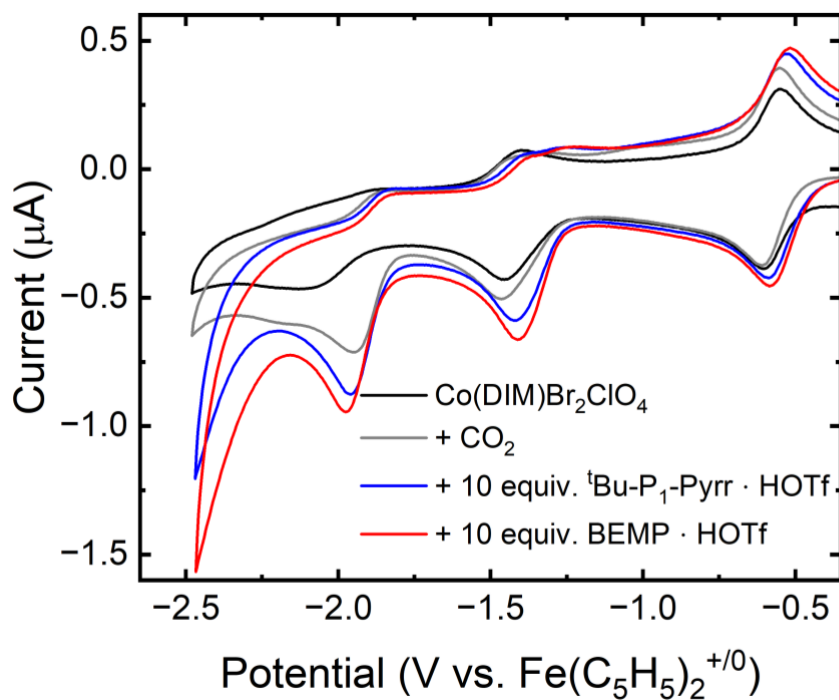


**Figure 2.6:** Cyclic voltammograms of Co(DIM)Br<sub>2</sub>ClO<sub>4</sub> with CO<sub>2</sub> and acids in 100 mM [<sup>n</sup>Bu<sub>4</sub>N][PF<sub>6</sub>] in THF. Experiments were performed under N<sub>2</sub> (black) or in the presence of CO<sub>2</sub> (gray) with <sup>t</sup>Bu-P<sub>1</sub>-Pyrr•HOTf (blue) and BEMP•HOTf (red).

## Attempted Electrocatalytic CO<sub>2</sub> Reduction Using Co(SIM)Br<sub>2</sub>PF<sub>6</sub>

With the increase in current seen from the cyclic voltammetric experiments, electrocatalytic CO<sub>2</sub> reduction was attempted using Co(SIM)Br<sub>2</sub>PF<sub>6</sub> as a catalyst. Chronoamperometric studies were performed under various conditions to assess the catalytic activity of Co(SIM)Br<sub>2</sub>PF<sub>6</sub> in the presence of various acids in CH<sub>3</sub>CN and THF. In each case, the potential was held at the potential at which the current was at its max for the Co<sup>II/I</sup> event, approximately -1.7 V vs. Fe(C<sub>5</sub>H<sub>5</sub>)<sub>2</sub><sup>+0</sup> in all cases. Figure 2.7 shows the chronoamperometry traces of the bulk reduction of Co(SIM)Br<sub>2</sub>PF<sub>6</sub> in the presence BEMP•HOTf and CO<sub>2</sub>. Each experiment shows a large initial current, both near 2 mA, passing 0.104 C and 0.179 C for the unfiltered and filtered solutions, respectively. After 1-2 minutes, the steady current is followed by a precipitous drop that decays to essentially zero in the case on the right. The only difference between the two traces is that the solution for the trace on the left was not filtered prior to reduction, which shows that the sustained supply of fresh Co(SIM)Br<sub>2</sub>PF<sub>6</sub> into solution likely sustained a small amount of the current for longer.

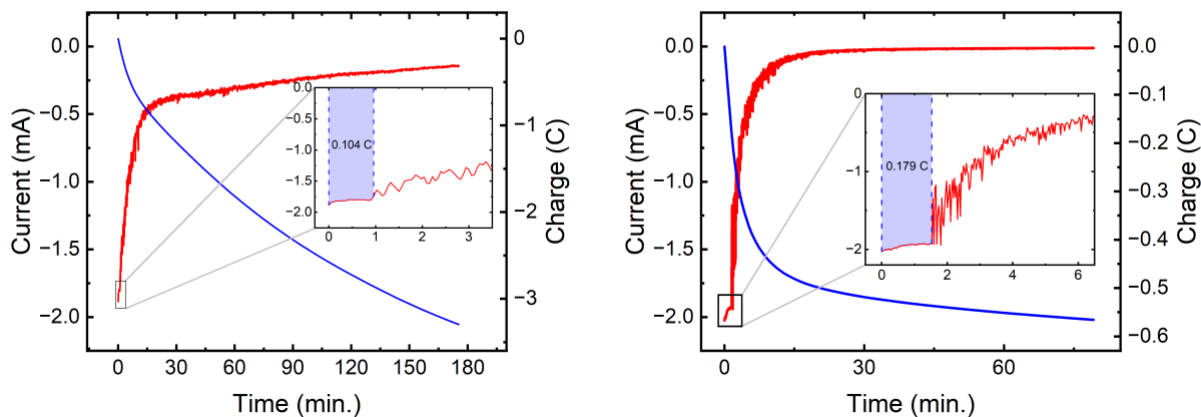


**Figure 2.7:** Chronoamperograms of the bulk electrolytic reduction of Co(SIM)Br<sub>2</sub>PF<sub>6</sub> in THF. Experiments were performed in stirred solutions of 100 mM [nBu<sub>4</sub>N][PF<sub>6</sub>] in THF in the presence of CO<sub>2</sub> and BEMP•HOTf. Red traces indicate current, blue traces indicate total charge passed, and the insets depict the first few minutes of the electrolysis where the current response was stable. On the left, solid remained suspended throughout the course of the electrolysis, and on the right, the solid Co(SIM)Br<sub>2</sub>PF<sub>6</sub> was filtered off prior to electrolysis.

In CH<sub>3</sub>CN (Figure 2.8), the electrolyses had similar results, first showing a steady current of ~15 mA followed by a major drop off in current. The most likely cause of the drastic drop in current in all of these cases is the compound in solution reduces entirely and does such little turnover that there is no or nearly no steady state current after all of the compound in solution is reduced. Additionally, as the reduction proceeds, the solution turns from a green color to gray/colorless. Pre- and post-electrolysis UV-Visible spectra of Electrolysis 2 (Figure 2.7, right) is shown in Figure 2.9. The post-electrolysis spectrum, shown in red, is most consistent with a mixture of mostly Co<sup>I</sup>(SIM)CO<sup>+</sup> and with a small amount of Co<sup>I</sup>(SIM)CO<sub>2</sub><sup>+</sup>, reported by Fujita and coworkers.<sup>14</sup> They reported a high binding constant  $K > 10^8 \text{ M}^{-1}$  for the yellow Co<sup>I</sup>(SIM)-CO complex,<sup>14</sup> which likely explains the massive drop in current even in the presence of acid. Under reductive conditions, the reduced cobalt center binds too tightly to CO, not allowing catalysis to proceed.

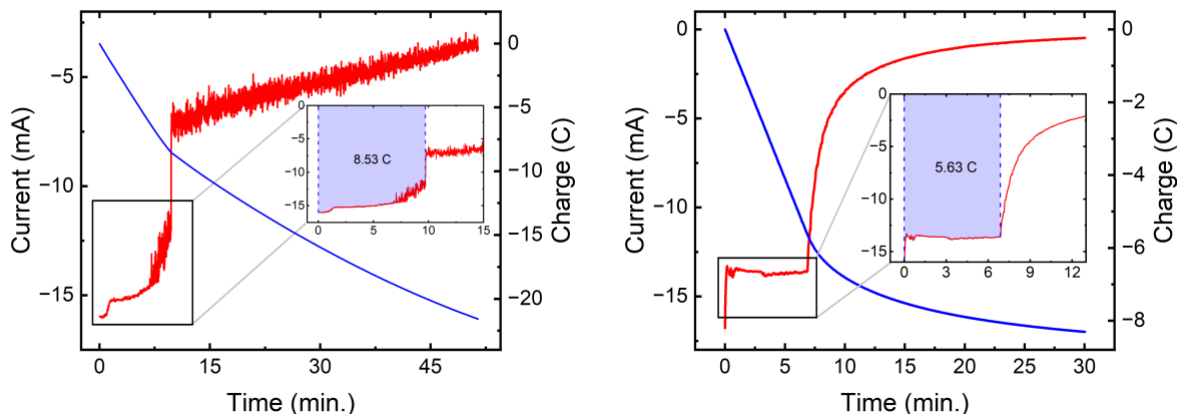


**Figure 2.8:** Chronoamperograms of the bulk electrolytic reduction of Co(SIM)Br<sub>2</sub>PF<sub>6</sub> in CH<sub>3</sub>CN. Experiments were performed in stirred solutions of 100 mM [<sup>n</sup>Bu<sub>4</sub>N][PF<sub>6</sub>] in CH<sub>3</sub>CN the presence of CO<sub>2</sub> and (A) Py•HBF<sub>4</sub> and (B) EtN<sub>3</sub>•HBF<sub>4</sub>. Red traces indicate current, blue traces indicate total charge passed, and the insets depict the first few minutes of the electrolysis where the current response was stable.

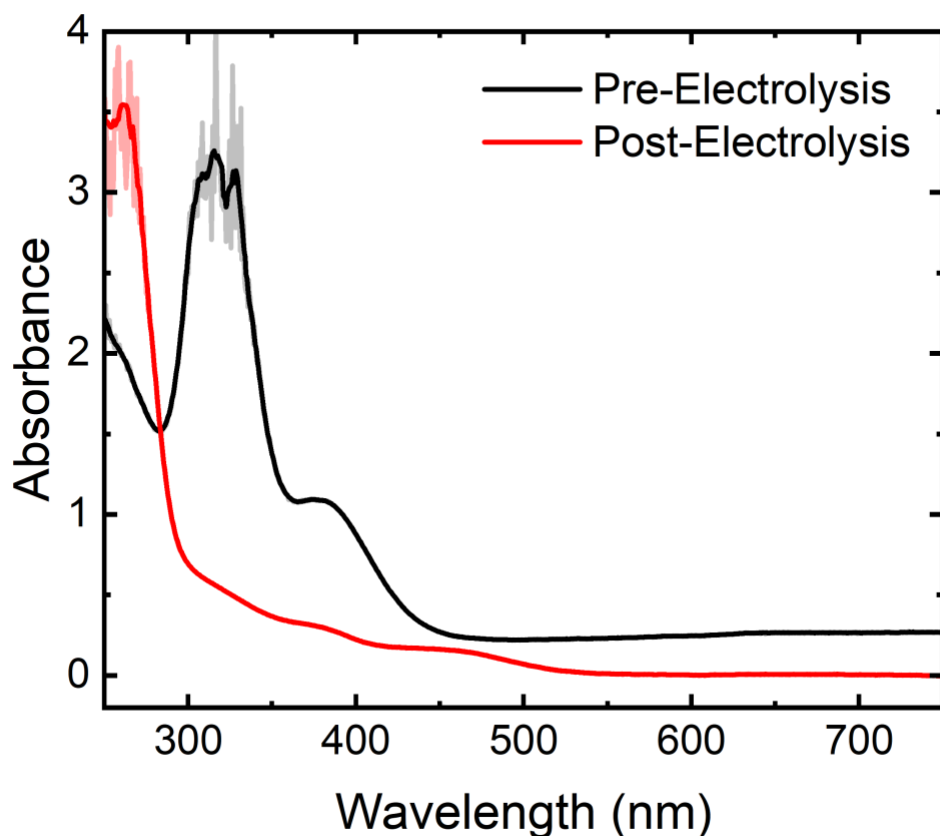


**Figure 2.9:** Pre- (black) and post-electrolysis (red) UV-Visible spectra of Electrolysis 2 (Table 2.3). Light colored traces are raw data with points at 10 absorbance units (detector saturation point) removed, and (dark lines) 10 point adjacent averages of the remaining data.

**Table 2.3:** Performance of electrolysis attempts

<i>Electrolysis</i>	<i>Solvent</i>	<i>Acid (concentration)</i>	<i>Charge Passed (time)</i>	<i>TON(CO)</i>	<i>TON(H<sub>2</sub>)</i>
1	THF	BEMP•HOTf (10 mM)	3.3 C (177 min.)	0.2	Trace
2	THF	BEMP•HOTf (10 mM)	0.57 C (80 min.)	Trace	0
3	CH <sub>3</sub> CN	Et <sub>3</sub> N•HBF <sub>4</sub> (10 mM)	21.8 C (51 min.)	Trace	--- <sup>a</sup>
4	CH <sub>3</sub> CN	Py•HBF <sub>4</sub> (10 mM)	8.3 C (30 min.)	0.17	0.52

<sup>a</sup>A large amount of H<sub>2</sub> formed in this experiment, but it was not quantified due to instrument issues

### Spectroelectrochemical Characterization

In order to understand the increase in current in the cyclic voltammograms, it may be possible to characterize the products of reduction and protonation by the weak acids. One method of *in situ* characterization is spectroelectrochemistry, where reduction products can be characterized by UV-Visible spectroscopy by performing small scale bulk electrolyses of the

solution in the path of the spectrophotometer. Figure **2.10** shows an attempt to ascertain the spectroelectrochemical profile of  $\text{Co}(\text{SIM})\text{Br}_2\text{PF}_6$  under an atmosphere of  $\text{N}_2$  in 100 mM  $n\text{Bu}_4\text{NPF}_6$  in THF. After polarization of the electrode to  $-215$  mV vs.  $\text{Fe}(\text{C}_5\text{H}_5)_2^{+/0}$  for 10 minutes, the UV-visible spectrum of  $\text{Co}(\text{SIM})\text{Br}_2\text{PF}_6$  was collected, showing peaks at 400 nm and 320 nm. At this potential, consulting the cyclic voltammograms of  $\text{Co}(\text{SIM})\text{Br}_2\text{PF}_6$ , the spectrum was consistent with the spectrum of the parent  $\text{Co}^{\text{III}}$  parent species. Upon polarization to  $-1.215$  V vs.  $\text{Fe}(\text{C}_5\text{H}_5)_2^{+/0}$ , the spectrum showed no obvious growth of any peaks that would correspond to a reduced species. Upon further polarization to more negative potentials, again, no growth of any peaks was noted as shown by the green and blue traces in Figure **2.10**. Although the solubility of the  $\text{Co}^{\text{III}}$  species has always been of concern (experimentally found to be  $<0.065$  mM in THF), the lack of any peaks upon reduction suggests that the bands that would be associated with a reduced species do not have a sufficiently high molar absorptivity to be useful in THF or that there is significant decomposition of the metal complex leading to products that do not absorb in the UV-visible spectra. Consequently, work has been done to generate a more soluble  $\text{Co}(\text{SIM})^n$  starting material, and further work was performed in mixed  $\text{CH}_3\text{CN}$  and THF solutions, which dissolve  $\text{Co}(\text{SIM})\text{Br}_2\text{PF}_6$  much more readily without major changes to the  $E_{1/2}$  potentials as shown in Figure **2.11** with tabulated reduction potentials in Table **2.4**. If dilution of the metal complex was a major contributor to the electrochemical response, addition of  $\text{CH}_3\text{CN}$  ( $\sim 20\%$  by volume) would decrease, but because the solubility is so much greater in the mixed solutions, the current responses actually increase.

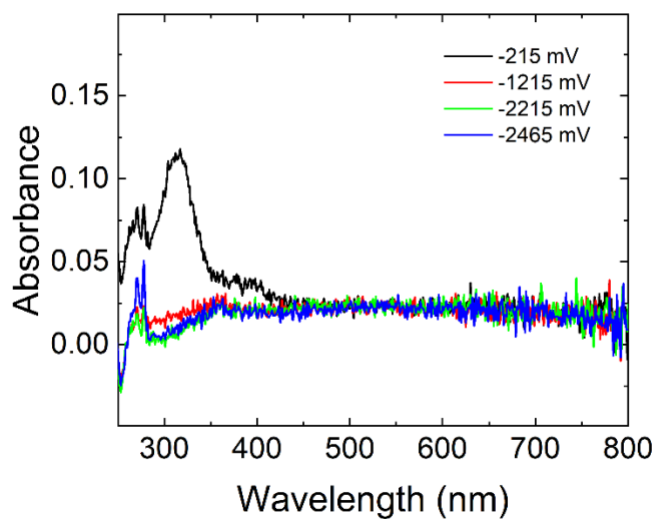


**Figure 2.10:** Spectroelectrochemistry of  $\text{Co}(\text{SIM})\text{Br}_2\text{PF}_6$  in THF. Experiments were performed in 100 mM  $[\text{nBu}_4\text{N}][\text{PF}_6]$  in THF. Working electrode: Pt honeycomb. Counter electrode: Pt. Reference electrode:  $\text{Ag}^{+}/^0$ .

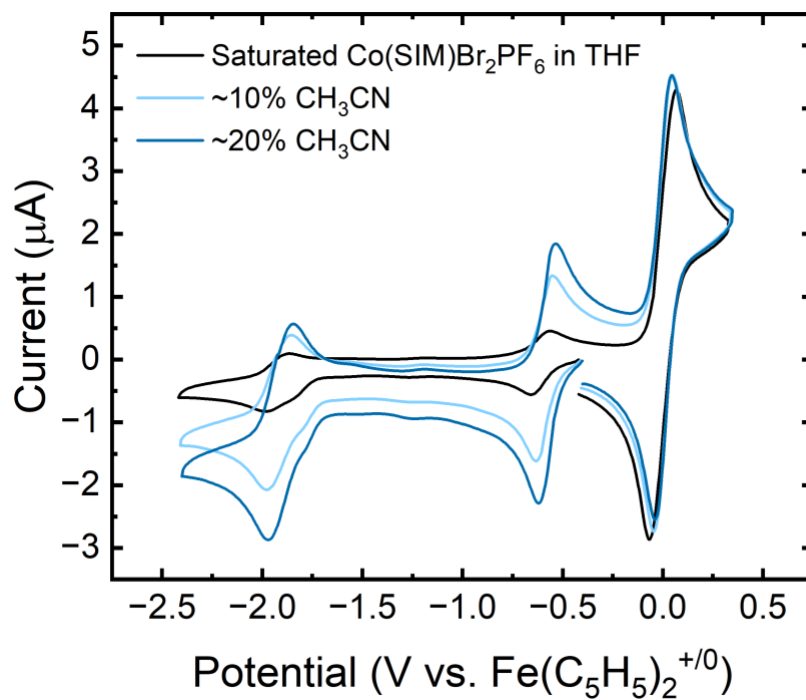


**Figure 2.11:** Cyclic voltammograms of  $\text{Co}(\text{SIM})\text{Br}_2\text{PF}_6$  THF with increasing concentration of  $\text{CH}_3\text{CN}$ . Experiments were performed in initially 100 mM  $[\text{nBu}_4\text{N}][\text{PF}_6]$  in THF with increasing concentration of  $\text{CH}_3\text{CN}$ .

**Table 2.4:** Tabulated reduction potentials of Co(SIM)Br<sub>2</sub>PF<sub>6</sub> in mixed THF and CH<sub>3</sub>CN

	<i>Co<sup>III/II</sup></i>	<i>Co<sup>II/I</sup></i>
<i>100% THF</i>	-0.609	-1.924
<i>9% CH<sub>3</sub>CN</i>	-0.591	-1.916
<i>16% CH<sub>3</sub>CN</i>	-0.577	-1.907
<i>100% CH<sub>3</sub>CN</i>	-0.441	-1.827

The spectroelectrochemical profile of Co(SIM)Br<sub>2</sub>PF<sub>6</sub> in CH<sub>3</sub>CN under N<sub>2</sub> had an absorption spectrum with far more detail and are shown in Figure 2.12. Similar to observations seen by Fujita and coworkers,<sup>14</sup> under an atmosphere of N<sub>2</sub>, the Co(III) compound shows an intense peak near 310 nm with a shoulder at 376 nm and a weak d-d band at 656 nm. Upon reduction of the metal by one electron to the formally Co<sup>II</sup> compound displays a peak at 273 nm and a shoulder at 369 nm. The peak at 317 nm in the Co<sup>II</sup> spectrum under N<sub>2</sub> is likely from unreduced Co<sup>III</sup>. Finally, upon reduction to Co<sup>I</sup>, a drastic change occurs in the spectrum which now shows an intense band at 521 nm and a smaller one at 678 nm. Under CO<sub>2</sub>, the UV-Visible spectrum appears similar in both the Co<sup>III</sup> and Co<sup>II</sup> states. When the compound is further reduced, it shows a spectrum much more similar to the Co<sup>II</sup> and Co<sup>III</sup> states, suggesting a chemical reaction between the CO<sub>2</sub> and Co<sup>I</sup>, forming what has been called a cobalt(III) “carboxylate,” (Co<sup>III</sup>(CO<sub>2</sub><sup>2-</sup>)), though the term, “metal carboxylate,” generally refers to metal-RCO<sub>2</sub><sup>-</sup> compounds. This and other Co<sup>III</sup>(CO<sub>2</sub><sup>2-</sup>) compounds have been suggested in literature,<sup>18</sup> which is likely the case here. The Co<sup>III</sup>(CO<sub>2</sub><sup>2-</sup>) mentioned is uncommon among this class of Co macrocycle complexes, however it is supported by many spectroscopic techniques including FT-IR, XANES, EXAFS, and flash photolysis.<sup>14,26-31</sup> The unconventional oxidation state assignment tends to be the case mostly with Co macrocycles with trans-diimines with one exception, a monoimine. Studies have shown that the reduced CO<sub>2</sub> is stabilized by hydrogen bonding from the ligand.<sup>31</sup> M(CO<sub>2</sub><sup>2-</sup>) intermediates are invoked in the mechanism for the water-gas shift reaction.<sup>32</sup>

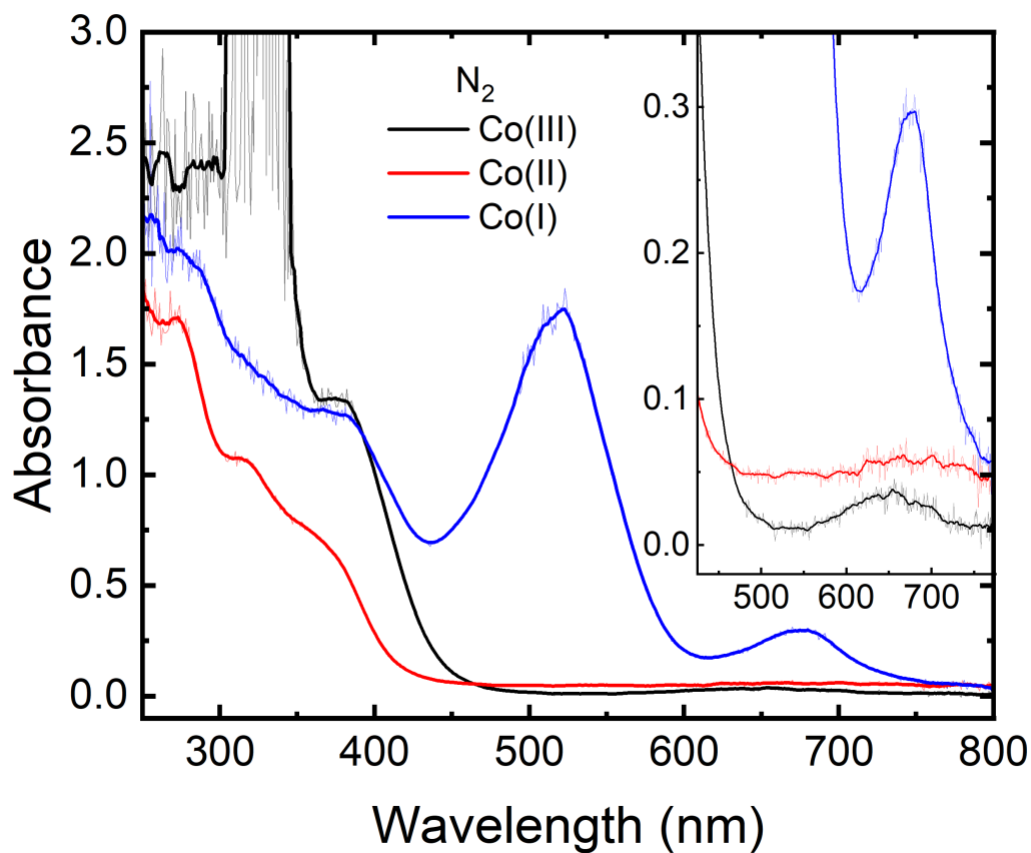


**Figure 2.12:** Spectroelectrochemistry of Co(SIM)Br<sub>2</sub>PF<sub>6</sub> in CH<sub>3</sub>CN under an atmosphere of N<sub>2</sub>. Black: 0.5 V vs. Ag<sup>+/0</sup>. Red: -0.5 V vs. Ag<sup>+/0</sup>. Blue: -1.75 V vs. Ag<sup>+/0</sup>. Light colored lines, raw data. Full colored lines, 10-point adjacent average.



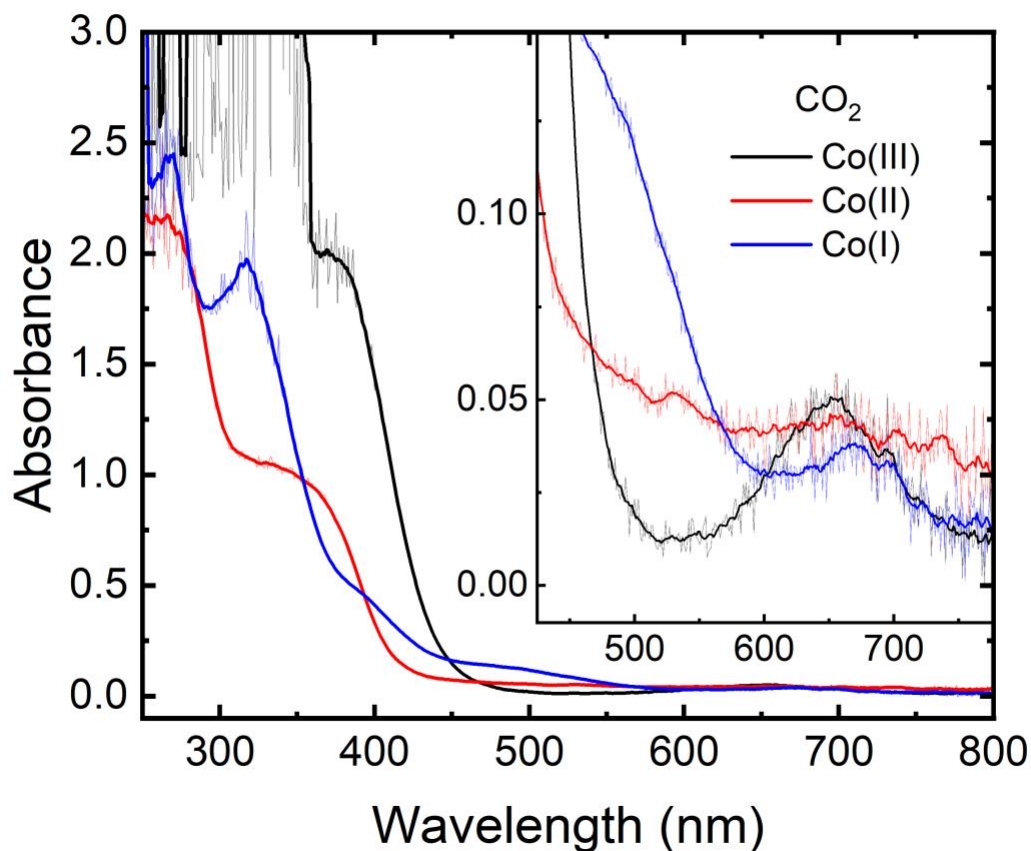


**Figure 2.13:** Spectroelectrochemistry of  $\text{Co}(\text{SIM})\text{Br}_2\text{PF}_6$  in  $\text{CH}_3\text{CN}$  under an atmosphere of  $\text{CO}_2$ . Black: 0.5 V vs.  $\text{Ag}^{+/0}$ . Red:  $-0.5$  V vs.  $\text{Ag}^{+/0}$ . Blue:  $-1.75$  V vs.  $\text{Ag}^{+/0}$ . Light colored lines, raw data. Full colored lines, 10-point adjacent average.

### Attempted Isolation of More Soluble Starting Materials

The solubility of the  $\text{Co}^{\text{III}}$  species has always been of concern ( $<0.065$  mM in THF). While sufficient for standard voltammetric techniques, attempts at spectroelectrochemical analysis have failed due to the low concentration of  $\text{Co}(\text{SIM})\text{Br}_2\text{PF}_6$  in THF.

Reductions of  $\text{Co}(\text{SIM})\text{Br}_2\text{PF}_6$  has been used to generate a more soluble  $\text{Co}(\text{SIM})^n$  species. Attempts have been made to generate both a  $\text{Co}(\text{SIM})^{1+}$  and a  $\text{Co}(\text{SIM})^{2+}$  species. In one experiment,  $\text{Co}(\text{SIM})\text{Br}_2\text{PF}_6$  was treated with 2 equiv. of  $\text{Na}(\text{Hg})$ . During the experiment, the solution went from a pale green suspension of  $\text{Co}(\text{SIM})\text{Br}_2\text{PF}_6$  in 5:1 toluene:THF to brown and then to a deep blue/purple color overnight. From this solution, an orange/violet crystal was

obtained by slow diffusion of pentanes into the reaction mixture. The crystal structure was determined to be of a new cobalt-containing species shown in Figure 2.14. This structure was determined to be a formally Co(II) complex containing a single  $\text{PF}_6^-$  counteranion (removed for clarity). The SIM ligand contains two imines that are trans to each other across the metal center, and two amines that are also trans to each other. In this compound, one of the propylene backbones is oxidized to form a NacNac-like unit while reducing the two imines to single bonds. Overall, five hydrogen atom transfers were required to go from  $\text{Co}^{\text{III}}(\text{SIM})^{3+}$  to the newly formed and compound that we have called  $\text{Co}^{\text{II}}(\text{GIM})^+$ . Three hydrogen atoms were lost, and two were gained, leaving the last equivalent likely leaving as half an equivalent of  $\text{H}_2$ . A similar crystallographically characterized compound was seen with a  $\text{Ni}^{\text{II}}$  center (CSD: BAWKOA).<sup>33,34</sup>

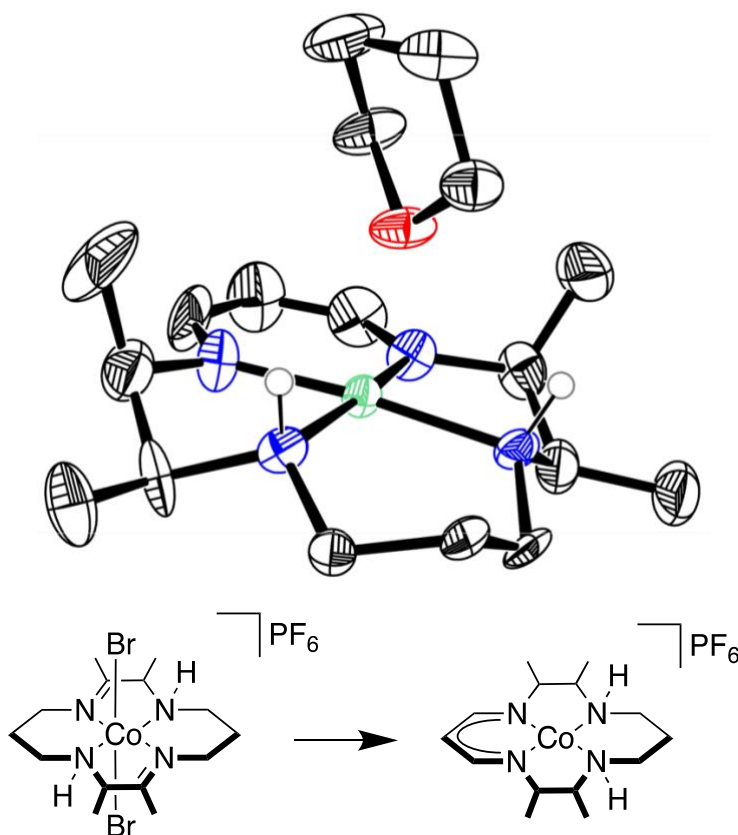


**Figure 2.14:** (Top) Solid state crystal structure of  $\text{Co}^{\text{II}}(\text{GIM})(\text{THF})\text{PF}_6$  and (bottom) drawn structures of  $\text{Co}(\text{SIM})\text{Br}_2\text{PF}_6$  and  $\text{Co}(\text{GIM})\text{PF}_6$ . Hydrogen atoms except amine hydrogens and counteranion omitted for clarity. Probability ellipsoids shown at 50%. Drawn structure of  $\text{Co}(\text{GIM})$  compound is shown with the THF ligand removed for clarity.

Further attempts to generate reduced products have been made, using  $\text{KC}_8$  and  $\text{Na}(\text{Hg})$  as reductants in various solvents and solvent mixtures. All experiments have yielded multiple products. A common trait among most of the reductions seems to be the vacuum instability of the reduced products. In order to probe this vacuum instability, a sample of  $\text{Co}(\text{SIM})\text{Br}_2\text{PF}_6$  was reduced with 1 equivalent of  $\text{KC}_8$  in 2-methyl-THF. Half of the sample was removed, and an EPR spectrum was obtained at 77K. The other half of the sample was held under vacuum for three hours, was redissolved in 2-methyl-THF, and its EPR spectrum was obtained. Both EPR spectra are shown in Figure 2.15. The spectra show axial signals at  $g = 2.3$ , which correspond to  $S = 1/2$  systems. Additional features on the axial spectra could either correspond to cobalt ( $I = 7/2$ ) hyperfine coupling or nitrogen ( $I = 1$ ) superhyperfine coupling, or both. Thus far, the coupling in these spectra have been difficult to deconvolute; however, it does show that the spectrum of the reduced species that was held under vacuum is more axial, suggesting a less symmetric ligand environment around the metal center.

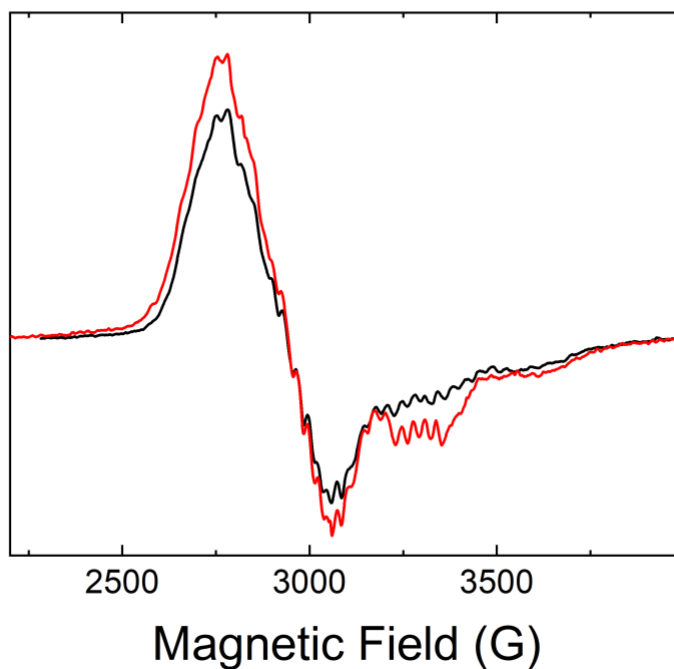


**Figure 2.15:** EPR spectra of  $\text{Co}(\text{SIM})\text{Br}_2\text{PF}_6$  treated with 1 equiv. of  $\text{KC}_8$  in 2-Me-THF (black) and held under vacuum for 3 hours (red)

## *Conclusions and Outlook*

So far, these studies have shown that along with previous literature on similar cobalt macrocycle complexes,  $\text{Co}(\text{SIM})\text{Br}_2\text{PF}_6$  shows initial promise as a catalyst for  $\text{CO}_2$  reduction. The first step,  $\text{CO}_2$  binding, is has been reported to be reversible, but we show that under our conditions, though an equilibrium may exist, the  $\text{CO}_2$  either does not release or releases very slowly after sweeping the reduction potential to more positive potentials. Using our knowledge of the thermodynamics of the system, we treated the cobalt complex under reductive conditions with very weak phosphazine acids to a much stronger acid, pyridinium, and showed a slight increase in reductive current even with the weakest acid. Disappointingly, electrocatalytic studies with these acids never produced more than 0.2 equivalents of CO to Co complex. Further spectroelectrochemical experiments in THF showed the compound was not soluble enough, and in  $\text{CH}_3\text{CN}$ , spectra were nearly identical to published reports.<sup>14</sup> Attempts to reduce the cobalt complex to find more soluble starting materials have resulted in an unexpected product ( $\text{Co}(\text{GIM})(\text{THF})\text{PF}_6$ ), which has not been studied further.

With the sensitivity of these Co macrocycles under reductive conditions, developing a well-supported thermodynamic cycle to predict the reactivity in this system would be very difficult. Similar to other projects in the Yang group, we may be able to study the reactivity of bound  $\text{CO}_2$  under reductive conditions using quinones, which also reversibly bind  $\text{CO}_2$ , giving us a similar starting place. Other nucleophiles,<sup>35,36</sup> including other metal-containing systems<sup>37,38</sup> have been shown to reversibly bind  $\text{CO}_2$  as well. While the outlook on the aims of this project look promising, a system that would facilitate the research has not yet been found.

### *Crystallographic Information for Co(GIM)(THF)PF<sub>6</sub>*

The data for jyy201 were collected from a shock-cooled single crystal at 93(2) K on a Bruker SMART APEX II three-circle diffractometer with a sealed X-ray tube using a equatorial mounted graphite as monochromator and a Bruker Apex II CCD detector. The diffractometer was equipped with a low temperature device and used MoK $\alpha$  radiation ( $\lambda = 0.71073 \text{ \AA}$ ). All data were integrated with SAINT and a multi-scan absorption correction using SADABS was applied.<sup>39,40</sup> The structure was solved by direct methods using SHELXS and refined by full-matrix least-squares methods against  $F^2$  by SHELXL-2018/3 using ShelXle.<sup>41,42</sup> All non-hydrogen atoms were refined with anisotropic displacement parameters. All C-bound hydrogen atoms were refined isotropic on calculated positions using a riding model with their  $U_{\text{iso}}$  values constrained to 1.5 times the  $U_{\text{eq}}$  of their pivot atoms for terminal sp<sup>3</sup> carbon atoms and 1.2 times for all other carbon atoms. Disordered moieties were refined using bond lengths restraints and displacement parameter restraints. This report and the CIF file were generated using FinalCif.<sup>43</sup>

#### Refinement Details:

All non-hydrogen atoms were refined anisotropically. All hydrogen atoms were refined using a riding model. The thermal ellipsoids of split atoms in disordered parts were constrained to the same values. C2, C8, C9, and C10 were restrained to more isotropic thermal ellipsoids, and chemically equivalent bond lengths were restrained to similar values. Poor data quality required truncation of the data at 0.83  $\text{\AA}$ .

**Table 2.5:** Crystal data for Co(GIM)(THF)PF<sub>6</sub>

<b>Empirical formula</b>	<b>C<sub>18</sub>H<sub>35</sub>CoF<sub>6</sub>N<sub>4</sub>OP</b>
<b>Formula weight</b>	527.40
<b>Temperature [K]</b>	93(2)
<b>Crystal system</b>	monoclinic
<b>Space group (number)</b>	<i>P</i> 2 <sub>1</sub> / <i>c</i> (14)
<b><i>a</i> [Å]</b>	8.8616(8)
<b><i>b</i> [Å]</b>	24.350(2)
<b><i>c</i> [Å]</b>	10.7669(9)
<b><math>\alpha</math> [°]</b>	90
<b><math>\beta</math> [°]</b>	98.2053(15)
<b><math>\gamma</math> [°]</b>	90
<b>Volume [Å<sup>3</sup>]</b>	2299.5(3)
<b><i>Z</i></b>	4
<b><math>\rho_{\text{calc}}</math> [gcm<sup>-3</sup>]</b>	1.523
<b><math>\mu</math> [mm<sup>-1</sup>]</b>	0.882
<b><i>F</i>(000)</b>	1100
<b>Crystal size [mm<sup>3</sup>]</b>	0.262×0.187×0.154
<b>Crystal colour</b>	orange
<b>Crystal shape</b>	plate
<b>Radiation</b>	MoK $\alpha$ ( $\lambda$ =0.71073 Å)
<b>2<math>\theta</math> range [°]</b>	3.35 to 50.70 (0.83 Å)
<b>Index ranges</b>	-10 ≤ <i>h</i> ≤ 10 -29 ≤ <i>k</i> ≤ 29 -12 ≤ <i>l</i> ≤ 12
<b>Reflections collected</b>	36514
<b>Independent reflections</b>	4207 <i>R</i> <sub>int</sub> = 0.0810 <i>R</i> <sub>sigma</sub> = 0.0546
<b>Completeness to <math>\theta</math> = 25.349°</b>	100.0 %
<b>Data / Restraints / Parameters</b>	4207/48/324
<b>Goodness-of-fit on <i>F</i><sup>2</sup></b>	1.118
<b>Final <i>R</i> indexes [<i>I</i> ≥ 2<math>\sigma</math>(<i>I</i>)]</b>	<i>R</i> <sub>1</sub> = 0.0716 <i>wR</i> <sub>2</sub> = 0.1333
<b>Final <i>R</i> indexes [all data]</b>	<i>R</i> <sub>1</sub> = 0.1013 <i>wR</i> <sub>2</sub> = 0.1444
<b>Largest peak/hole [eÅ<sup>-3</sup>]</b>	0.63/-0.39

## References

- (1) Can, M.; Armstrong, F. A.; Ragsdale, S. W. Structure, Function, and Mechanism of the Nickel Metalloenzymes, CO Dehydrogenase, and Acetyl-CoA Synthase. *Chemical Reviews* **2014**, *114* (8), 4149–4174. <https://doi.org/10.1021/cr400461p>.
- (2) Wang, V. C.-C.; Ragsdale, S. W.; Armstrong, F. A. Investigations of the Efficient Electrocatalytic Interconversions of Carbon Dioxide and Carbon Monoxide by Nickel-Containing Carbon Monoxide Dehydrogenases. In *The Metal-Driven Biogeochemistry of Gaseous Compounds in the Environment*; Kroneck, P. M. H., Torres, M. E. S., Eds.; Metal Ions in Life Sciences; Springer Netherlands: Dordrecht, 2014; pp 71–97. [https://doi.org/10.1007/978-94-017-9269-1\\_4](https://doi.org/10.1007/978-94-017-9269-1_4).
- (3) Reda, T.; Plugge, C. M.; Abram, N. J.; Hirst, J. Reversible Interconversion of Carbon Dioxide and Formate by an Electroactive Enzyme. *PNAS* **2008**, *105* (31), 10654–10658. <https://doi.org/10.1073/pnas.0801290105>.
- (4) Bassegoda, A.; Madden, C.; Wakerley, D. W.; Reisner, E.; Hirst, J. Reversible Interconversion of CO<sub>2</sub> and Formate by a Molybdenum-Containing Formate Dehydrogenase. *J. Am. Chem. Soc.* **2014**, *136* (44), 15473–15476. <https://doi.org/10.1021/ja508647u>.
- (5) Fourmond, V.; Wiedner, E. S.; Shaw, W. J.; Léger, C. Understanding and Design of Bidirectional and Reversible Catalysts of Multielectron, Multistep Reactions. *J. Am. Chem. Soc.* **2019**, *141* (28), 11269–11285. <https://doi.org/10.1021/jacs.9b04854>.
- (6) Bi, J.; Hou, P.; Kang, P. Single Iridium Pincer Complex for Roundtrip Electrochemical Conversion between Carbon Dioxide and Formate. *ChemCatChem* **2019**, *11* (8), 2069–2072. <https://doi.org/10.1002/cctc.201900083>.
- (7) Cunningham, D. W.; Barlow, J. M.; Velazquez, R. S.; Yang, J. Y. Reversible and Selective CO<sub>2</sub> to HCO<sub>2</sub><sup>-</sup> Electrocatalysis near the Thermodynamic Potential. *Angewandte Chemie*

- International Edition* **2020**, *59* (11), 4443–4447.  
<https://doi.org/10.1002/anie.201913198>.
- (8) Cunningham, D. W.; Yang, J. Y. Kinetic and Mechanistic Analysis of a Synthetic Reversible CO<sub>2</sub>/HCO<sub>2</sub><sup>-</sup> Electrocatalyst. *Chem. Commun.* **2020**, *56* (85), 12965–12968.  
<https://doi.org/10.1039/DoCC05556E>.
- (9) Davis, S. J.; Lewis, N. S.; Shaner, M.; Aggarwal, S.; Arent, D.; Azevedo, I. L.; Benson, S. M.; Bradley, T.; Brouwer, J.; Chiang, Y.-M.; Clack, C. T. M.; Cohen, A.; Doig, S.; Edmonds, J.; Fennell, P.; Field, C. B.; Hannegan, B.; Hodge, B.-M.; Hoffert, M. I.; Ingersoll, E.; Jaramillo, P.; Lackner, K. S.; Mach, K. J.; Mastrandrea, M.; Ogden, J.; Peterson, P. F.; Sanchez, D. L.; Sperling, D.; Stagner, J.; Trancik, J. E.; Yang, C.-J.; Caldeira, K. Net-Zero Emissions Energy Systems. *Science* **2018**, *360* (6396), eaas9793. <https://doi.org/10.1126/science.aas9793>.
- (10) J, B. S. R.; Loganathan, M.; Shantha, M. S. A Review of the Water Gas Shift Reaction Kinetics. *International Journal of Chemical Reactor Engineering* **2010**, *8* (1).  
<https://doi.org/10.2202/1542-6580.2238>.
- (11) Subramani, V.; Sharma, P.; Zhang, L.; Liu, K. Catalytic Steam Reforming Technology for the Production of Hydrogen and Syngas. In *Hydrogen and Syngas Production and Purification Technologies*; John Wiley & Sons, Ltd, 2009; pp 14–126.  
<https://doi.org/10.1002/9780470561256.ch2>.
- (12) Fisher, B. J.; Eisenberg, R. Electrocatalytic Reduction of Carbon Dioxide by Using Macrocycles of Nickel and Cobalt. *Journal of the American Chemical Society* **1980**, *102* (24), 7361–7363. <https://doi.org/10.1021/ja00544a035>.
- (13) Tinnemans, A. H. A.; Koster, T. P. M.; Thewissen, D. H. M. W.; Mackor, A. Tetraaza-Macrocyclic Cobalt(II) and Nickel(II) Complexes as Electron-Transfer Agents in the Photo(Electro)Chemical and Electrochemical Reduction of Carbon Dioxide. *Recueil des Travaux Chimiques des Pays-Bas* **1984**, *103* (10), 288–295.  
<https://doi.org/10.1002/recl.19841031004>.



- (14) Fujita, E.; Creutz, C.; Sutin, N.; Szalda, D. J. Carbon Dioxide Activation by Cobalt(I) Macrocycles: Factors Affecting Carbon Dioxide and Carbon Monoxide Binding. *J. Am. Chem. Soc.* **1991**, *113* (1), 343–353. <https://doi.org/10.1021/ja00001a048>.
- (15) Jackels, S. C.; Farmery, Keith.; Barefield, E. Kent.; Rose, N. J.; Busch, D. H. Tetragonal Cobalt(III) Complexes Containing Tetradentate Macrocyclic Amine Ligands with Different Degrees of Unsaturation. *Inorg. Chem.* **1972**, *11* (12), 2893–2901. <https://doi.org/10.1021/ic50118a008>.
- (16) Tait, A. Martin.; Busch, D. H. Reactions of Coordinated Ligands. Selective Hydrogenation of .Alpha.-Diimine Linkages in Complexes of Cobalt(III) with Macrocyclic Ligands. *Inorg. Chem.* **1977**, *16* (4), 966–968. <https://doi.org/10.1021/ic50170a057>.
- (17) Schmidt, M. H.; Miskelly, G. M.; Lewis, N. S. Effects of Redox Potential, Steric Configuration, Solvent, and Alkali Metal Cations on the Binding of Carbon Dioxide to Cobalt(I) and Nickel(I) Macrocycles. *J. Am. Chem. Soc.* **1990**, *112* (9), 3420–3426. <https://doi.org/10.1021/ja00165a027>.
- (18) Schneider, J.; Jia, H.; Muckerman, J. T.; Fujita, E. Thermodynamics and Kinetics of CO<sub>2</sub>, CO, and H<sup>+</sup> Binding to the Metal Centre of CO<sub>2</sub>reductioncatalysts. *Chem. Soc. Rev.* **2012**, *41* (6), 2036–2051. <https://doi.org/10.1039/C1CS15278E>.
- (19) Tshepelevitsh, S.; Kütt, A.; Lõkov, M.; Kaljurand, I.; Saame, J.; Heering, A.; Plieger, P. G.; Vianello, R.; Leito, I. On the Basicity of Organic Bases in Different Media. *European Journal of Organic Chemistry* **2019**, *2019* (40), 6735–6748. <https://doi.org/10.1002/ejoc.201900956>.
- (20) Kaljurand, I.; Saame, J.; Rodima, T.; Koppel, I.; Koppel, I. A.; Kögel, J. F.; Sundermeyer, J.; Köhn, U.; Coles, M. P.; Leito, I. Experimental Basicities of Phosphazene, Guanidinophosphazene, and Proton Sponge Superbases in the Gas Phase and Solution. *J. Phys. Chem. A* **2016**, *120* (16), 2591–2604. <https://doi.org/10.1021/acs.jpca.6b01552>.

- (21) Fulmer, G. R.; Miller, A. J. M.; Sherden, N. H.; Gottlieb, H. E.; Nudelman, A.; Stoltz, B. M.; Bercaw, J. E.; Goldberg, K. I. NMR Chemical Shifts of Trace Impurities: Common Laboratory Solvents, Organics, and Gases in Deuterated Solvents Relevant to the Organometallic Chemist. *Organometallics* **2010**, *29* (9), 2176–2179. <https://doi.org/10.1021/om100106e>.
- (22) Lovecchio, F. V.; Gore, E. S.; Busch, D. H. Oxidation and Reduction Behavior of Macrocyclic Complexes of Nickel. Electrochemical and Electron Spin Resonance Studies. *J. Am. Chem. Soc.* **1974**, *96* (10), 3109–3118. <https://doi.org/10.1021/ja00817a016>.
- (23) Vaddypally, S.; Tomlinson, W.; O’Sullivan, O. T.; Ding, R.; Van Vliet, M. M.; Wayland, B. B.; Hooper, J. P.; Zdilla, M. J. Activation of C–H, N–H, and O–H Bonds via Proton-Coupled Electron Transfer to a Mn(III) Complex of Redox-Noninnocent Octaazacyclotetradecadiene, a Catenated-Nitrogen Macrocyclic Ligand. *J. Am. Chem. Soc.* **2019**, *141* (14), 5699–5709. <https://doi.org/10.1021/jacs.8b10250>.
- (24) Lorimer, J. W. *CARBON DIOXIDE IN NON-AQUEOUS SOLVENTS AT PRESSURES LESS THAN 200 KPA*; Solubility Data Series; IUPAC: Oxford, UK, 1992; Vol. 50.
- (25) Zanello, P. *Inorganic Electrochemistry*; 2003. <https://doi.org/10.1039/9781847551146>.
- (26) Fujita, E.; van Eldik, R. Effect of Pressure on the Reversible Binding of Acetonitrile to the “Co(I)–CO<sub>2</sub>” Adduct To Form Cobalt(III) Carboxylate. *Inorg. Chem.* **1998**, *37* (2), 360–362. <https://doi.org/10.1021/ic971044k>.
- (27) Fujita, E.; Furenlid, L. R.; Renner, M. W. Direct XANES Evidence for Charge Transfer in Co–CO<sub>2</sub> Complexes. *J. Am. Chem. Soc.* **1997**, *119* (19), 4549–4550. <https://doi.org/10.1021/ja970151a>.
- (28) Creutz, C.; Schwarz, H. A.; Wishart, J. F.; Fujita, E.; Sutin, N. Thermodynamics and Kinetics of Carbon Dioxide Binding to Two Stereoisomers of a Cobalt(I) Macrocycle in Aqueous Solution. *J. Am. Chem. Soc.* **1991**, *113* (9), 3361–3371. <https://doi.org/10.1021/ja00009a022>.

- (29) Ogata, T.; Yanagida, S.; Brunshwig, B. S.; Fujita, E. Mechanistic and Kinetic Studies of Cobalt Macrocycles in a Photochemical CO<sub>2</sub> Reduction System: Evidence of Co-CO<sub>2</sub> Adducts as Intermediates. *J. Am. Chem. Soc.* **1995**, *117* (25), 6708–6716. <https://doi.org/10.1021/ja00130a009>.
- (30) Fujita, Etsuko.; Szalda, D. J.; Creutz, Carol.; Sutin, Norman. Carbon Dioxide Activation: Thermodynamics of Carbon Dioxide Binding and the Involvement of Two Cobalt Centers in the Reduction of Carbon Dioxide by a Cobalt(I) Macrocycle. *J. Am. Chem. Soc.* **1988**, *110* (14), 4870–4871. <https://doi.org/10.1021/ja00222a079>.
- (31) Fujita, E.; Creutz, C.; Sutin, N.; Brunshwig, B. S. Carbon Dioxide Activation by Cobalt Macrocycles: Evidence of Hydrogen Bonding between Bound CO<sub>2</sub> and the Macrocycle in Solution. *Inorg. Chem.* **1993**, *32* (12), 2657–2662. <https://doi.org/10.1021/ic00064a015>.
- (32) Lin, C.-H.; Chen, C.-L.; Wang, J.-H. Mechanistic Studies of Water–Gas-Shift Reaction on Transition Metals. *J. Phys. Chem. C* **2011**, *115* (38), 18582–18588. <https://doi.org/10.1021/jp2034467>.
- (33) He, Y.; Kou, H.-Z.; Zhou, B.-C.; Wang, R.-J.; Li, Y.-D.; Wang, H.-G. *Gaodeng Zuexiao Huaxue Xuebao* **2002**, *23*, 2017.
- (34) He, Y.; Kou, H.-Z.; Zhou, B.-C.; Wang, R.-J.; Li, Y.-D.; Wang, H.-G. CCDC 219027: Experimental Crystal Structure Determination, 2004. <https://doi.org/10.5517/CC7BXDV>.
- (35) Villiers, C.; Dognon, J.-P.; Pollet, R.; Thuéry, P.; Ephritikhine, M. An Isolated CO<sub>2</sub> Adduct of a Nitrogen Base: Crystal and Electronic Structures. *Angewandte Chemie International Edition* **2010**, *49* (20), 3465–3468. <https://doi.org/10.1002/anie.201001035>.
- (36) Buß, F.; Mehlmann, P.; Mück-Lichtenfeld, C.; Bergander, K.; Dielmann, F. Reversible Carbon Dioxide Binding by Simple Lewis Base Adducts with Electron-Rich Phosphines. *J. Am. Chem. Soc.* **2016**, *138* (6), 1840–1843. <https://doi.org/10.1021/jacs.5b13116>.
- (37) Vogt, M.; Nerush, A.; Diskin-Posner, Y.; Ben-David, Y.; Milstein, D. Reversible CO<sub>2</sub> Binding Triggered by Metal–Ligand Cooperation in a Rhenium(I) PNP Pincer-Type

- Complex and the Reaction with Dihydrogen. *Chem. Sci.* **2014**, *5* (5), 2043–2051. <https://doi.org/10.1039/C4SC00130C>.
- (38) Company, A.; Jee, J.-E.; Ribas, X.; Lopez-Valbuena, J. M.; Gómez, L.; Corbella, M.; Llobet, A.; Mahía, J.; Benet-Buchholz, J.; Costas, M.; van Eldik, R. Structural and Kinetic Study of Reversible CO<sub>2</sub> Fixation by Dicopper Macrocyclic Complexes. From Intramolecular Binding to Self-Assembly of Molecular Boxes. *Inorg. Chem.* **2007**, *46* (22), 9098–9110. <https://doi.org/10.1021/ic700692t>.
- (39) Bruker. SAINT.
- (40) Krause, L.; Herbst-Irmer, R.; Sheldrick, G. M.; Stalke, D. Comparison of Silver and Molybdenum Microfocus X-Ray Sources for Single-Crystal Structure Determination. *J Appl Cryst* **2015**, *48* (1), 3–10. <https://doi.org/10.1107/S1600576714022985>.
- (41) Sheldrick, G. A Short History of SHELX. *Acta Crystallographica Section A* **2008**, *64* (1), 112–122. <https://doi.org/doi:10.1107/S0108767307043930>.
- (42) Sheldrick, G. M. Crystal Structure Refinement with SHELXL. *Acta Cryst C* **2015**, *71* (1), 3–8. <https://doi.org/10.1107/S2053229614024218>.
- (43) Kratzert, D. FinalCif. [HTTPS://dkratzert.de/finalcif.html](https://dkratzert.de/finalcif.html).

## Chapter 3: Development of an Electrochemical Catalytic System for the Reduction of CO<sub>2</sub> to Methanol

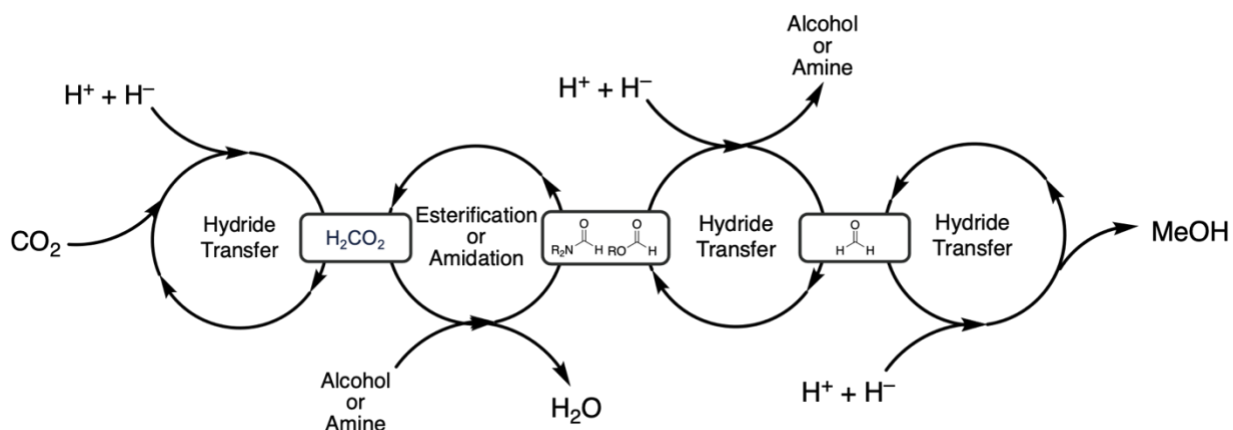
For further discussion on hydricity studies, showing reduction of methyl formate and formadehye, please see Steps Toward CO<sub>2</sub> Reduction to Methanol via Electrochemical Cascade Catalysis by Ian Mercer (MS, UCI, 2020)

### *Introduction*

As the global need for energy continues to increase, the shift to greener energy sources has been partially responsible for an increase in intermittent electricity generation.<sup>1,2</sup> The storage of energy in chemical bonds is an attractive option to store the excess energy when it is produced and use it when generation is lower than demand. For example, the energy density of methanol is 10x greater than that of Li-ion batteries.<sup>3</sup>

The thermodynamics for hydride transfer to CO<sub>2</sub> has been well studied in recent literature.<sup>4-6</sup> The thermodynamics of the hydride transfer reaction has been used in the development of reversible<sup>7</sup> and bidirectional<sup>8</sup> catalysts that are competent for CO<sub>2</sub> reduction and HCO<sub>2</sub><sup>-</sup> oxidation. Sanford and coworkers,<sup>9</sup> and more recently, Goldberg and coworkers<sup>10</sup> reported the first two cascade catalytic systems for the reduction of CO<sub>2</sub> to methanol through a hydrogenation pathway. Their work is a step forward to the development of an effective means of storing electrical energy C-H or C-C bonds. While their work was pivotal, in both cases, the reactions were run at high temperature and pressure, and the best performances were inhibited by the Lewis acid catalyst responsible for esterification of formic acid. In this work, we aim to develop an electrochemical cascade catalytic system using the thermodynamics of each elementary step as a guide. A proposed cascade catalytic cycle is shown in Scheme **3.1** where: (1) CO<sub>2</sub> undergoes reduction and protonation to formic acid, (2) esterification or amidation of the

formic acid to yield an ester or amide, respectively, (3) followed by two hydride transfers and protonations, ending with the release of methanol.



**Scheme 3.1:** Proposed electrochemical cascade catalytic process

In order to reduce  $\text{CO}_2$  to  $\text{HCO}_2^-$ , the hydride donor must have a hydricity value equal to or less than those shown in Table 3.1 in various solvents. The reaction for the formation of a hydride from formate, forming  $\text{CO}_2$  and a hydride is shown in Equation 1. A difficulty that arises under catalytic conditions is the propensity for the hydride to be protonated and released as  $\text{H}_2$  gas. The heterolytic cleavage of  $\text{H}_2$  is shown in Equation 2, and the associated solvent- and pH-dependent free energy changes are shown in Table 3.1. Importantly, in this thermodynamics-driven method, the free energy change of formate production must be more negative than the free energy change of  $\text{H}_2$  evolution under the given conditions.

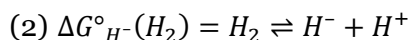
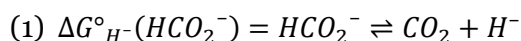


**Table 3.1:** Relevant solvent-dependent empirically determined constants

Solvent	$\Delta G_{H^-}^{\circ}(\text{HCO}_2^-)$ (kcal/mol)	$\Delta G_{H^-}^{\circ}(\text{H}_2)$ (kcal/mol) <sup>4</sup>
<i>H</i> <sub>2</sub> <i>O</i>	24.1 <sup>11</sup>	34.2
<i>CH</i> <sub>3</sub> <i>CN</i>	44 <sup>12</sup>	76.0
<i>DMSO</i>	42 <sup>13,14</sup>	60.7
<i>THF</i>	>44.7 <sup>15</sup>	68.7

Applying these thermodynamic considerations to a cascade catalytic system and flattening the energy landscape to make it as energetically efficient as possible, we must first consider each elementary step, keeping in mind that each step in a one-pot cascade must be compatible with every other step. Here, I present experiments on the esterification and amidation of a formate salt and formic acid.

## *Experimental Methods*

### General Considerations

All manipulations with formic acid were carried out in open air. All experiments with  ${}^n\text{Bu}_4\text{N HCO}_2$  were prepared in an inert atmosphere glovebox and subsequently left to react in either a J. Young-type NMR tube or a parafilm-sealed NMR tube with standard cap. All deuterated solvents were dried over 3Å molecular sieves or  $\text{CaH}_2$ , distilled, and stored over 3Å molecular sieves.  ${}^n\text{Bu}_4\text{N HCO}_2$  was prepared by mixing equimolar quantities of fresh  ${}^n\text{Bu}_4\text{N OH}$  and 88% formic acid in methanol and removing the solvent *in vacuo*. All amine acids were prepared by the addition of the conjugate acids ( $\text{HOTf}$  and  $\text{HBF}_4 \cdot \text{Et}_2\text{O}$ ) to the amines dissolved in dry  $\text{Et}_2\text{O}$ . The resulting solids were filtered in air and dried *in vacuo*. Propylamine, dipropylamine, and 4-fluoroaniline were distilled prior to use. All other chemicals and reagents were used as received from the manufacturer. All temperatures are reported in °C.

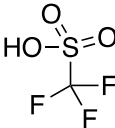
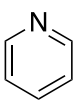
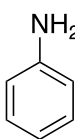
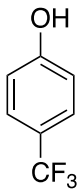
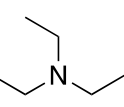
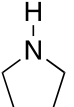
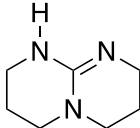
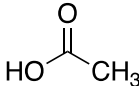
### NMR Experiments

NMR spectra were collected on a Bruker Avance 600 MHz with a cryoprobe. Conversion percentages were calculated according to the following formula:

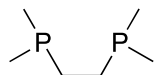
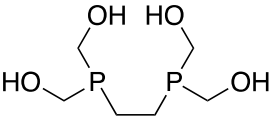
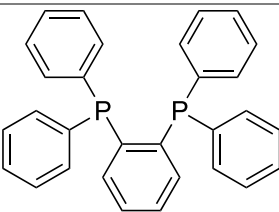
$$\% \text{ Conversion} = \frac{\text{Product Integration}}{\text{Product Integration} + \text{Starting Material Integration}}$$

The calculated % conversions should be considered as the best case, however, in all cases presented here, there was little ambiguity in the identity of the resulting products, ethyl formate,<sup>16</sup> 4-fluoroformanilide,<sup>17</sup> di- ${}^n$ butylformamide,<sup>18</sup> and  ${}^n$ butyl formate.<sup>19</sup>

**Table 3.2:** Relevant  $pK_a$  values

Structure								
Abbreviation	<b>HOTf</b> <sup>20</sup>	<b>Py</b> <sup>21</sup>	<b>Aniline</b> <sup>21</sup>	<b>4-CF<sub>3</sub>-Phenol</b> <sup>22</sup>	<b>Et<sub>3</sub>N</b> <sup>21</sup>	<b>Pyrr</b> <sup>21</sup>	<b>TBD</b> <sup>21</sup>	<b>AcOH</b> <sup>20</sup>
$pK_a$ THF	7.83	5.5	5.2	---	12.5	13.5	21.0	22.48
$pK_a$ CH <sub>3</sub> CN	2.60	12.53	10.64	26.5	18.83	19.62	26.02	23.51

**Table 3.3:** Diphosphine ligand abbreviations

Structure			
Abbreviation	dmpe	dhmpe	dppbz

## Results and Discussion

### Esterification and Amidation of HCO<sub>2</sub><sup>-</sup>

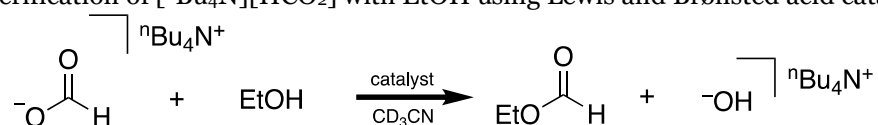
Initial studies focused on the conversion of formate salts into formate esters and formamides. Previous reports have demonstrated esterification of acetic acid with Brønsted acids<sup>23</sup> and Lewis acids.<sup>24</sup> Additionally, in previous CO<sub>2</sub> hydrogenation reports, Sc(OTf)<sub>3</sub> (-OTf = trifluoromethanesulfonate) was used as a catalyst for the esterification of the resulting formic acid product to a methyl<sup>9</sup> or ethyl<sup>10</sup> ester. We decided to begin our attempts with Lewis acid catalyzed esterifications, and the results are summarized in Table 3.4. In each sample, after monitoring the reaction at room temperature for 15 hours in CD<sub>3</sub>CN for any reactivity through <sup>1</sup>H-NMR, the sample was then heated for the reported time. In reports where the acetic acid (HOAc) was esterified using a Sc(OTf)<sub>3</sub> catalyst, the worst conversion in the presence of catalyst was 71% in 30 minutes in refluxing HOAc.<sup>24</sup> Using tetra-*n*-butylammonium formate (<sup>n</sup>Bu<sub>4</sub>N HCO<sub>2</sub>) as the electrophile, there is essentially no reactivity at room temperature and very little reactivity even



at 70°C for 27 hr. Considering the possibility that conversion to the formate ester may require a small equilibrium of protonated formate, a weak Brønsted acid, 4-CF<sub>3</sub>-phenol, was added to the reaction mixtures (Entries 3 and 5) with small differences in conversion. In all of the examples labeled with <1% conversion, resonances belonging to the ethyl formate product were observed in the <sup>1</sup>H NMR, but any quantitation below 1% may be severely affected by dissimilarities in the baselines imposed on the spectrum. In entries labeled with 0%, no resonances attributable to the product were observed.

Comparing Entries 2 and 5, under very similar conditions, some product is observed in the former with none in the latter. The inconsistency may be due to a small amount of water present in one of the samples, but in both cases, the total conversion is extremely small.

**Table 3.4:** Esterification of [<sup>n</sup>Bu<sub>4</sub>N][HCO<sub>2</sub>] with EtOH using Lewis and Brønsted acid catalysts



Entry	Catalyst (mol%)	Time	Temperature	Conversion
1	Dy(OTf) <sub>3</sub> (5%)	30 hr.	65	0%
2	Sc(OTf) <sub>3</sub> (5%)	27 hr.	70	<1%
3	Sc(OTf) <sub>3</sub> (5%) 4-CF <sub>3</sub> -Phenol (2.5%)	27 hr.	70	<1%
4	Al(OTf) <sub>3</sub> (10%)	27 hr.	70	<1%
5	Al(OTf) <sub>3</sub> (10%) 4-CF <sub>3</sub> -Phenol (2.5%)	27 hr.	70	<1%
6	Sc(OTf) <sub>3</sub> (5%)	30 hr.	75	0%

Even without any reactivity seen, the Sc<sup>3+</sup>, Al<sup>3+</sup>, and Dy<sup>3+</sup> salts do appear to interact with formate in solution (Figure 3.1). Compared to free <sup>n</sup>Bu<sub>4</sub>N HCO<sub>2</sub>, which has a formyl proton resonance at 8.72 ppm, the interaction with Sc<sup>3+</sup> yields two new resonances at 8.69 and 8.50 ppm that integrate in a 2:1 ratio. For the Al<sup>3+</sup> salt, the formyl proton resonance shifts to 8.62 ppm with a broad resonance likely consisting of multiple species at 8.26 ppm. Addition of the paramagnetic Dy<sup>3+</sup> salt yields only one broad formyl proton signal that is centered at 8.68 ppm.

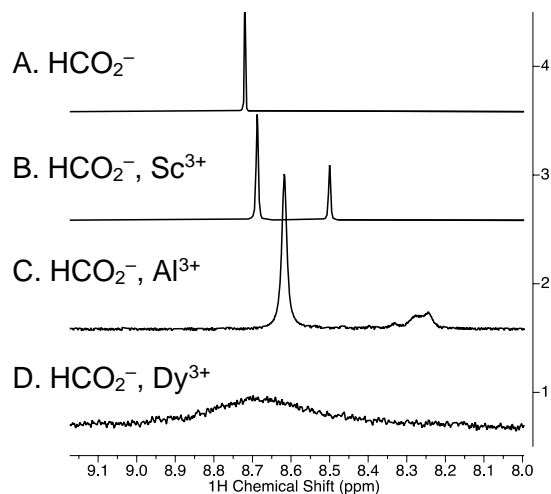


**Figure 3.1:**  $^1\text{H}$ -NMR spectra of the formyl proton of tetra-*n*-butylammonium formate in  $\text{CD}_3\text{CN}$  (Top), with 5 mol%  $\text{Sc}(\text{OTf})_3$  (middle), and 10 mol%  $\text{Al}(\text{OTf})_3$  (bottom)

Entries 2-5 were monitored intermittently over another 12 days, and even after 13 total days at  $70^\circ\text{C}$ , there was very little conversion to the formate product. In Entry 2b, there was essentially no change in the  $^1\text{H}$  NMR spectrum between the measurement at 27 hr and 13 days.

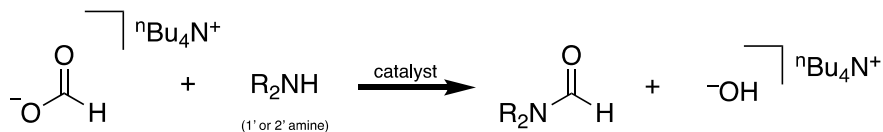
**Table 3.5:** Effect of heating reaction mixtures for 2 weeks

Entry	Catalyst (mol%)	Time	Temperature	Conversion
<b>2b</b>	$\text{Sc}(\text{OTf})_3$ (5%)	13 days	70	<1%
<b>3b</b>	$\text{Sc}(\text{OTf})_3$ (5%) 4- $\text{CF}_3$ -Phenol (2.5%)	13 days	70	2.6%
<b>4b</b>	$\text{Al}(\text{OTf})_3$ (10%)	13 days	70	1.8%
<b>5b</b>	$\text{Al}(\text{OTf})_3$ (10%) 4- $\text{CF}_3$ -Phenol (2.5%)	13 days	70	1.1%

Seeing very little conversion in the previous reactions, we considered that ethanol (or possibly the conjugate base ethoxide) was too weak of a nucleophile to add in to the carbonyl carbon. As such, we chose two liquid amines to pursue further reactivity. Tertiary amines were excluded from these studies because of the necessity for deprotonation of the amine to form the secondary or tertiary formamide. Primary amine propylamine ( $\text{PrNH}_2$ ) and secondary amine dipropylamine ( $\text{Pr}_2\text{NH}$ ) were selected as they are both liquids and have identical R groups. Under similar conditions as with ethanol, the formate salt was treated with the amines, and the results

are summarized in Table 3.6. Similar to before, over a shorter amount of time, no reactivity was seen with no visible change in the  $^1\text{H-NMR}$  spectrum.

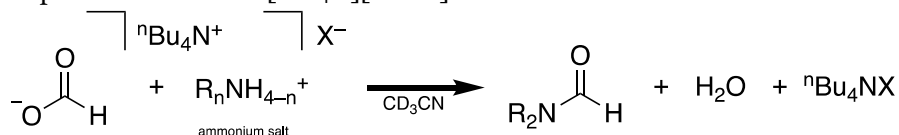
**Table 3.6:** Attempted amidations of [ $^n\text{Bu}_4\text{N}$ ][ $\text{HCO}_2$ ] with dipropylamine and propylamine using Lewis acid catalysts



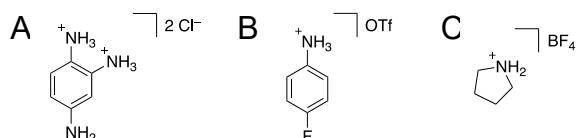
Entry	Substrate	Catalyst	Solvent	Time	Temperature	Conversion
7	Pr <sub>2</sub> NH	Dy(OTf) <sub>3</sub>	CD <sub>3</sub> CN	30 hr	75	0%
8	PrNH <sub>2</sub>	Dy(OTf) <sub>3</sub>	CD <sub>3</sub> CN	30 hr.	75	0%
9	Pr <sub>2</sub> NH	Sc(OTf) <sub>3</sub>	CD <sub>3</sub> CN	30 hr.	75	0%
10	PrNH <sub>2</sub>	Sc(OTf) <sub>3</sub>	CD <sub>3</sub> CN	30 hr.	75	0%
11	Pr <sub>2</sub> NH	3Å Sieves	Toluene	23 hr.	80 <sup>a</sup>	0%

<sup>a</sup>Entry 11 was allowed to react at room temperature for 20 hours, then heated to 60°C for 26 hours, then heated to 80°C for 23 hours.

As the amine nucleophile did not react with formate as desired, we next considered the protonation state of formate itself. In all of the acetic acid studies reported,<sup>24</sup> the reaction was completed on the protonated form. With the release of the final formamide, instead of an unstabilized hydroxide ion, water and a tetrabutylammonium salt is formed. Table 3.7 shows a summary of the reaction of various acid salts with  $^n\text{Bu}_4\text{N HCO}_2$ . Using  $\text{NH}_4\text{PF}_6$  to first protonate, then perform nucleophilic addition into the formate carbonyl bond, was problematic at the start. Although  $\text{NH}_4^+$  has a  $\text{p}K_a$  of 16.46 in  $\text{CH}_3\text{CN}$ <sup>21</sup> and  $\text{H}_2\text{CO}_2$  has a  $\text{p}K_a$  estimated at 20.9,<sup>25</sup> addition of  $\text{NH}_4^+$  to  $\text{H}_2\text{CO}_2$  results in precipitation of the salt  $\text{NH}_4\text{HCO}_2$ . Using 4-fluoroaniline • HOTf and pyrrolidine • HOTf, at least partial protonation of formate to formic acid is seen in the  $^1\text{H-NMR}$  by an up-field shift of the formyl proton resonance consistent with the shift seen between  $^n\text{Bu}_4\text{N HCO}_2$  and  $\text{H}_2\text{CO}_2$  in  $\text{CD}_3\text{CN}$ , but no reactivity is observed with the stronger acid. However, in the presence of pyrrolidinium, Entry 15, there was 3% conversion of formate to N-formylpyrrolidine. A potential explanation for the inconsistency is that the two aniline conjugate bases are less nucleophilic than pyrrolidine.

**Table 3.7:** Attempted amidations of [<sup>n</sup>Bu<sub>4</sub>N][HCO<sub>2</sub>] with ammonium salts

Entry	Substrate	Time	Temperature	Conversion
<b>12</b>	NH <sub>4</sub> PF <sub>6</sub>	45 hr	25	0%
<b>13</b>	A	45 hr.	25	0%
<b>14</b>	B	45 hr.	25	0%
<b>15</b>	C	45 hr.	25	3%

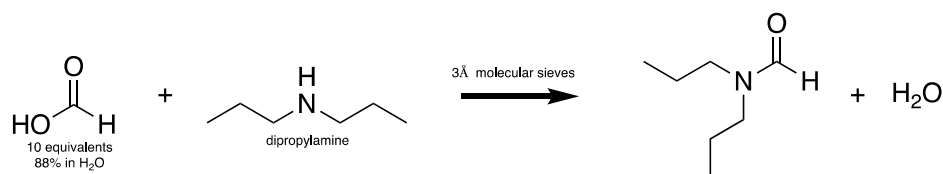


With the aim of developing a catalytic system that functions at room temperature with reasonable turnover frequencies that may be applicable for industrial application ( $10^{-2}$  -  $10^2$  s<sup>-1</sup>),<sup>26</sup> the evidence that the protonation state of formate may be a limiting factor. Instead of using formate salts, formic acid (88% in H<sub>2</sub>O, 10 equivalents with respect to nucleophile) was used for further esterification experiments to see if we could observe the desired reactivity. Additionally, water is present in the formic acid solution and is formed in the balanced reaction. To maximize the ability to exclude water from the reaction, considering a possible equilibrium between formic acid and the formamide/formate ester product, drying agents were employed in the toluene solvent. Ultimately, a 10-fold excess of formic acid was used in the reported esterification using Lewis acid catalysts used acetic acid as the solvent as well as the substrate.<sup>24</sup>

The results of the initial experiments (Table **3.8**, Entries 16-18) were highly encouraging, showing a massive increase in product formation compared to the reactions with formate salts. In the presence of 3Å molecular sieves, over a day, Pr<sub>2</sub>NH reacted with formic acid in refluxing toluene to form *N,N*-dipropylformamide with 28% conversion. Entries 16 and 17 were subjected to the same conditions simultaneously where first, they were left to react for 20 hr at room temperature (Entries 17a-19a), followed by heating to 60°C for 27 hrs (Entries 17b-19b), and

finally heated to 80°C and monitored over 4 days (Entries 17c-19c and 17d-19d). The time represents time spent at the given temperature, and the conversion represents the total conversion up to that point. Toluene appears to be the best solvent between the two conditions because an overall a higher conversion percentage was achieved, and the conversion at 60°C was 29% compared to 5% in CH<sub>3</sub>CN. When under the same conditions as Entries 17 and 18, but *without* Sc(OTf)<sub>3</sub>, conversion occurred slightly slower than with Sc(OTf)<sub>3</sub> present at 60°C. Surprisingly, without the Lewis acid, the total conversion after 96 hr at 80°C was 97% (Entry 19b), leaving very little free amine left in solution.

**Table 3.8:** Amidations of formic acid with dipropylamine using Sc(OTf)<sub>3</sub>



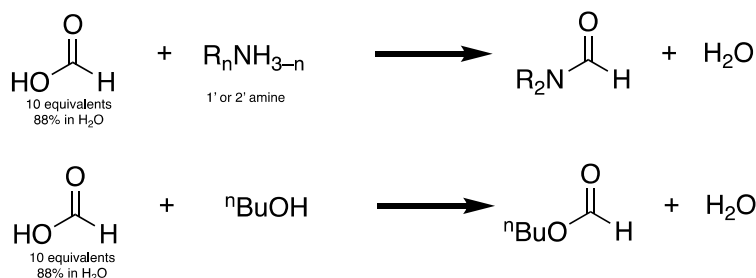
	Conditions	Solvent	Time	Temperature	Conversion
<b>16</b>	Sc(OTf) <sub>3</sub>	Toluene	23 hr.	Reflux	28%
<b>17a</b>	Sc(OTf) <sub>3</sub>	Toluene			1%
<b>18a</b>	Sc(OTf) <sub>3</sub>	CH <sub>3</sub> CN	20 hr.	25°C	<1%
<b>19a</b>	---	Toluene			<1%
<b>17b</b>	Sc(OTf) <sub>3</sub>	Toluene			29%
<b>18b</b>	Sc(OTf) <sub>3</sub>	CH <sub>3</sub> CN	27 hr.	60°C	5%
<b>19b</b>	---	Toluene			19%
<b>17c</b>	Sc(OTf) <sub>3</sub>	Toluene			59%
<b>18c</b>	Sc(OTf) <sub>3</sub>	CH <sub>3</sub> CN	22 hr.	80°C	21%
<b>19c</b>	---	Toluene			78%
<b>17d</b>	Sc(OTf) <sub>3</sub>	Toluene			66%
<b>18d</b>	Sc(OTf) <sub>3</sub>	CH <sub>3</sub> CN	74 hr.	80°C	55%
<b>19d</b>	---	Toluene			97%

Under the impression that water had a deleterious effect on the N-formylation or esterification reaction, drying agents MgSO<sub>4</sub> and KHSO<sub>4</sub> were also considered, both of which can act as Lewis acids, and KHSO<sub>4</sub>, which may act as both a Brønsted and Lewis acid (pK<sub>a</sub> HSO<sub>4</sub><sup>-</sup> (H<sub>2</sub>O) = 2.0).<sup>27</sup> With the change in drying agents, compared to Entry 19d with molecular sieves,

the sample with MgSO<sub>4</sub> (Entry 20) showed a drop in conversion. When no drying agent was added (Entry 22), only a slight drop in conversion was noted over a similar amount of time at similar temperatures compared with molecular sieves as a drying agent (Entry 19d). When KHSO<sub>4</sub> (Entry 21) was added, reactivity entirely shut down which may be due to the very acidic HSO<sub>4</sub><sup>-</sup> ion protonating the amine.

Counter to what was previously believed, when n-butanol, a weaker nucleophile, is used in the described reaction conditions, the conversion to n-butylformate occurs in 88% yield, comparable to dipropylamine. The success of the n-butanol formylation led us to attempt a reaction with a less-nucleophilic amine, 4-fluoroaniline. Entry 24 has a greater than 99% conversion over the course of 15 hours in refluxing toluene, which was by far the best conversion seen thus far.

**Table 3.9:** Amidations and esterification of formic acid in the presence of drying agents



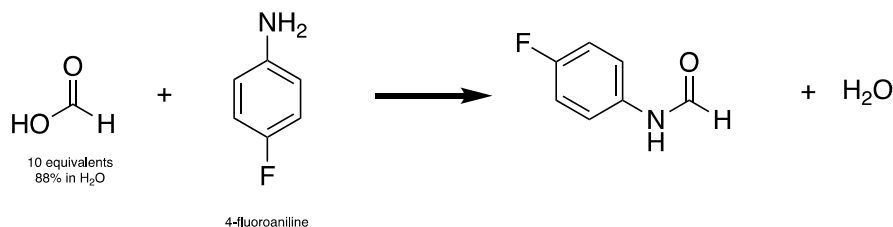
Entry	Substrate	Drying Agent	Solvent	Time	Temp.	Conversion
<b>20</b>	Pr <sub>2</sub> NH	MgSO <sub>4</sub>	Toluene	135 hr.	85	79%
<b>21</b>	Pr <sub>2</sub> NH	KHSO <sub>4</sub>	Toluene	135 hr.	85	<1%
<b>22</b>	Pr <sub>2</sub> NH	---	Toluene	135 hr.	85	89%
<b>23</b>	<sup>n</sup> Bu-OH	3Å Sieves	Toluene	135 hr.	85	88%
<b>24</b>	4-fluoroaniline	---	Toluene	15 hr.	Reflux	>99%

Note: For all samples, 100 μL aliquots were removed from the stirring reaction and added to ~700 μL of CD<sub>3</sub>CN for NMR analysis.

With a major increase in the reactivity, 4-fluoroaniline was selected for further studies. 4-fluoroaniline was specifically selected because it has a diagnostic <sup>19</sup>F-NMR spectrum with a triplet of triplets (J<sub>F-H</sub> = 8.9 Hz, 4.6 Hz) at -131.14 ppm in CD<sub>3</sub>CN where the <sup>1</sup>H NMR for aniline and any formylated aniline is complicated by multiple heavily coupled resonances in the aromatic region.

We performed a solvent screen with solvents that are compatible with electrochemical analysis. The results of the solvent screen are summarized in Table 3.10. Formic acid (10 equivalents) was added to 1 equivalent of 4-fluoroaniline in various solvents, and the reactions were monitored by  $^{19}\text{F}$ -NMR. Interestingly, the  $^{19}\text{F}$ -NMR for the product, 4-fluoroformanilide, appears as two distinct resonances for each rotamer, similar to other formamides.<sup>28</sup> After 15 hours,  $\text{CH}_3\text{CN}$  ( $\epsilon = 36.64$ )<sup>29</sup> and  $\text{CH}_3\text{OH}$  ( $\epsilon = 33.0$ )<sup>29</sup> had similar conversion yields of 78% and 76%, respectively. Use of the more non-polar solvent,  $\text{CH}_2\text{Cl}_2$  ( $\epsilon = 8.93$ )<sup>29</sup> resulted in an increase in the conversion, and THF ( $\epsilon = 7.52$ )<sup>29</sup> had the highest conversion with over 99%. Although a decrease in rate is to be expected when the concentration of one of the reagents is lowered, when the equivalents of formic acid is brought down to 1.3:1 (Entry 30), the conversion significantly slows to 87% over 48 hours. When a 1:1 sample is prepared (Entry 31), the reaction significantly slows again to only 3.6% conversion after 48 hours.

**Table 3.10:** Solvent screen and ratio dependence for the amidation of formic acid with 4-fluoroaniline



Entry	Ratio	Solvent	Time	Conversion
<b>25</b>	10:1	THF	2 hr.	68%
<b>26</b>	10:1	$\text{CH}_3\text{OH}$	15 hr.	78%
<b>27</b>	10:1	$\text{CH}_3\text{CN}$	15 hr.	76%
<b>28</b>	10:1	$\text{CH}_2\text{Cl}_2$	15 hr.	87%
<b>29</b>	10:1	THF	15 hr.	>99%
<b>30</b>	1.3:1	THF	48 hr.	87%
<b>31</b>	1:1	THF	48 hr.	3.6%

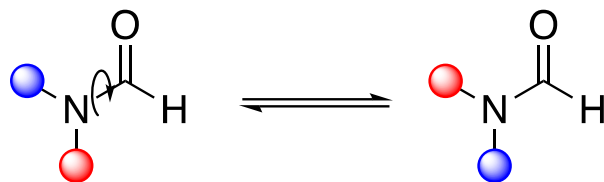


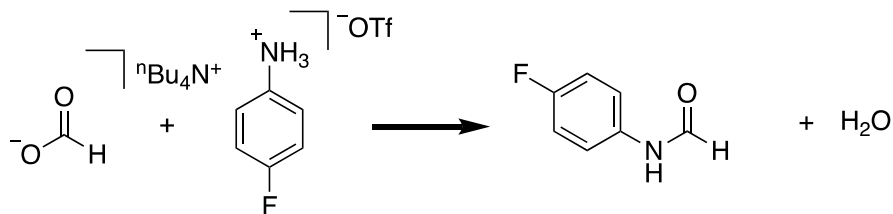
**Figure 3.2:** Two rotamers of a generic formamide.  $\Delta G^\ddagger \approx 21 \text{ kcal/mol}$  for dimethylformamide.<sup>13</sup>

As THF is the best solvent tested for facilitating the reactivity between formic acid and 4-fluoroaniline, we sought to achieve the same reactivity with their conjugate base and conjugate acid, respectively. By achieving the reactivity with the conjugates, we could show that adding an exogenous acid source of a known  $pK_a$ , we may be able to design a system where the  $pK_a$  of the exogenous acid is not sufficient to protonate the metal hydride, leading to deleterious  $H_2$  evolution. This exogenous acid may, however, maintain a small equilibrium of  $H_2CO_2$ , allowing for amidation.

Attempting the amidation reaction between  $[nBu_4N][HCO_2]$  and 4-fluoroaniline • HOTf, the reaction was expected to proceed as before with formic acid and 4-fluoroaniline. Surprisingly, as summarized in Table 3.11, very little reactivity was achieved in any of the reactions, which were all performed at room temperature. In varying the ratios of formate to anilinium, we attempted to recreate similar conditions to the previous studies to no avail. Adding 10 equivalents of water to the reaction mixture also showed no discernable conversion to the formanilide product. The only instances where some conversion to the amidated product occurred when an extra equivalent of acid was added to the solution, and the conversion to 1.5% occurred over 5 days rather than 15 hours to completion as before.



**Table 3.11:** Attempted amidations of [<sup>n</sup>Bu<sub>4</sub>N][HCO<sub>2</sub>] with 4-fluoroanilinium triflate by varying ratios and adding Brønsted acids

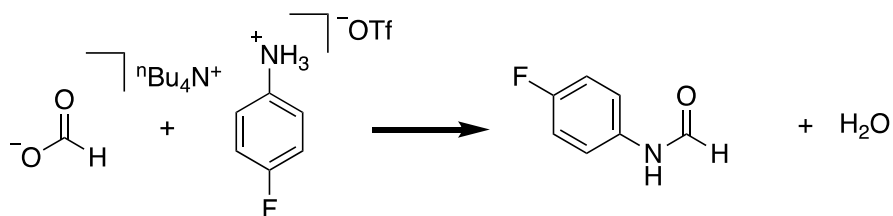


Ratio            m            :

Entry	Ratio (m:n)	Additive	Time	Conversion
<b>32</b>	1:1	---	40 hr.	0%
<b>33</b>	10:1	---	40 hr.	0%
<b>34</b>	1:10	---	40 hr.	0%
<b>35</b>	10:1	H <sub>2</sub> O	40 hr.	0%
<b>36</b>	1:10	H <sub>2</sub> O	40 hr.	0%
<b>37</b>	1:1	Py • HOTf	126 hr.	1.4%
<b>38</b>	1:1	Et <sub>3</sub> N • HBF <sub>4</sub>	126 hr.	1.1%
<b>39</b>	1:1	TBD • HOTf	126 hr.	0%

Again, considering that the solvent may have a negative effect on the conversion, the formate and anilinium salt reactions were tested in 5 different solvents. The only solvent to show a very small amount of conversion was the sample in toluene-*d*<sub>8</sub> with a trace amount of formanilide product detected by <sup>19</sup>F NMR.

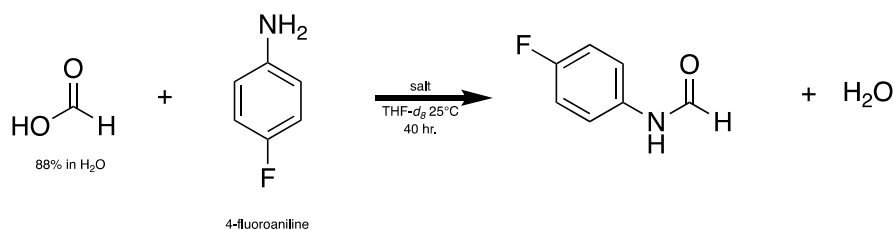
**Table 3.12:** Solvent screen for the attempted amidation of [<sup>n</sup>Bu<sub>4</sub>N][HCO<sub>2</sub>] with 4-fluoroanilinium triflate



Entry	Solvent	Conversion	Time
<b>40</b>	CD <sub>3</sub> CN	0%	25 hr.
<b>41</b>	CD <sub>3</sub> OD	0%	25 hr.
<b>42</b>	D <sub>2</sub> O	0%	25 hr.
<b>43</b>	(CD <sub>3</sub> ) <sub>2</sub> SO	0%	25 hr.
<b>44</b>	Toluene- <i>d</i> <sub>8</sub>	<1%	25 hr.

With the solvent, presence of water, presence of excess acid, excess formate salt, and excess anilinium salt, ruled out as major contributing factors to the reactivity, the final consideration was the salt that was used as the countercation or counteranion for the formate and anilinium, respectively. In all of the prior experiments, a tetra-*n*-butylammonium and triflate salts were used. Known to have a deleterious effect on the reactivity as well, a 1:1 ratio of formic acid to aniline was used in order to determine if we could completely stop reactivity in any case. Over the course of 40 hours at room temperature, low yields were seen across the board with [<sup>n</sup>Bu<sub>4</sub>N][OTf] having the lowest conversion of 2.4% and Li(OTf) having the highest conversion at this point of 6.4%, which is just over 2σ above the average.

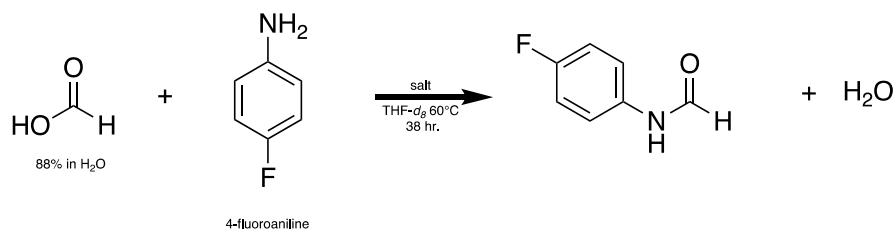
**Table 3.13:** Effect of salts on the amidation of formic acid and 4-fluoroaniline



Entry	Salt	Conversion
<b>45</b>	<sup>n</sup> Bu <sub>4</sub> N OTf	2.4%
<b>46</b>	<sup>n</sup> Bu <sub>4</sub> N BF <sub>4</sub>	5.6%
<b>47</b>	<sup>n</sup> Bu <sub>4</sub> N PF <sub>6</sub>	4.7%
<b>48</b>	<sup>n</sup> Bu <sub>4</sub> N ClO <sub>4</sub>	3.0%
<b>49*</b>	<sup>n</sup> Bu <sub>4</sub> N I	3.6%
<b>50*</b>	(CH <sub>3</sub> ) <sub>4</sub> N Cl	3.4%
<b>51</b>	Li OTf	6.4%
<b>52*</b>	Na BF <sub>4</sub>	3.4%
<b>53*</b>	Na OTf	3.5%
<b>54</b>	---	3.7%

\*Salts did not completely dissolve in these samples

With the low conversion yields after 40 hours, each of the reactions were heated to 60°C for 38 hours. The results are summarized in Table 3.14. After heating, appreciable conversion yields occurred in all of the samples.

**Table 3.14:** Effect of heating amidation reactions with salts

Entry	Salt	Conversion
<b>45b</b>	<sup>n</sup> Bu <sub>4</sub> N OTf	16%
<b>46b</b>	<sup>n</sup> Bu <sub>4</sub> N BF <sub>4</sub>	33%
<b>47b</b>	<sup>n</sup> Bu <sub>4</sub> N PF <sub>6</sub>	28%
<b>48b</b>	<sup>n</sup> Bu <sub>4</sub> N ClO <sub>4</sub>	26%
<b>49b*</b>	<sup>n</sup> Bu <sub>4</sub> N I	26%
<b>50b*</b>	(CH <sub>3</sub> ) <sub>4</sub> N Cl	30%
<b>51b</b>	Li OTf	35%
<b>52b*</b>	Na BF <sub>4</sub>	28%
<b>53b*</b>	Na OTf	28%
<b>54b</b>	---	28%

\*Salts did not completely dissolve in these samples

Figure 3.3 contains the compiled data from the addition of various salts to the reaction mixture of 4-fluoroaniline and formic acid. Most of the salts yielded very similar conversions, but notably, [<sup>n</sup>Bu<sub>4</sub>N][OTf] had the lowest total conversion with 16%. The next lowest conversion was 26%, a 60% increase in conversion. In part, these data explain the inhibition of the reactivity of formic acid with the 4-fluoroaniline, however it is not immediately clear why, if LiOTf had the best conversion among the 9 added salts, and there was essentially no difference in the conversion with other <sup>n</sup>Bu<sub>4</sub>N<sup>+</sup> cations. With the differences in the cations and anions, I expect the reason [<sup>n</sup>Bu<sub>4</sub>N][OTf] has the lowest conversion because it is the only source of “free” triflate ion. Schumann and coworkers<sup>30</sup> reported a crystallographically characterized (Li<sub>2</sub>(OTf)<sub>2</sub>(THF)<sub>2</sub>)<sub>n</sub> polymeric structure, and Anwender and coworkers<sup>31</sup> similarly reported a Li<sub>4</sub>(OTf)<sub>4</sub>(THF)<sub>6</sub> monomer. These structures, NaOTf’s low solubility, and knowing ion pairing to be very favorable in non-polar THF suggest that the major difference between the three triflate salts is whether the cation is expected to stay tightly bound when in THF solution. Frech and Huang<sup>32</sup> showed that in

ethereal and other solvents,  $\text{Li}^+$  splits the doubly degenerate antisymmetric S-O stretching mode of the triflate anion into two distinct bands, revealing a strong interaction between cation and anion, while the band remains degenerate when  $[\text{nBu}_4\text{N}][\text{OTf}]$  is used. For the above reasons, in solutions of  $\text{LiOTf}$  and  $\text{NaOTf}$ , they should be considered ion paired, bound species, but in  $[\text{nBu}_4\text{N}][\text{OTf}]$  solutions, with relatively little cation-anion interaction, it should be considered as “free triflate.”

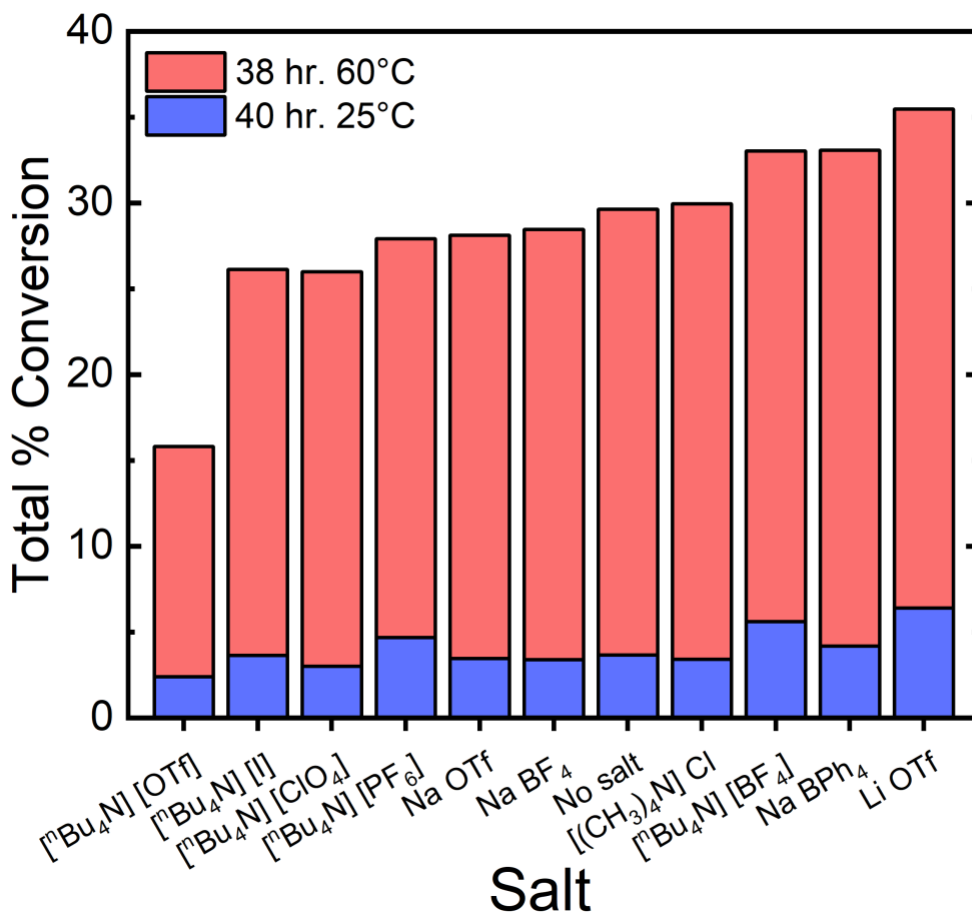
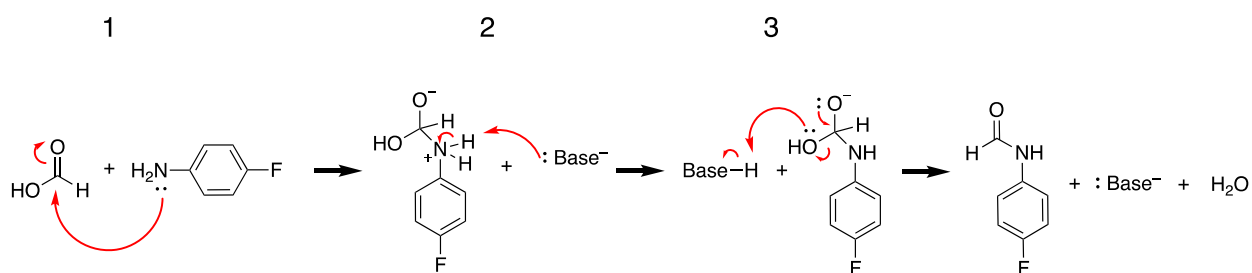


**Figure 3.3:** Conversions of 4-fluoroaniline to 4-fluoroanilide in the presence of a salt at 25°C (blue) and 60°C (red)

The reason “free triflate” ( $[\text{nBu}_4\text{N}][\text{OTf}]$ ) decreases the rate and/or yield of the reaction is unclear. It is worth noting, however, that the  $\text{p}K_a$  of triflic acid in THF is far higher than expected, 7.83. As a result, triflate is more basic than aniline (anilinium  $\text{p}K_a = 5.2$ ) or pyridine (pyridinium

$pK_a = 5.5$ ) in the same solvent.<sup>21</sup> A proposed mechanism for the amidation of formic acid and 4-fluoroaniline is shown in Scheme 3.2. Step 1 involves the nucleophilic attack of aniline on formic acid, although general organic principles state that carboxylic acids are poor electrophiles, formic acid (and possibly even acetic acid) is an exception to the common principles, as even a weak nucleophile like aniline can add in to the carbonyl carbon. Step 2 deprotonates the secondary amine resulting from the nucleophilic attack, and finally Step 3 protonates the hydroxyl, and it dissociates, leaving 4-fluoroformanilide, base, and water. A potential issue with free triflate in solution is in Step 3. Considering the contents of the solution, free triflate, but not ion-paired triflate, is likely to be the most basic site in solution other than methoxide. According to the proposed mechanism, an appreciable equilibrium must exist between the protonated hydroxyl and all other potential protonation states in solution. I hypothesize that of the salts chosen, triflate, but not  $\text{Li}^+$ - or  $\text{Na}^+$ -bound triflate, is too basic to allow for this equilibrium. There is some evidence that supports this possibility in Entries 37 and 38 where exogenous acids were added to the reaction with  $[\text{nBu}_4\text{N}][\text{HCO}_2]$  and 4-fluoroanilinium triflate and some conversion was noted.



**Scheme 3.2:** Plausible mechanism for the substitution of 4-fluoroaniline into formic acid

This proposed mechanism does not, however, explain the large difference in conversion when lower ratios of formic acid to aniline are used. Although a full explanation is difficult, there are reports of product-inhibited reactions where amides formed from the reaction bind tightly with the Lewis acid catalyst, necessitating the use of  $>1$  equivalent of catalyst.<sup>33</sup> One example even required 4.5 equivalents of catalyst to 1 equivalent of reactant.<sup>34</sup>

## *Conclusions and Outlook*

Putting all of these elementary steps together to form a cascade catalytic system will likely be difficult. My studies have shown that activation of the formate anion is very slow in the best of cases. Once protonated, the resulting formic acid reacts readily with nucleophiles, but the reactivity of  $\text{HCO}_2^-$  is very difficult beyond simple protonation and hydride transfer, forming  $\text{CO}_2$ . I was able to find two examples of formate reacting with amines to generate formamides without the presence of formic acid in excess (many examples), acid chlorides (one example),<sup>35</sup> anhydrides (one example),<sup>36</sup> DCC (dicyclohexylcarbodiimide) (one example),<sup>37</sup> or other harsh reagents and conditions likely not compatible with a possible cascade catalytic system. The first example is by Hanzlik and coworkers<sup>38</sup> where  $\text{NaH}^{13}\text{CO}_2$  reacted with methylbenzylamine hydrochloride over 48 hours at  $82^\circ\text{C}$ , resulting in a 74% yield in the desired  $^{13}\text{C}$ -labeled formamide product. Second, Gescher and coworkers<sup>39</sup> showed a very similar reaction of trifluoroethylamine hydrochloride with sodium formate, distilled on a Kugelrohr apparatus, and isolated in 83% yield. Notably, both of the substrates treated with the formate salt were amine acids, and the first was performed in acetonitrile, and the second was performed neat. Without a doubt, the triflate salt used in my studies was detrimental to the overall reactivity, and heating improved the reactivity, as expected. It is likely that switching salts away from the triflate salt used will improve reactivity. One unavoidable limitation for which I have no explanation is the decrease in reactivity seen at lower molar ratios of formic acid to aniline. This result may prove to be a major limitation when applied to a cascade catalytic cycle.

Ultimately, to achieve the desired reactivity, my data show that to achieve the desired reactivity, formic acid will likely need to be the product of the reduction of  $\text{CO}_2$ , the first step in the proposed catalytic cycle. Formic acid is reactive enough to undergo nucleophilic addition while none of the experiments with formate showed any appreciable product yield. Formic acid, however, is thermodynamically disfavored compared to hydrogen evolution at all pHs. It may be

possible to kinetically select for formic acid with quick conversion to another intermediate, even in the presence of a very strong hydride needed for the following step.

When considering the reduction of the formamide or ester, the stability of the formamide or ester must be overcome to form a much less stable product, formaldehyde. Mercer's studies showed that the hydride affinity of methyl formate was low, only fully reacting with HRh(dmpe)<sub>2</sub> in THF. This rhodium bisdiphosphine compound is tied for the most hydridic ground state metal complex with a hydricity of 26.6 kcal/mol, which can even donate its hydride to triethylborane.<sup>40</sup> Electrocatalytic studies with this compound have not yet been performed, but the reduction potentials required for such catalysis are expected to be relatively extreme, yielding very large overpotentials for the very slightly exergonic 6 H<sup>+</sup>, 6 e<sup>-</sup> CO<sub>2</sub> to methanol reaction.

## References

- (1) Sepulveda, N. A.; Jenkins, J. D.; de Sisternes, F. J.; Lester, R. K. The Role of Firm Low-Carbon Electricity Resources in Deep Decarbonization of Power Generation. *Joule* **2018**, *2* (11), 2403–2420. <https://doi.org/10.1016/j.joule.2018.08.006>.
- (2) Sinsel, S. R.; Riemke, R. L.; Hoffmann, V. H. Challenges and Solution Technologies for the Integration of Variable Renewable Energy Sources—a Review. *Renewable Energy* **2020**, *145*, 2271–2285. <https://doi.org/10.1016/j.renene.2019.06.147>.
- (3) Godula-Jopek, Dr.-Ing. habil. A.; Westenberger, A. F. Fuel Cell Types: PEMFC/DMFC/AFC/PAFC//MCFC/SOFC/. In *Encyclopedia of Energy Storage*; Cabeza, L. F., Ed.; Elsevier: Oxford, 2022; pp 250–265. <https://doi.org/10.1016/B978-0-12-819723-3.00056-1>.
- (4) Ilic, S.; Alherz, A.; Musgrave, C. B.; Glusac, K. D. Thermodynamic and Kinetic Hydricities of Metal-Free Hydrides. *Chem. Soc. Rev.* **2018**, *47* (8), 2809–2836. <https://doi.org/10.1039/C7CS00171A>.

- (5) Wiedner, E. S.; Chambers, M. B.; Pitman, C. L.; Bullock, R. M.; Miller, A. J. M.; Appel, A. M. Thermodynamic Hydricity of Transition Metal Hydrides. *Chem. Rev.* **2016**, *116* (15), 8655–8692. <https://doi.org/10.1021/acs.chemrev.6b00168>.
- (6) Waldie, K. M.; Ostericher, A. L.; Reineke, M. H.; Sasayama, A. F.; Kubiak, C. P. Hydricity of Transition-Metal Hydrides: Thermodynamic Considerations for CO<sub>2</sub> Reduction. *ACS Catal.* **2018**, *8* (2), 1313–1324. <https://doi.org/10.1021/acscatal.7b03396>.
- (7) Cunningham, D. W.; Barlow, J. M.; Velazquez, R. S.; Yang, J. Y. Reversible and Selective CO<sub>2</sub> to HCO<sub>2</sub><sup>-</sup> Electrocatalysis near the Thermodynamic Potential. *Angewandte Chemie International Edition* **2020**, *59* (11), 4443–4447. <https://doi.org/10.1002/anie.201913198>.
- (8) Bi, J.; Hou, P.; Kang, P. Single Iridium Pincer Complex for Roundtrip Electrochemical Conversion between Carbon Dioxide and Formate. *ChemCatChem* **2019**, *11* (8), 2069–2072. <https://doi.org/10.1002/cctc.201900083>.
- (9) Huff, C. A.; Sanford, M. S. Cascade Catalysis for the Homogeneous Hydrogenation of CO<sub>2</sub> to Methanol. *J. Am. Chem. Soc.* **2011**, *133* (45), 18122–18125. <https://doi.org/10.1021/ja208760j>.
- (10) Chu, W.-Y.; Culakova, Z.; Wang, B. T.; Goldberg, K. I. Acid-Assisted Hydrogenation of CO<sub>2</sub> to Methanol in a Homogeneous Catalytic Cascade System. *ACS Catal.* **2019**, *9* (10), 9317–9326. <https://doi.org/10.1021/acscatal.9b02280>.
- (11) Connelly, S. J.; Wiedner, E. S.; Appel, A. M. Predicting the Reactivity of Hydride Donors in Water: Thermodynamic Constants for Hydrogen. *Dalton Trans.* **2015**, *44* (13), 5933–5938. <https://doi.org/10.1039/C4DT03841J>.
- (12) DuBois, D. L.; Berning, D. E. Hydricity of Transition-Metal Hydrides and Its Role in CO<sub>2</sub> Reduction. *Applied Organometallic Chemistry* **2000**, *14* (12), 860–862. [https://doi.org/10.1002/1099-0739\(200012\)14:12<860::AID-AOC87>3.0.CO;2-A](https://doi.org/10.1002/1099-0739(200012)14:12<860::AID-AOC87>3.0.CO;2-A).



- (13) Tsay, C.; Livesay, B. N.; Ruelas, S.; Yang, J. Y. Solvation Effects on Transition Metal Hydricity. *J. Am. Chem. Soc.* **2015**, *137* (44), 14114–14121. <https://doi.org/10.1021/jacs.5b07777>.
- (14) Moret, S.; Dyson, P. J.; Laurency, G. Direct Synthesis of Formic Acid from Carbon Dioxide by Hydrogenation in Acidic Media. *Nat Commun* **2014**, *5* (1), 4017. <https://doi.org/10.1038/ncomms5017>.
- (15) Mathis, C. L.; Geary, J.; Ardon, Y.; Reese, M. S.; Philliber, M. A.; VanderLinden, R. T.; Saouma, C. T. Thermodynamic Analysis of Metal–Ligand Cooperativity of PNP Ru Complexes: Implications for CO<sub>2</sub> Hydrogenation to Methanol and Catalyst Inhibition. *J. Am. Chem. Soc.* **2019**, *141* (36), 14317–14328. <https://doi.org/10.1021/jacs.9b06760>.
- (16) Huff, C. A.; Kampf, J. W.; Sanford, M. S. Reversible Carbon–Carbon Bond Formation between Carbonyl Compounds and a Ruthenium Pincer Complex. *Chem. Commun.* **2013**, *49* (64), 7147–7149. <https://doi.org/10.1039/C3CC43517B>.
- (17) Yin, J.; Zhang, J.; Cai, C.; Deng, G.-J.; Gong, H. Catalyst-Free Transamidation of Aromatic Amines with Formamide Derivatives and Tertiary Amides with Aliphatic Amines. *Org. Lett.* **2019**, *21* (2), 387–392. <https://doi.org/10.1021/acs.orglett.8b03542>.
- (18) Zhang, Q.; Hou, J.; Huang, Y.; Zhan, L.; Li, B. Visible Light-Promoted Synthesis of Ureas and Formamides from Amines and CO<sub>2</sub>. *Chem. Commun.* **2022**, *58* (29), 4599–4602. <https://doi.org/10.1039/D2CC00572G>.
- (19) Liang, F.; Eda, K.; Okazoe, T.; Wada, A.; Mori, N.; Konishi, K.; Tsuda, A. Photo-on-Demand Synthesis of Vilsmeier Reagents with Chloroform and Their Applications to One-Pot Organic Syntheses. *J. Org. Chem.* **2021**, *86* (9), 6504–6517. <https://doi.org/10.1021/acs.joc.1c00334>.
- (20) Kütt, A.; Selberg, S.; Kaljurand, I.; Tshepelevitsh, S.; Heering, A.; Darnell, A.; Kaupmees, K.; Piirsalu, M.; Leito, I. PKa Values in Organic Chemistry – Making Maximum Use of the

- Available Data. *Tetrahedron Letters* **2018**, 59 (42), 3738–3748.  
<https://doi.org/10.1016/j.tetlet.2018.08.054>.
- (21) Tshepelevitsh, S.; Kütt, A.; Lõkov, M.; Kaljurand, I.; Saame, J.; Heering, A.; Plieger, P. G.; Vianello, R.; Leito, I. On the Basicity of Organic Bases in Different Media. *European Journal of Organic Chemistry* **2019**, 2019 (40), 6735–6748.  
<https://doi.org/10.1002/ejoc.201900956>.
- (22) Kütt, A.; Tshepelevitsh, S.; Saame, J.; Lõkov, M.; Kaljurand, I.; Selberg, S.; Leito, I. Strengths of Acids in Acetonitrile. *European Journal of Organic Chemistry* **2021**, 2021 (9), 1407–1419. <https://doi.org/10.1002/ejoc.202001649>.
- (23) Lunagariya, J.; Dhar, A.; L. Vekariya, R. Efficient Esterification of n -Butanol with Acetic Acid Catalyzed by the Brønsted Acidic Ionic Liquids: Influence of Acidity. *RSC Advances* **2017**, 7 (9), 5412–5420. <https://doi.org/10.1039/C6RA26722J>.
- (24) Barrett, A. G. M.; Braddock, D. C. Scandium(III) or Lanthanide(III) Triflates as Recyclable Catalysts for the Direct Acetylation of Alcohols with Acetic Acid. *Chem. Commun.* **1997**, No. 4, 351–352. <https://doi.org/10.1039/A606484A>.
- (25) Stirling, M. J.; Sweeney, G.; MacRory, K.; Blacker, A. J.; Page, M. I. The Kinetics and Mechanism of the Organo-Iridium-Catalysed Enantioselective Reduction of Imines. *Org. Biomol. Chem.* **2016**, 14 (14), 3614–3622. <https://doi.org/10.1039/C6OB00245E>.
- (26) Introduction. In *Industrial Catalysis*; John Wiley & Sons, Ltd, 2005; pp 1–14.  
<https://doi.org/10.1002/3527607684.ch1>.
- (27) Perrin, D. D. Tables. In *Ionisation Constants of Inorganic Acids and Bases in Aqueous Solution (Second Edition)*; Perrin, D. D., Ed.; Pergamon, 1982; pp 1–138.  
<https://doi.org/10.1016/B978-0-08-029214-4.50008-8>.
- (28) Drakenberg, T.; Forsen, S. Barrier to Internal Rotation of Amides. I. Formamide. *J. Phys. Chem.* **1970**, 74 (1), 1–7. <https://doi.org/10.1021/j100696a001>.

- (29) Haynes, W. M. *CRC Handbook of Chemistry and Physics*, 92nd ed.; CRC Press: Boca Raton, FL, 2011.
- (30) Schumann, H.; Meese-Marktscheffel, J. A.; Loebel, J. Die Kristall- und Molekülstruktur von Lithiumtrifluormethansulfonat Li[SO<sub>3</sub>CF<sub>3</sub>](THF). *Zeitschrift für Naturforschung B, Chemical Sciences* **45**, 1304.
- (31) Schädle, C.; Meermann, C.; Törnroos, K. W.; Anwander, R. Rare-Earth Metal Phenyl(Trimethylsilyl)Amide Complexes. *European Journal of Inorganic Chemistry* **2010**, 2010 (18), 2841–2852. <https://doi.org/10.1002/ejic.201000220>.
- (32) Frech, R.; Huang, W. Anion-Solvent and Anion-Cation Interactions in Lithium and Tetrabutylammonium Trifluoromethanesulfonate Solutions. *J Solution Chem* **1994**, 23 (4), 469–481. <https://doi.org/10.1007/BF00972613>.
- (33) Motiwala, H. F.; Fehl, C.; Li, S.-W.; Hirt, E.; Porubsky, P.; Aubé, J. Overcoming Product Inhibition in Catalysis of the Intramolecular Schmidt Reaction. *J. Am. Chem. Soc.* **2013**, 135 (24), 9000–9009. <https://doi.org/10.1021/ja402848c>.
- (34) Milligan, G. L.; Mossman, C. J.; Aube, J. Intramolecular Schmidt Reactions of Alkyl Azides with Ketones: Scope and Stereochemical Studies. *J. Am. Chem. Soc.* **1995**, 117 (42), 10449–10459. <https://doi.org/10.1021/ja00147a006>.
- (35) Ono, S.; Saitoh, A.; Iwakami, N.; Nakagawa, M.; Yamaguchi, S. N-Alkoxyalkyl-N,n-Dialkylamine Derivatives or Salts Thereof, and Remedies for Nerve Degeneration Diseases Containing the Same. EP1186594A1, March 13, 2002.
- (36) Gibson, K. R.; Jones, A.; Kemp, M. I.; Madin, A.; Stockley, M. L.; Whitlock, G. A.; Woodrow, M. D. Novel Compounds. WO2017141036A1, August 24, 2017.
- (37) Donets, P. A.; Cramer, N. Diaminophosphine Oxide Ligand Enabled Asymmetric Nickel-Catalyzed Hydrocarbamylation of Alkenes. *J. Am. Chem. Soc.* **2013**, 135 (32), 11772–11775. <https://doi.org/10.1021/ja406730t>.

- (38) Cerny, M. A.; Hanzlik, R. P. Cytochrome P450-Catalyzed Oxidation of N-Benzyl-N-Cyclopropylamine Generates Both Cyclopropanone Hydrate and 3-Hydroxypropionaldehyde via Hydrogen Abstraction, Not Single Electron Transfer. *J. Am. Chem. Soc.* **2006**, *128* (10), 3346–3354. <https://doi.org/10.1021/ja054938+>.
- (39) Gate, E. N.; Threadgill, M. D.; Stevens, M. F. G.; Chubb, D.; Vickers, L. M.; Langdon, S. P.; Hickman, J. A.; Gescher, A. Structural Studies on Bioactive Compounds. 4. A Structure-Antitumor Activity Study on Analogs of N-Methylformamide. *J. Med. Chem.* **1986**, *29* (6), 1046–1052. <https://doi.org/10.1021/jm00156a024>.
- (40) Mock, M. T.; Potter, R. G.; Camaioni, D. M.; Li, J.; Dougherty, W. G.; Kassel, W. S.; Twamley, B.; DuBois, D. L. Thermodynamic Studies and Hydride Transfer Reactions from a Rhodium Complex to BX<sub>3</sub> Compounds. *J. Am. Chem. Soc.* **2009**, *131* (40), 14454–14465. <https://doi.org/10.1021/ja905287q>.

## Appendix A: Tables of Cartesian Coordinates for DFT-Optimized Structures

<i>Protonation State</i>	<i>Method/Basis Set</i>			
	<i>B3LYP</i> <i>6-311g+(d,p)</i>	<i>B3LYP</i> <i>6-31g+(d,p)</i>	<i>B3LYP</i> <i>LANL2dz</i>	<i>B3P86</i> <i>LANL2dz</i>
<i>A</i>	1a	2a	3a	4a
<i>B</i>	1b	2b	3b	4b
<i>C</i>	1c	2c	3c	4c
<i>D</i>	1d	2d	3d	4d

<i>Protonation state</i>	<i>Compound</i>		
	<i>Mnt</i>	<i>LiPr</i>	<i>Mo</i>
<i>A</i>	5a	6a	7a
<i>B</i>	5b	6b	7b
<i>C</i>	5c	6c	7c

<b>1a</b>				<b>1b</b>			
Atom	X	Y	Z	Atom	X	Y	Z
W	-0.002855	-0.000163	0.390189	W	-0.035555	-0.014504	0.390027
S	1.628781	1.547288	-0.320339	S	-1.730797	-1.559589	-0.214799
S	1.627092	-1.547291	-0.324821	S	-1.630262	1.556805	-0.416244
S	-1.649974	-1.555615	-0.252106	S	1.742949	1.559814	-0.40405
S	-1.648134	1.556227	-0.254545	S	1.583379	-1.587068	-0.436766
C	3.14208	0.672537	-0.729271	C	-3.240684	-0.641523	-0.574899
C	3.141237	-0.672801	-0.731503	C	-3.194946	0.695232	-0.679974
C	-3.14727	-0.671568	-0.711377	C	3.286801	0.604527	-0.584293
C	-3.146381	0.673077	-0.712641	C	3.161687	-0.725577	-0.666147
C	-4.289936	1.572997	-1.103887	C	4.297313	-1.668866	-0.963515
H	-4.557809	2.243944	-0.281116	H	4.433831	-2.371498	-0.135822
H	-4.013759	2.206159	-1.953604	H	4.069753	-2.263981	-1.853161
H	-5.183079	1.011828	-1.38079	H	5.241706	-1.151851	-1.132905
C	-4.291953	-1.570787	-1.100974	C	4.512565	1.457838	-0.743251
H	-4.560258	-2.240278	-0.277159	H	4.674828	2.082178	0.142464
H	-5.184601	-1.009073	-1.378372	H	5.407536	0.852515	-0.886838
H	-4.016743	-2.205465	-1.949875	H	4.418	2.132572	-1.600379
C	4.299095	-1.573366	-1.075954	C	-4.344643	1.613029	-1.00421
H	4.570677	-2.202979	-0.222028	H	-4.551836	2.293213	-0.170737
H	4.037643	-2.247341	-1.8981	H	-4.11078	2.237969	-1.872724
H	5.186456	-1.012228	-1.370942	H	-5.262488	1.065834	-1.223822
C	4.301006	1.572904	-1.07068	C	-4.45173	-1.518379	-0.761185
H	4.572678	2.199949	-0.214896	H	-4.6798	-2.070479	0.157106
H	5.188033	1.011765	-1.366672	H	-5.339493	-0.94738	-1.036483
H	4.040645	2.249361	-1.891134	H	-4.276509	-2.264117	-1.543969
S	0.122591	-0.001102	2.757896	S	0.059994	0.050564	2.562135
H	-1.201563	-0.003686	3.03103	H	2.04397	2.252241	0.715725

	<b>1c</b>		
<b>Atom</b>	<b>X</b>	<b>Y</b>	<b>Z</b>
<b>W</b>	0.000002	0.340974	0.373607
<b>S</b>	1.929569	1.388709	-0.707137
<b>S</b>	1.53217	-1.57437	0.166108
<b>S</b>	-1.532237	-1.574335	0.166252
<b>S</b>	-1.929546	1.388708	-0.707162
<b>C</b>	3.283242	0.235463	-0.831077
<b>C</b>	3.113425	-1.03695	-0.436683
<b>C</b>	-3.113452	-1.036919	-0.436641
<b>C</b>	-3.283233	0.23548	-0.831099
<b>C</b>	-4.535221	0.841905	-1.412178
<b>H</b>	-4.88718	1.682257	-0.805339
<b>H</b>	-4.3526	1.231202	-2.419214
<b>H</b>	-5.348844	0.119328	-1.480371
<b>C</b>	-4.141437	-2.139429	-0.480562
<b>H</b>	-4.325592	-2.543673	0.519892
<b>H</b>	-5.095468	-1.795989	-0.880624
<b>H</b>	-3.799154	-2.972771	-1.102243
<b>C</b>	4.141391	-2.139478	-0.480612
<b>H</b>	4.325503	-2.543765	0.519832
<b>H</b>	3.799114	-2.972789	-1.102338
<b>H</b>	5.095442	-1.79604	-0.880627
<b>C</b>	4.535262	0.841891	-1.412085
<b>H</b>	4.887223	1.6822	-0.805188
<b>H</b>	5.34887	0.119298	-1.480295
<b>H</b>	4.352679	1.231248	-2.419104
<b>S</b>	0.000042	0.778109	2.49055
<b>H</b>	0.000003	2.0065	0.076555

	<b>1d</b>		
<b>Atom</b>	<b>X</b>	<b>Y</b>	<b>Z</b>
<b>W</b>	0.000002	-0.6423	-0.002376
<b>S</b>	1.72734	-0.000199	1.566047
<b>S</b>	1.727529	0.010716	-1.566529
<b>S</b>	-1.727505	0.010751	-1.566539
<b>S</b>	-1.727328	-0.000179	1.566049
<b>C</b>	2.875448	1.010334	0.682678
<b>C</b>	2.875067	1.01552	-0.675923
<b>C</b>	-2.875064	1.015525	-0.675927
<b>C</b>	-2.875451	1.010332	0.682675
<b>C</b>	-3.809729	1.808515	1.557343
<b>H</b>	-4.123631	1.220818	2.423945
<b>H</b>	-3.313991	2.707821	1.938692
<b>H</b>	-4.705477	2.124135	1.021889
<b>C</b>	-3.807765	1.821191	-1.545127
<b>H</b>	-4.141013	1.232358	-2.403866
<b>H</b>	-4.691665	2.155083	-1.001322
<b>H</b>	-3.302592	2.709761	-1.938925
<b>C</b>	3.807755	1.821198	-1.545127
<b>H</b>	4.141014	1.232366	-2.403863
<b>H</b>	3.302568	2.709758	-1.93893
<b>H</b>	4.691649	2.155107	-1.001322
<b>C</b>	3.809706	1.808537	1.557348
<b>H</b>	4.123617	1.220848	2.423953
<b>H</b>	4.70545	2.124175	1.021897
<b>H</b>	3.313948	2.707834	1.938694
<b>S</b>	-0.000025	-2.881367	-0.007583
<b>H</b>	0.000009	1.127683	0.004181

	<b>2a</b>		
Atom	X	Y	Z
W	-0.002603	-0.000106	0.39182
S	1.628195	1.547824	-0.317411
S	1.626004	-1.548194	-0.322446
S	-1.64748	-1.555854	-0.249963
S	-1.644823	1.556465	-0.25462
C	3.141358	0.675105	-0.728859
C	3.140208	-0.675952	-0.731617
C	-3.144138	-0.67442	-0.713664
C	-3.142902	0.676024	-0.715822
C	-4.287253	1.576829	-1.111777
H	-4.553479	2.255054	-0.291826
H	-4.011245	2.205369	-1.967523
H	-5.1835	1.014528	-1.384122
C	-4.289919	-1.574401	-1.107397
H	-4.556413	-2.25112	-0.286306
H	-5.185663	-1.011404	-1.37997
H	-4.015268	-2.204512	-1.962439
C	4.299456	-1.577371	-1.079377
H	4.565441	-2.217901	-0.229349
H	4.04087	-2.243606	-1.911401
H	5.191531	-1.014587	-1.364143
C	4.302192	1.576177	-1.07224
H	4.568686	2.212511	-0.219213
H	5.193584	1.013301	-1.358951
H	4.045097	2.24653	-1.901406
S	0.112444	-0.000472	2.75668
H	-1.210444	-0.004548	3.030685

	<b>2b</b>		
Atom	X	Y	Z
W	-0.035545	-0.016264	0.398187
S	-1.72822	-1.558984	-0.213871
S	-1.622373	1.556679	-0.415073
S	1.737416	1.560695	-0.394695
S	1.577979	-1.587776	-0.433535
C	-3.235589	-0.642222	-0.584919
C	-3.187366	0.700281	-0.690235
C	3.279727	0.608554	-0.595353
C	3.154709	-0.727362	-0.677942
C	4.290417	-1.671686	-0.984211
H	4.428641	-2.380078	-0.15918
H	4.059375	-2.263452	-1.877623
H	5.236907	-1.154507	-1.153849
C	4.505909	1.463784	-0.764814
H	4.679834	2.084703	0.123514
H	5.400343	0.857838	-0.922996
H	4.401239	2.144419	-1.618635
C	-4.335757	1.621299	-1.0208
H	-4.539155	2.310782	-0.191485
H	-4.100913	2.239453	-1.896448
H	-5.257989	1.07524	-1.234472
C	-4.448749	-1.51867	-0.778458
H	-4.682511	-2.073048	0.139392
H	-5.336076	-0.945135	-1.05768
H	-4.271013	-2.265206	-1.562709
S	0.062217	0.049707	2.569527
H	2.039561	2.24351	0.729077



	<b>2c</b>		
Atom	X	Y	Z
W	-0.001742	-0.327133	0.400458
S	-1.915926	-1.400752	-0.68094
S	-1.520963	1.581888	0.12679
S	1.569786	1.558931	0.221591
S	1.8918	-1.396875	-0.714453
C	-3.265642	-0.248654	-0.854784
C	-3.097564	1.037291	-0.484359
C	3.116916	1.01379	-0.456354
C	3.255318	-0.260913	-0.876173
C	4.483399	-0.878068	-1.502557
H	4.841383	-1.729672	-0.911613
H	4.263252	-1.254845	-2.508865
H	5.302899	-0.161056	-1.586363
C	4.16241	2.102156	-0.526897
H	4.388308	2.492312	0.472623
H	5.095325	1.742792	-0.965851
H	3.808878	2.946955	-1.129849
C	-4.124621	2.141768	-0.570205
H	-4.324834	2.566723	0.420645
H	-3.767496	2.961258	-1.20526
H	-5.071883	1.786484	-0.980931
C	-4.515528	-0.86401	-1.437866
H	-4.880699	-1.685387	-0.809746
H	-5.32185	-0.13401	-1.536607
H	-4.318623	-1.282724	-2.432359
S	-0.022954	-0.737897	2.524258
H	-0.001759	-1.98585	0.159504

	<b>2d</b>		
Atom	X	Y	Z
W	0.000018	-0.635981	-0.000681
S	-1.724902	0.006722	-1.568486
S	-1.72792	0.000085	1.565975
S	1.724903	0.003447	1.568297
S	1.728092	0.003006	-1.566144
C	-2.880183	1.00737	-0.682306
C	-2.881607	1.004477	0.681887
C	2.880214	1.00587	0.68421
C	2.881492	1.005837	-0.680009
C	3.819482	1.806271	-1.55263
H	4.147698	1.21395	-2.413383
H	3.319424	2.699929	-1.947013
H	4.70862	2.134782	-1.010117
C	3.816793	1.806258	1.558455
H	4.138578	1.215964	2.422974
H	4.709896	2.129245	1.019099
H	3.318229	2.703325	1.946986
C	-3.819989	1.80266	1.556201
H	-4.145115	1.209466	2.4175
H	-3.321593	2.697643	1.949693
H	-4.711049	2.128722	1.015333
C	-3.816553	1.809537	-1.555086
H	-4.143604	1.218744	-2.417333
H	-4.706455	2.137421	-1.013454
H	-3.315576	2.70368	-1.947197
S	-0.000089	-2.873478	-0.002022
H	0.000404	1.143542	0.001032

	<b>3a</b>		
Atom	X	Y	Z
W	-0.003806	-0.000041	0.352635
S	1.659081	1.592523	-0.327124
S	1.657097	-1.592665	-0.331422
S	-1.673456	-1.598036	-0.256988
S	-1.671722	1.598527	-0.260645
C	3.240082	0.675793	-0.700153
C	3.239163	-0.676688	-0.702194
C	-3.240244	-0.675405	-0.689742
C	-3.239351	0.676381	-0.691792
C	-4.392571	1.592214	-1.044214
H	-4.63749	2.25457	-0.202677
H	-4.132942	2.235626	-1.895959
H	-5.296516	1.032775	-1.306512
C	-4.394717	-1.590907	-1.038934
H	-4.639533	-2.250864	-0.195482
H	-5.298353	-1.031229	-1.301783
H	-4.136519	-2.236775	-1.889256
C	4.406811	-1.592315	-1.004286
H	4.64239	-2.223959	-0.136639
H	4.169253	-2.265924	-1.838716
H	5.310388	-1.032652	-1.267296
C	4.408884	1.59076	-0.99981
H	4.644491	2.220656	-0.130909
H	5.312089	1.030661	-1.263178
H	4.172574	2.266067	-1.833231
S	0.106356	0.00015	2.758169
H	-1.234205	-0.002898	3.081611

	<b>3b</b>		
Atom	X	Y	Z
W	0.042484	0.019567	0.39677
S	1.758558	1.598934	-0.204734
S	1.621502	-1.591529	-0.466912
S	-1.784715	-1.613644	-0.367669
S	-1.581075	1.614357	-0.483606
C	3.318721	0.632552	-0.57819
C	3.258053	-0.70909	-0.710331
C	-3.378054	-0.598015	-0.588663
C	-3.232351	0.73605	-0.692161
C	-4.355561	1.707863	-0.989088
H	-4.467159	2.42309	-0.163736
H	-4.12545	2.288691	-1.89183
H	-5.315862	1.205835	-1.140708
C	-4.612383	-1.456693	-0.719751
H	-4.79092	-2.040847	0.19428
H	-5.501906	-0.845617	-0.901069
H	-4.514482	-2.169076	-1.54977
C	4.397889	-1.65253	-1.03245
H	4.578225	-2.348236	-0.200847
H	4.163018	-2.261543	-1.916305
H	5.331902	-1.115722	-1.230182
C	4.54072	1.514239	-0.730712
H	4.761369	2.043378	0.206945
H	5.430175	0.939744	-1.010741
H	4.375868	2.280197	-1.501136
S	-0.050878	-0.046123	2.598224
H	-2.10505	-2.286035	0.787358

Atom	X	3c Y	Z
W	-0.002412	-0.298438	0.450806
S	-1.920438	-1.473082	-0.644493
S	-1.5433	1.607154	0.056639
S	1.619916	1.579425	0.200421
S	1.894638	-1.476333	-0.668852
C	-3.315904	-0.294426	-0.90198
C	-3.159637	1.011253	-0.58711
C	3.188921	0.978737	-0.542702
C	3.303792	-0.314628	-0.92245
C	4.508846	-0.977892	-1.559177
H	4.878081	-1.802597	-0.934893
H	4.251322	-1.401284	-2.539299
H	5.331318	-0.270598	-1.703429
C	4.234616	2.066961	-0.685907
H	4.489756	2.496349	0.291929
H	5.154859	1.685504	-1.138262
H	3.862265	2.886591	-1.314779
C	-4.183977	2.118016	-0.738393
H	-4.398506	2.587921	0.230652
H	-3.8133	2.905948	-1.407531
H	-5.126409	1.742587	-1.148216
C	-4.556459	-0.957076	-1.466278
H	-4.925461	-1.739204	-0.789266
H	-5.365375	-0.236489	-1.621289
H	-4.340763	-1.436255	-2.430662
S	-0.046752	-0.557941	2.628338
H	-0.005481	-1.987291	0.416495

Atom	X	3d Y	Z
W	0.000003	-0.654756	-0.002983
S	-1.747881	-0.012617	-1.604956
S	-1.746855	-0.022524	1.604372
S	1.747216	-0.022958	1.604258
S	1.747945	-0.012708	-1.605045
C	-2.913519	1.058126	-0.679419
C	-2.913015	1.05409	0.686135
C	2.913049	1.054	0.686066
C	2.913458	1.058204	-0.679496
C	3.830583	1.873668	-1.56858
H	4.240942	1.253234	-2.375276
H	3.282191	2.700593	-2.040423
H	4.668146	2.302917	-1.010947
C	3.829713	1.864587	1.580217
H	4.22625	1.244032	2.393568
H	4.676992	2.28247	1.028541
H	3.285313	2.699383	2.042852
C	-3.829791	1.864577	1.580249
H	-4.226291	1.243988	2.393591
H	-3.285499	2.699444	2.042882
H	-4.677089	2.282366	1.028527
C	-3.830958	1.873263	-1.568487
H	-4.241057	1.252693	-2.375208
H	-4.668699	2.302149	-1.010839
H	-3.282887	2.700425	-2.040291
S	-0.000167	-2.918741	-0.003659
H	0.000233	1.117936	0.004172

	<b>4a</b>		
<b>Atom</b>	<b>X</b>	<b>Y</b>	<b>Z</b>
<b>W</b>	-0.003378	-0.000054	0.352915
<b>S</b>	1.63978	1.580147	-0.324399
<b>S</b>	1.637837	-1.580238	-0.328834
<b>S</b>	-1.657215	-1.585587	-0.250909
<b>S</b>	-1.655498	1.586079	-0.254073
<b>C</b>	3.212233	0.674486	-0.698164
<b>C</b>	3.21134	-0.675281	-0.700212
<b>C</b>	-3.21455	-0.674047	-0.684663
<b>C</b>	-3.213658	0.675108	-0.686556
<b>C</b>	-4.358937	1.586421	-1.041379
<b>H</b>	-4.607456	2.246703	-0.201131
<b>H</b>	-4.095317	2.229735	-1.89014
<b>H</b>	-5.260526	1.027371	-1.308316
<b>C</b>	-4.361137	-1.585	-1.0362
<b>H</b>	-4.609981	-2.242325	-0.19372
<b>H</b>	-5.262218	-1.025707	-1.30433
<b>H</b>	-4.098775	-2.231336	-1.883046
<b>C</b>	4.371599	-1.58652	-1.00277
<b>H</b>	4.608305	-2.216843	-0.136292
<b>H</b>	4.132082	-2.259243	-1.835511
<b>H</b>	5.273757	-1.027383	-1.267542
<b>C</b>	4.373538	1.58511	-0.998597
<b>H</b>	4.609725	2.214589	-0.131381
<b>H</b>	5.275587	1.025526	-1.262804
<b>H</b>	4.135451	2.258659	-1.831098
<b>S</b>	0.113404	-0.000069	2.730979
<b>H</b>	-1.226188	-0.002758	3.056606

	<b>4b</b>		
<b>Atom</b>	<b>X</b>	<b>Y</b>	<b>Z</b>
<b>W</b>	0.038251	0.01834	0.379957
<b>S</b>	1.733652	1.587912	-0.215763
<b>S</b>	1.620878	-1.581681	-0.434703
<b>S</b>	-1.74689	-1.591715	-0.388843
<b>S</b>	-1.573739	1.606502	-0.461823
<b>C</b>	3.294548	0.638874	-0.564883
<b>C</b>	3.243906	-0.701995	-0.679525
<b>C</b>	-3.344268	-0.604189	-0.581284
<b>C</b>	-3.212421	0.729516	-0.668446
<b>C</b>	-4.338528	1.692084	-0.93919
<b>H</b>	-4.448846	2.390637	-0.101213
<b>H</b>	-4.119549	2.289886	-1.831869
<b>H</b>	-5.295211	1.185646	-1.092166
<b>C</b>	-4.563687	-1.468656	-0.718873
<b>H</b>	-4.729293	-2.071758	0.183497
<b>H</b>	-5.459869	-0.863865	-0.881499
<b>H</b>	-4.464515	-2.162065	-1.562956
<b>C</b>	4.384747	-1.636084	-0.986568
<b>H</b>	4.56417	-2.323932	-0.150234
<b>H</b>	4.158185	-2.251187	-1.866678
<b>H</b>	5.315545	-1.095151	-1.182803
<b>C</b>	4.504176	1.523261	-0.719
<b>H</b>	4.71778	2.058787	0.215029
<b>H</b>	5.397392	0.953275	-0.992321
<b>H</b>	4.33617	2.282004	-1.493816
<b>S</b>	-0.06904	-0.051227	2.56618
<b>H</b>	-2.051133	-2.303011	0.746048

Atom	X	4c Y	Z
W	-0.002028	-0.28494	0.454608
S	-1.891947	-1.471011	-0.615906
S	-1.529918	1.593803	0.046951
S	1.602778	1.56681	0.182793
S	1.86064	-1.472159	-0.653205
C	-3.282341	-0.310938	-0.897192
C	-3.132021	0.995951	-0.596602
C	3.159436	0.963728	-0.554562
C	3.267335	-0.330593	-0.92314
C	4.460481	-1.000978	-1.554745
H	4.826429	-1.821959	-0.926154
H	4.198619	-1.428704	-2.53021
H	5.28527	-0.299188	-1.705224
C	4.202504	2.041162	-0.708562
H	4.463804	2.474445	0.26432
H	5.117894	1.653083	-1.162756
H	3.830613	2.857054	-1.340019
C	-4.151295	2.092982	-0.767627
H	-4.376768	2.570379	0.19362
H	-3.775761	2.874124	-1.439637
H	-5.087401	1.711276	-1.183481
C	-4.509161	-0.979669	-1.461876
H	-4.87878	-1.757379	-0.782474
H	-5.319193	-0.264101	-1.627106
H	-4.284795	-1.463638	-2.420266
S	-0.037493	-0.522209	2.623684
H	-0.004479	-1.973496	0.45519

Atom	X	4d Y	Z
W	-0.002028	-0.28494	0.454608
S	-1.891947	-1.471011	-0.615906
S	-1.529918	1.593803	0.046951
S	1.602778	1.56681	0.182793
S	1.86064	-1.472159	-0.653205
C	-3.282341	-0.310938	-0.897192
C	-3.132021	0.995951	-0.596602
C	3.159436	0.963728	-0.554562
C	3.267335	-0.330593	-0.92314
C	4.460481	-1.000978	-1.554745
H	4.826429	-1.821959	-0.926154
H	4.198619	-1.428704	-2.53021
H	5.28527	-0.299188	-1.705224
C	4.202504	2.041162	-0.708562
H	4.463804	2.474445	0.26432
H	5.117894	1.653083	-1.162756
H	3.830613	2.857054	-1.340019
C	-4.151295	2.092982	-0.767627
H	-4.376768	2.570379	0.19362
H	-3.775761	2.874124	-1.439637
H	-5.087401	1.711276	-1.183481
C	-4.509161	-0.979669	-1.461876
H	-4.87878	-1.757379	-0.782474
H	-5.319193	-0.264101	-1.627106
H	-4.284795	-1.463638	-2.420266
S	-0.037493	-0.522209	2.623684
H	-0.004479	-1.973496	0.45519

	<b>5a</b>		
<b>Atom</b>	<b>X</b>	<b>Y</b>	<b>Z</b>
<b>W</b>	-0.003888	-0.002781	0.431208
<b>S</b>	1.630547	1.587125	-0.193672
<b>S</b>	1.622205	-1.586344	-0.229331
<b>S</b>	-1.649258	-1.593239	-0.154769
<b>S</b>	-1.63836	1.596385	-0.162455
<b>C</b>	3.109313	0.682917	-0.568804
<b>C</b>	3.105744	-0.680345	-0.5842
<b>C</b>	-3.118786	-0.676097	-0.551152
<b>C</b>	-3.113482	0.686369	-0.556744
<b>C</b>	-4.258672	1.449985	-0.899107
<b>C</b>	-4.270532	-1.434186	-0.883283
<b>C</b>	4.257968	-1.442205	-0.90564
<b>C</b>	4.264665	1.44545	-0.878306
<b>S</b>	0.13477	-0.011869	2.755254
<b>N</b>	-5.194437	-2.081251	-1.145917
<b>N</b>	-5.177586	2.099778	-1.172117
<b>N</b>	5.192046	2.094324	-1.123465
<b>N</b>	5.183305	-2.090338	-1.15981
<b>H</b>	-1.191352	-0.016035	3.022739

	<b>5b</b>		
<b>Atom</b>	<b>X</b>	<b>Y</b>	<b>Z</b>
<b>W</b>	-0.03688	-0.020278	0.430575
<b>S</b>	-1.662459	-1.586216	-0.35287
<b>S</b>	-1.694633	1.602961	-0.107737
<b>S</b>	1.614908	1.629071	-0.242223
<b>S</b>	1.741026	-1.617483	-0.32231
<b>C</b>	-3.165946	-0.661775	-0.579151
<b>C</b>	-3.179917	0.695626	-0.467759
<b>C</b>	3.119549	0.736131	-0.516031
<b>C</b>	3.254066	-0.61617	-0.482822
<b>C</b>	4.45845	-1.311702	-0.707627
<b>C</b>	4.255752	1.550851	-0.803614
<b>C</b>	-4.359675	1.459916	-0.651379
<b>C</b>	-4.3317	-1.409125	-0.881228
<b>S</b>	0.018015	-0.128739	2.566461
<b>N</b>	5.15601	2.237525	-1.036325
<b>N</b>	5.43185	-1.918428	-0.874931
<b>N</b>	-5.26702	-2.048075	-1.125237
<b>N</b>	-5.305484	2.113583	-0.794646
<b>H</b>	2.04845	-2.247707	0.831944

5c			
Atom	X	Y	Z
W	-0.000228	-0.40166	0.373759
S	-1.981846	-1.511687	-0.545852
S	-1.513475	1.573429	0.174117
S	1.516647	1.572093	0.182524
S	1.98095	-1.511835	-0.547463
C	-3.287625	-0.331498	-0.627972
C	-3.07966	0.978682	-0.317427
C	3.080902	0.977349	-0.314479
C	3.287404	-0.332209	-0.628823
C	4.545555	-0.821274	-1.065725
C	4.117925	1.946355	-0.40235
C	-4.11605	1.948261	-0.405681
C	-4.546778	-0.820756	-1.061884
S	-0.001978	-0.781147	2.466725
N	4.950906	2.747056	-0.46544
N	5.561404	-1.244981	-1.425186
N	-5.563377	-1.244652	-1.41897
N	-4.94859	2.749401	-0.469129
H	-0.000299	-2.048002	0.058129

6a			
Atom	X	Y	Z
S	-1.651031	-1.536984	-0.001938
S	-1.606707	1.549053	-0.046221
S	1.66226	1.543039	0.076818
S	1.619278	-1.55263	-0.045612
C	-3.1546	-0.655472	-0.448152
C	-3.131581	0.693753	-0.477432
C	3.15714	0.668443	-0.423107
C	3.136902	-0.679154	-0.479083
S	-0.106308	-0.046912	3.053613
C	-4.340345	-1.542176	-0.805501
C	-4.780599	-2.427134	0.376427
C	-4.078927	-2.393678	-2.062867
H	-5.182354	-0.885654	-1.037753
H	-5.00507	-1.82244	1.259348
H	-5.680757	-2.990485	0.111989
H	-4.001253	-3.144323	0.647171
H	-3.805386	-1.765086	-2.914617
H	-3.269188	-3.108306	-1.896149
H	-4.978137	-2.957121	-2.330433
C	-4.284207	1.600752	-0.888163
C	-3.989436	2.359621	-2.196651
C	-4.694061	2.574661	0.232844
H	-5.149505	0.962107	-1.081412
H	-3.742731	1.667121	-3.005963
H	-4.864847	2.941358	-2.501431
H	-3.150573	3.049339	-2.074197
H	-4.935608	2.036897	1.153727
H	-3.893172	3.284313	0.455875
H	-5.577146	3.146198	-0.068916
C	4.331016	1.564646	-0.79631
C	4.771526	2.472101	0.367877
C	4.048067	2.394735	-2.063693
H	5.179171	0.915128	-1.026049
H	5.007634	1.88405	1.258968
H	5.665232	3.037853	0.087211
H	3.988983	3.187855	0.632528
H	3.780101	1.74988	-2.905002
H	3.226672	3.09707	-1.901005
H	4.935475	2.970163	-2.344996
C	4.289138	-1.57589	-0.912728
C	3.97484	-2.350338	-2.207209
C	4.73475	-2.5348	0.207963
H	5.142418	-0.929345	-1.131364
H	3.696369	-1.669103	-3.015785
H	4.852566	-2.919425	-2.528754
H	3.151468	-3.053322	-2.058735
H	4.996131	-1.984805	1.116154
H	3.944309	-3.246685	0.459506
H	5.6136	-3.104331	-0.109597
W	0.002981	-0.009075	0.679686
H	1.21736	0.013157	3.321122

6b			
Atom	X	Y	Z
S	1.616701	1.554067	-0.183727
S	1.718849	-1.55048	-0.009107
S	-1.583504	-1.570749	-0.181016
S	-1.73503	1.571394	-0.116565
C	3.184316	0.702465	-0.497472
C	3.232112	-0.639329	-0.400616
C	-3.163447	-0.70934	-0.441468
C	-3.289004	0.624312	-0.348623
S	-0.023196	0.033271	2.825932
C	4.346163	1.619554	-0.855461
C	4.708653	2.584983	0.289599
C	4.100457	2.391404	-2.166388
H	5.222188	0.987973	-1.02299
H	4.920467	2.038647	1.212776
H	5.597783	3.166838	0.026918
H	3.893919	3.285071	0.491319
H	3.885277	1.7071	-2.991684
H	3.257154	3.07983	-2.070029
H	4.986255	2.976809	-2.432092
C	4.460561	-1.511612	-0.625247
C	4.297644	-2.459449	-1.829414
C	4.861179	-2.296027	0.639015
H	5.295647	-0.846777	-0.859583
H	4.050115	-1.903314	-2.737768
H	5.22874	-3.006276	-2.008399
H	3.504884	-3.191079	-1.654723
H	5.017595	-1.623399	1.486765
H	4.090226	-3.018365	0.919079
H	5.79185	-2.84506	0.464372
C	-4.319448	-1.641564	-0.79013
C	-4.634338	-2.626932	0.350553
C	-4.080934	-2.384437	-2.118701
H	-5.209805	-1.025478	-0.931873
H	-4.833421	-2.097257	1.285999
H	-5.521133	-3.215605	0.097936
H	-3.805353	-3.317371	0.520954
H	-3.880624	-1.683011	-2.93301
H	-3.234638	-3.070806	-2.045592
H	-4.969411	-2.965821	-2.382108
C	-4.52827	1.476709	-0.567821
C	-4.48932	2.230169	-1.911702
C	-4.810074	2.442901	0.599045
H	-5.375155	0.788227	-0.607334
H	-4.363798	1.537277	-2.747307
H	-5.421969	2.781873	-2.061504
H	-3.666621	2.949775	-1.940855
H	-4.814571	1.918772	1.558369
H	-4.073998	3.25047	0.650965
H	-5.789762	2.909178	0.463758
W	0.04156	-0.015944	0.647018
H	-2.015881	2.188722	1.049042

6c			
Atom	X	Y	Z
S	-1.908013	-1.590384	-0.22527
S	-1.539964	1.461546	0.189624
S	1.539872	1.461557	0.189441
S	1.90805	-1.590375	-0.225208
C	-3.277773	-0.486814	-0.542292
C	-3.1175	0.837563	-0.349597
C	3.117502	0.837586	-0.34953
C	3.277827	-0.486796	-0.542139
S	0.000033	-0.497851	2.853866
C	-4.546287	-1.179802	-1.027943
C	-5.148043	-2.113373	0.040204
C	-4.338896	-1.926072	-2.359974
H	-5.285748	-0.398898	-1.217847
H	-5.333854	-1.575087	0.973421
H	-6.099341	-2.524558	-0.311125
H	-4.479633	-2.949894	0.259594
H	-3.939079	-1.258459	-3.12785
H	-3.645614	-2.763046	-2.244995
H	-5.292388	-2.325327	-2.71869
C	-4.168717	1.914427	-0.598079
C	-3.787264	2.84791	-1.76316
C	-4.498049	2.722168	0.67132
H	-5.086855	1.401186	-0.891158
H	-3.587342	2.278748	-2.674876
H	-4.605084	3.545033	-1.969155
H	-2.895426	3.433904	-1.527189
H	-4.795023	2.063897	1.492089
H	-3.639045	3.310678	1.003428
H	-5.323546	3.412322	0.472584
C	4.168695	1.914469	-0.598028
C	4.497701	2.722568	0.671222
C	3.787403	2.84762	-1.763433
H	5.086938	1.401224	-0.890772
H	4.79451	2.064535	1.492243
H	5.323223	3.41269	0.472482
H	3.638608	3.311146	1.002977
H	3.58777	2.278208	-2.675055
H	2.895429	3.433549	-1.527807
H	4.605175	3.544806	-1.969406
C	4.546382	-1.179774	-1.027691
C	4.33913	-1.925788	-2.35989
C	5.147933	-2.113575	0.040367
H	5.285921	-0.398888	-1.217332
H	3.939522	-1.257992	-3.127715
H	5.292629	-2.325104	-2.71852
H	3.645722	-2.762693	-2.245161
H	5.333586	-1.575487	0.97373
H	4.479487	-2.950141	0.259468
H	6.099291	-2.524685	-0.310884
W	0.000003	-0.38579	0.688373
H	-0.000009	-2.05899	0.656542



Atom	X	7a Y	Z
Mo	-0.00203	0.000702	0.511556
S	-1.633617	-1.552833	-0.196607
S	-1.624008	1.55425	-0.217737
S	1.630828	1.547457	-0.217169
S	1.621118	-1.549893	-0.231067
C	-3.109618	-0.672813	-0.683368
C	-3.104999	0.67599	-0.693364
C	3.113226	0.67144	-0.682599
C	3.108354	-0.678019	-0.690111
S	0.076443	0.004018	2.898124
C	4.250889	-1.574419	-1.096357
H	5.130745	-1.009176	-1.404941
H	4.546918	-2.227809	-0.269259
H	3.959023	-2.22385	-1.927889
C	4.262339	1.564471	-1.077649
H	5.139787	0.996835	-1.388682
H	3.976908	2.223376	-1.903943
H	4.559783	2.208364	-0.243637
C	-4.242815	1.57119	-1.115298
H	-5.130084	1.005941	-1.401867
H	-4.526115	2.249544	-0.304071
H	-3.952001	2.195318	-1.966531
C	-4.253203	-1.566503	-1.092865
H	-5.141727	-0.999974	-1.372978
H	-3.971447	-2.193847	-1.944866
H	-4.530923	-2.241746	-0.277227
H	-1.252875	-0.008482	3.141487

Atom	X	7b Y	Z
Mo	-0.047901	-0.016025	0.570579
S	-1.684155	-1.566409	-0.191244
S	-1.572276	1.56565	-0.354899
S	1.805005	1.540404	0.042668
S	1.583987	-1.604094	-0.260234
C	-3.153172	-0.638661	-0.640931
C	-3.102317	0.702334	-0.730618
C	3.207382	0.611445	-0.639445
C	3.100738	-0.726026	-0.662573
S	-0.125776	0.024227	2.737675
C	4.21774	-1.653744	-1.069392
H	5.130657	-1.12301	-1.338152
H	4.452184	-2.341429	-0.251261
H	3.91113	-2.264958	-1.923215
C	4.379139	1.473759	-1.018199
H	5.193254	0.883772	-1.438575
H	4.090631	2.217417	-1.76943
H	4.767676	2.022294	-0.15404
C	-4.229875	1.616319	-1.138227
H	-5.126714	1.06614	-1.42552
H	-4.50048	2.295351	-0.322499
H	-3.934057	2.241603	-1.987318
C	-4.353208	-1.50815	-0.921155
H	-5.210817	-0.931903	-1.270325
H	-4.120594	-2.259039	-1.683478
H	-4.659673	-2.052738	-0.021548
H	1.511544	2.299453	-1.039175

Atom	X	<sup>7</sup> c Y	Z
Mo	0.00169	-0.313309	0.500653
S	1.541181	1.548198	0.076144
S	1.887584	-1.496856	-0.515696
S	-1.8619	-1.495011	-0.552597
S	-1.588027	1.532264	0.17131
C	3.108396	0.928995	-0.48171
C	3.257472	-0.380627	-0.745944
C	-3.2461	-0.394085	-0.767454
C	-3.126329	0.907746	-0.452432
S	0.020703	-0.610342	2.635632
C	-4.18929	1.967496	-0.60708
H	-5.117667	1.558015	-1.005267
H	-4.414128	2.438525	0.354863
H	-3.853362	2.760076	-1.283086
C	-4.468956	-1.077254	-1.32748
H	-5.293798	-0.379551	-1.474144
H	-4.249295	-1.544224	-2.292947
H	-4.816116	-1.870625	-0.657837
C	4.501329	-1.059833	-1.262407
H	5.314792	-0.352013	-1.423568
H	4.853493	-1.821262	-0.559163
H	4.304334	-1.566189	-2.212824
C	4.153821	2.003204	-0.653119
H	5.096226	1.598906	-1.022706
H	3.815043	2.767579	-1.359574
H	4.353657	2.508829	0.296797
H	0.001115	-1.96501	0.361089